Spring 1-1-2016

First-Principles Study of Phonon Transport in Two-Dimensional Materials and Phonon Transmission Across Magnesium Silicide/Magnesium Stannide Interfaces

Xiaokun Gu
University of Colorado at Boulder, guxiaokun@gmail.com

FIRST-PRINCIPLES STUDY OF PHONON TRANSPORT IN TWO-DIMENSIONAL MATERIALS AND PHONON TRANSMISSION ACROSS MAGNESIUM SILICIDE/MAGNESIUM STANNIDE INTERFACES

by

XIAOKUN GU

B.E., Tsinghua University, 2008

M.E., Tsinghua University, 2011

A thesis submitted to the

Faculty of the Graduate School of the

University of Colorado in partial fulfillment

of the requirement for the degree of

Doctor of Philosophy

Department of Mechanical Engineering

September, 2016

This thesis entitled:
First-principles study of phonon transport in two-dimensional materials and phonon transmission across magnesium silicide/magnesium stannide interfaces
written by Xiaokun Gu
has been approved for the Department of Mechanical Engineering

Professor Ronggui Yang, Chair

Professor Baowen Li

Date

The final copy of this thesis has been examined by the signatories, and we find that both the content and the form meet acceptable presentation standards of scholarly work in the above mentioned discipline.

ABSTRACT

Gu, Xiaokun (Ph.D., Mechanical Engineering)

First-Principles Study of Phonon Transport in Two-Dimensional Materials and Phonon Transmission across Magnesium Silicide/Magnesium Stannide Interfaces

Thesis directed by Professor Ronggui Yang

Low-dimensional and nanostructured materials have been shown to be of exceptional electronic, optical and mechanical properties, with great potential for novel applications. Understanding the thermal transport properties of low-dimensional materials is essential for designing reliable devices with these novel materials. The objectives of this thesis are to develop numerical methods based on the first-principles calculations to predict the thermal transport properties of novel two-dimensional and nanostructured materials, to explore their unique phonon dynamics and to exploit them for thermal applications.

In the first part of this thesis, the first-principles based Boltzmann transport equation approach is developed. We apply this approach to predict a series of novel two-dimensional materials, including silicene and single-layer transition metal dichalcogenides (TMDs). Their thermal conductivities are found to be highly correlated to their crystal structures and atomic masses. Using the same approach, we also study the layer thickness-dependence of thermal conductivity of MoS_2. Unlike conventional thin film materials, whose thermal conductivity is usually suppressed when the thickness decreases due to phonon-boundary scattering, the thermal conductivity of MoS_2 decreases when increasing its thickness. It appears that both the phonon dispersion and the

anharmonicity change with the thickness of MoS_2. To further reduce the thermal conductivity of single-layer MoS_2 for potential thermoelectric applications, we study the thermal conductivity of $Mo_{1-x}W_xS_2$ alloy embedded with WS_2 nanodomains. The nanostructured two-dimensional alloy has a very low thermal conductivity, only one-tenth of MoS_2, because both high-frequency and low-frequency phonons can be effectively scattered by atomic-difference and nanodomains, respectively.

In the second part of this thesis, the first-principles-based atomistic Green's function approach is developed to study phonon transport across interfaces between dissimilar materials. When two dissimilar materials with different lattice constants are connected at an interface, the lattice near the interface is usually distorted. Such a lattice distortion can extend to several unit cells away from the interface. Using direct first-principles calculations to model thermal transport near the interfacial region becomes infeasible. To overcome such numerical challenges, a methodology is developed to extract second-order harmonic interatomic force constants based on higher-order force constant model, which is originated from virtual crystal approximation but considers the local force field difference. Phonon transmission across Mg_2Si/Mg_2Sn interfaces and $Mg_2Si/Mg2Si_{1-x}Sn_x$ is studied. The interfacial thermal resistance across $Mg_2Si/Mg_2Si_{1-x}Sn_x$ interface is found to be weakly dependent on the composition of Sn when the composition of x is less than 40% but increases rapidly when it is larger than 40% due to the transition of high-frequency phonon density of states in $Mg_2Si_{1-x}Sn_x$ alloys.

ACKNOWLEDGEMENTS

Foremost, I would like to express my sincere gratitude to my advisor Prof. Ronggui Yang for the continuous support of my Ph.D. study and research, for his patience, motivation, enthusiasm. His knowledge and vision in heat transfer and nano science help me to overcome many difficulties in research. I also learnt a lot of things from him, especially on how to probe and think about scientific problems, which will be my precious wealth in my future career.

Besides my advisor, I would like to thank the rest of my thesis committee: Prof. Yung-Cheng Lee, Prof. Baowen Li, Prof. Charles Musgrave and Prof. Xiaobo Yin, for their encouragement, insightful comments and advice, and being supportive over the past few years.

I would thank my labmates in our group for their encouragement and support: Dr. Xiaobo Li, Dr. Wei Wang, Dr. Jun Zhou, Dr. Yuanyuan Wang, Dr. Qian Li, Dr. Gensheng Wu, Dr. Jiafeng Wu, Xin Qian, Shanshan Xu, Dr. Dongliang Zhao, Dr. Rongfu Wen and Tianzhu Fan.

Last but not least, I would like to thank my wife Miao and my parents for supporting me to finish my Ph. D. studies.

Table of contents

Contents

CHAPTER I INTRODUCTION 1
I.1 Thermal Transport in Nanoscale Structures 1
I.2 Numerical methods for phonon transport 2
I.3 Two-dimensional materials 5
I.4 Thermoelectric materials 9
I.5 Objectives of the thesis 10
I.6 Organization of the thesis 11
CHAPTER II FIRST-PRINCIPLES PREDICTION OF PHONONIC THERMAL CONDUCTIVITY OF SILICENE: A COMPARISON WITH GRAPHENE 13
II.1 Introduction 13
II.2 Theoretical methods 16
II.2.1 First-principles calculations for phonon dispersion and phonon scattering rate 17
II.2.2 Numerical solution of phonon Boltzmann transport equation 20
II.3 Phonon dispersion 24
II.4 Intrinsic thermal conductivity of graphene and silicene 26
II.5 The role of the ZA branch 32
II.6 Length dependence of the thermal conductivity 35
II.7 Summary of this chapter 42
CHAPTER III PHONON TRANSPORT IN SINGLE-LAYER AND FEW-LAYER TRANSITION-METAL DICHALCOGENIDES 44
III.1 Introduction 44
III.2 Numerical methods 49
III.3 Thermal conductivity of single-layer TMDs 52
III.4 Thermal conductivity of bulk MoS_2 60
III.5 Layer-dependent thermal conductivity of MoS_2 64
III.6 Summary of this chapter 70
CHAPTER IV PHONON TRANSPORT IN TWO-DIMENSIONAL MOLYBDENUM TUNGSTEN ALLOY EMBEDDED WITH NANODOMAINS 72

IV.1 Introduction 72
IV.2 Numerical methods 74
IV.2.1 Pierels-Boltzmann transport equation for lattice thermal conductivity 74
IV.2.2 Green's function approach for phonon-alloy and phonon-nanodomain scattering rates 76
IV.3 Thermal conductivity of $Mo_{1-x}W_xS_2$ alloy 80
IV.4 Phonon-nanodomain scattering rates 82
IV.5 Thermal conductivity dependence of alloy composition 85
IV.6 Summary of this chapter 87
CHAPTER V PHONON TRANSMISSION ACROSS MATERIAL INTERFACES: A FRIST-PRINCIPLES-BASED ATOMISTIC GREEN'S FUNCTION STUDY 90
V.1 Introduction 90
V.2 Modeling approaches 92
V.2.1 Interatomic force constants from the first-principles calculations 94
V.2.2 AGF approach for phonon transmission 100
V.2.3 Implementation for $Mg_2Si/Mg_2Si_xSn_{1-x}$ interface 102
V.3 Phonon dispersion of Mg_2Si, Mg_2Sn and their superlattice 105
V.4 Phonon transmission across a sharp Mg_2Si/Mg_2Sn interface 110
V.5 Phonon transmission across $Mg_2Si/Mg_2Si_{1-x}Sn_x/Mg_2Si$ 114
V.6 Summary of this chapter 121
CHAPTER VI CONCLUSIONS AND FUTURE WORK 122
APPENDIX 124
A.1 The shape of silicene's ZA phonon dispersion 124
A.2 The long-wavelength ZA phonon modes in graphene 126
A.3 Analytical limit of the scattering rates of graphene's acoustic phonon modes 127
A.4 Analytical limit of the scattering rates of silicene's acoustic phonon modes 129
A.5: Imposing translational and rotational invariance to the fitting for interatomic force constants 130
BIBLIOGRAPHY 133

TABLES

Table III.1. Experimental studies on the thermal conductivity in MoS_2. χ is the temperature coefficient of Raman signal and α is the absorption ratio used for data fitting……48

Table III.2. Lattice constants and spring constants of single-layer TMDs from DFT calculations, and the lattice constants from literature…….53

FIGURES

Figure. I.1: Atomistic simulation methods for the calculation of phonon properties and thermal conductivity……...……...2

Figure I.2: Top view and side view of some typical 2D materials. The primitive unit cell of each material is indicated by black lines in the top view……7

Figure I.3. The geometrical and physical factors that affect the thermal conductivity of 2D materials…….....8

Fig. II.1. (a) Top and side views of the buckled atomic structure of silicene. The parallelogram denotes the primitive unit cell of silicene. (b) First Brillouin zone of silicene (as well as graphene). The black dots are the q-grid points used to calculate the thermal conductivity. (c) The schematics of the simulation domain for a finite size *L* sample……...……..17

Figure II.2. Phonon dispersion of graphene (a) and silicene (b) calculated from the first-principles. The red line in (a) is the renormalized dispersion curve for ZA modes which satisfies $\omega \propto q^{3/2}$ near the zone center. This renormalized dispersion relation is used to calculate and analyze the phonon scattering process and thermal conductivity of graphene in this work…….……..26

Figure II.3. The dependence of the thermal conductivity on q-grid for graphene (a) and silicene (b) with sample size $L = 3\mu\text{m}$ ……..28

Figure II.4. Thermal conductivity of graphene as a function of temperature. The solid, dashed, dashed-dotted black lines are the calculated thermal conductivity of graphene with sample sizes L=100 μm, 10 μm and 3 μm, respectively. The pink line is the PBTE solution from Singh et al's work for an infinite size sample. Experimental values are represented by open symbols: circles

represent measured values for isotopically enriched graphene with 99.99% ^{12}C and 0.01% ^{13}C, while triangles, diamonds and pentagons are the values for naturally occurring graphene…….30

Figure II.5. Calculated thermal conductivity of silicene as a function of temperature……..31

Figure II.6. Scaled thermal conductivities from different phonon branches of (a) graphene and (b) silicene with sample size $L = 10\mu\text{m}$ as a function of temperature.…….32

Figure II.7. Scattering rates of acoustic phonon modes of graphene (a) and silicene (b) along Γ-M direction at 300 K……...33

Figure II.8. Scattering rates of out-of-plane acoustic phonon modes of graphene (a) and silicene (b) along Γ-M direction at 300 K……35

Figure II.9. Length dependence of thermal conductivity of each phonon branch of (a) graphene and (b) silicene. The inset in (b) is the q-dependence of thermal conductivity of silicene when the boundary scattering is not considered…….36

Figure II.10. Accumulated thermal conductivity of the LA and TA branches of silicene as a function of phonon frequency. The values are calculated using a 128×128 q-grid…….37

Figure II.11. Scattering rates of in-plane LA and TA acoustic phonon modes in graphene (a) and silicene (b) along the Γ-M direction at 300 K using log-log scale……..39

Figure III.1. Crystal structures of (a) MoS_2 and (b) ZrS_2 monolayers as examples for 2H and 1T single-layer TMDs, with the Mo atom in purple, the Zr atom in green, and the S atom in yellow...45

Figure III.2. Phonon dispersion of bulk MoS_2. Black lines are the results calculated using the second-order harmonic force constants from first-principles calculations. Dots are the experimental data from inelastic neutron scattering measurement……50

Figure III.3. Mode-specific Gruneisen parameters of acoustic and low-lying optical phonons of bulk MoS_2. Dots and lines represent the Grunesien parameters calculated from the finite-difference method and the perturbation theory, respectively……...52

Figure III.4. The calculated thermal conductivity of MoS_2 at 300K as a function of sample size…55

Figure III.5. The thermal conductivity of (a) 2H and (b) 1T TMD monolayers as a function of temperature……56

Figure III.6. Phonon dispersion of (a) MoS_2 and WS_2, and (b) ZrS_2 and HfS_2 calculated from the first-principles simulations…….....57

Figure III.7. Phonon lifetime of MoS_2 and WS_2 at 300K as a function of phonon frequency…..58

Figure III.8. Calculated thermal conductivity of WS_2-like material at 300K as a function of the frequency gap between acoustic and optical branches. The black dashed lines indicate the frequency gap of MoS_2 and WS_2……59

Figure III.9. Phonon lifetime for (a) 2H TMDs and (b) 1T TMDs……60

Figure III.10. Basal-plane thermal conductivity of bulk MoS_2 as a function of temperature. Blue dot is the experimental data from pump-probe measurement…….61

Figure III.11. Cross-plane thermal conductivity of bulk MoS_2 as a function of temperature. Blue and Green dots are the experimental data from pump-probe measurement……62

Figure III.12. Room-temperature basal-plane thermal conductivity of MoS_2 as a function of layer numbers……..65

Figure III.13. Phonon dispersion of few-layer MoS_2. Black lines are the dispersion for single-layer MoS_2. Blue, red and green lines refer to the ZA_i, TA_i and LA_i branches, respectively. Dash, dash-dot and short-dash lines refer to i=1, 2, 3, respectively……..68

Figure III.14. Scattering rates of the acoustic and low-lying optical branches of phonons in single-layer and bi-layer MoS_2. Black lines are the scattering rates for single-layer MoS_2. Blue, red and green lines refer to the ZA_i, TA_i and LA_i branches, respectively. Dash and dash-dot lines refer to i =1, 2, respectively……..69

Figure IV.1. The schematic of the simulation domain. The inset shows a typical atomic configuration for the $Mo_{1-x}W_xS_2$ alloy embedded triangular WS_2 nanodomains…….……74

Figure IV.2. (a) Thermal conductivity of $Mo_{1-x}W_xS_2$ at 300K as a function of alloy composition x. (b) Thermal conductivity of $Mo_{1-x}W_xS_2$ alloy embedded with W nanodomains as a function of the size of nanodomains…….……...……...80

Figure IV.3. The accumulative thermal conductivity of $Mo_{0.5}W_{0.5}S_2$ with and without nanodomains embedded as a function phonon frequency. The thermal conductivity difference is mainly caused by low-frequency phonons.……...…….82

Figure IV.4. (a) The phonon-nanodomain scattering rates of LA phonons from the Γ point to the M point as a function of phonon frequency. (b) The phonon-nanodomain scattering rates of long-wavelength LA phonon at 0.03(0, $\pi/a_0\sqrt{3}$) and short-wavelength LA phonon at 0.97(0, $\pi/a_0\sqrt{3}$). The scattering rates are normalized by the area fraction of the nanodomains.……...84

Figure IV.5. Thermal conductivity of $Mo_{1-x}W_xS_2$ alloy embedded with 10-unit-cell-large WS_2 nanodomains at 10% area fraction at 300 K as a function alloy composition *x*.…….86

Figure IV.6. (a) Phonon-alloy scattering rates as a function of phonon frequency. (b) Phonon-nanodomain scattering rates as a function of phonon frequency.……87

Figure V.1. Numerical simulation procedure of the integrated DFT-AGF approaches: MA-AGF and HOFCM-AGF. In both approaches, an interfacial system is first converted to an effective virtual crystal. In MA, the harmonic force constants are computed from DFT calculations of the

virtual crystal, and then directly used as the inputs for AGF calculations. In HOFCM, the interatomic force constants with respect to both the atom displacements and atom species are extracted from DFT calculations. Then a force-field using these interatomic force constants are constructed, which is used to determine the equilibrium configuration of the interfacial system and the corresponding harmonic force constants that are used in AGF calculations……93

Figure V.2. (a) Calculated phonon dispersions of Mg_2Si and Mg_2Sn using the force constants from the first-principles calculations: the direct method, the MA, and the HOFCM, in comparison with the measured phonon dispersions from inelastic neutron scattering experiments. (b) Calculated phonon DOS of Mg_2Si from the direct method with and without including the long-range interaction due to the Born effective charge…….107

Figure V.3. Phonon dispersions of stretched Mg_2Si and compressed Mg_2Sn computed using the force constants from the direct method, the MA, the HOFCM. Mg_2Si and Mg_2Sn are strained to the same averaged lattice constant of them to mimic the deformed lattice near the interface……109

Figure V.4. (a) Lattice structure of Mg_2Si/Mg_2Sn superlattice. The small, medium and large atoms are Mg, Si and Sn, respectively. (b) Phonon DOS of Mg_2Si/Mg_2Sn superlattice calculated using the force constants from the direct method, the MA, the HOFCM…….110

Figure V.5. (a) The atomic system used to perform energy minimization. The arrows indicate the periodic boundary condition. (b) The atomic system for the AGF calculation. The yellow, cyan and pink atoms are Si, Sn and Mg, respectively……..111

Figure V.6. (a) Frequency-dependent phonon transmission across a sharp Mg_2Si/Mg_2Sn interface. (b) Phonon DOS of Mg_2Si. (c) Phonon DOS of Mg_2Sn……112

Figure V.7. Interfacial thermal conductance across Mg_2Si/Mg_2Sn interface at different temperature. The MA overpredicts the interfacial thermal conductance……...114

Figure V.8. (a) The schematic of the simulation system of $Mg_2Si/Mg_2Si_{1-x}Sn_x/Mg_2Si$ structure. (b) Phonon transmission across the $Mg_2Si/Mg_2Si_{1-x}Sn_x/Mg_2Si$ structure as a function of phonon frequency for different Sn compositions (x). The length of the alloy layers is fixed at 10 unit cells……..116

Figure V.9. Phonon transmission across the $Mg_2Si/Mg_2Si_{1-x}Sn_x/Mg_2Si$ structure as a function of phonon frequency for alloy layers with different Sn compositions and thickness……117

Figure V.10. The total thermal resistance of $Mg_2Si/Mg_2Si_{1-x}Sn_x/Mg_2Si$ structure as a function of the thickness of alloy layers……..118

Figure V.11. (a) The extracted interfacial resistance of $Mg_2Si/Mg_2Si_{1-x}Sn_x$ interface as a function of x. (b) The extracted effective thermal conductivity of $Mg_2Si_{1-x}Sn_x$ alloy as a function of *x*, in comparison with the measured data and the PBTE calculation……119

Figure V.12. The calculated phonon DOS of $Mg_2Si_{1-x}Sn_x$ alloys……..120

Fig. A.1. The schematic of the shear deformation of silicene……..…..126

CHAPTER I INTRODUCTION

I.1 Thermal Transport in Nanoscale Structures

Thermal conductivity plays a critical role in many applications such as nanoelectronic devices and thermoelectrics. In electronics, while the performance of semiconductor devices is improved by shrinking their characteristic size, the ability of thermal conduction is significantly reduced simultaneously, which might jeopardize the performance and reliability of the devices [1, 2]. Thus, how to dissipate heat efficiently is a challenging task for semiconductor industry. For thermoelectrics, however, low thermal conductivity materials are preferred. Different strategies have been proposed to suppress the thermal transport in the potential thermoelectric materials. One of the most efficient methods is nanostructuring [3-6]. In order to design devices or materials with desirable thermal transport ability effectively, it is essential to understand how heat is transported in nanostructures. While it is well-known that both electrons and phonons contribute to heat transfer in solid, this thesis mainly focuses on phonon transport only due to its dominant role in semiconductors and thermoelectric materials.

In nanostructures, the ability of heat transport due to phonons is dependent on both the dimension of nanostructures and the phonon mean free path (MFP) [7]. When the dimension of nanostructures is much larger than the phonon MFP, the phonon transport is diffusive and dominated by phonon-phonon scattering. On the other hand, when the dimension of nanostructures is much smaller than the phonon MFP, phonons travel ballistically and the interfacial scattering is important. If the two length-scales are comparable, both phonon-interfacial scattering and phonon-phonon scattering becomes important. Recent theoretical and experimental works [8, 9] show that the phonon-mode-specific MFP can span at least three orders of magnitude. Hence, to understand

the phonon transport in nanostructures and its related heat transport, both the two key factors, phonon MFP and phonon transmission coefficient across interfaces, should be well represented in the theoretical models. This raises significant challenges in the study of nanoscale heat transport.

I.2 Numerical methods for phonon transport

Over the past several decades, various theoretical simulation tools have been developed to understand the thermal transport in micro-/nano-scale, which heavily rely on many assumptions, such as relaxation time approximation. Recently, the integration of first-principles calculations with these phonon modeling tools made it possible to predict the phonon properties and thermal conductivity of various materials. The common theoretical approaches for investigating the phonon transport can be classified into two categories, including the Boltzmann transport equation (PBTE)-based method and molecular dynamics simulations. The required inputs of these methods are summarized in Figure I.1.

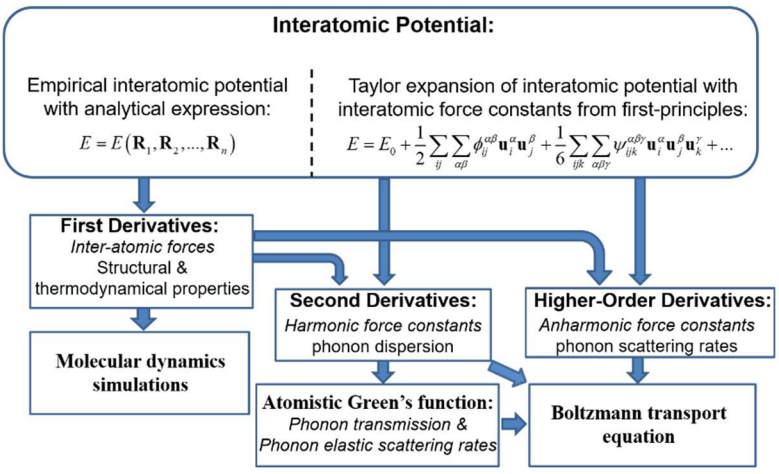

Figure. I.1: Atomistic simulation methods for the calculation of phonon properties and thermal conductivity.

The first approach to study the phonon transport is PBTE-based method. Peierls extended the Boltzmann transport equation for describing the dynamics of gases to the study of phonons in 1929 [10]. Later, the PBTE has been applied to a wide range of crystals for calculating lattice thermal conductivity [11-14]. Due to the complex of the phonon-phonon scattering, historically various approximations were proposed to estimate the scattering rate and phonon relaxation time [12-14]. Usually adjustable parameters are included in the expression, which limit the accuracy of PBTE to predict the thermal conductivity of materials. Recently, with enhanced computational power, the strength of scattering among any three phonon modes can be determined through Fermi's golden rule only if the interatomic force constants are known. Meanwhile, the power of first-principles as an accurate method of calculating the interatomic interactions is well established

For a simple periodic crystal, the PBTE can be solved in reciprocal space. The group velocity and scattering rate of each phonon mode can be well determined, which serve as the input for the PBTE, and thus the thermal conductivity of the crystal material can be calculated by solving the PBTE. The thermal properties of quite a few three-dimensional materials are computed under the framework of the first-principles-based PBTE and show remarkably high agreement with experimental measurements [8, 15-17]. Inspired by the success of this method on regular materials, thermal transport properties of novel materials could be predicted by using first-principles-based PBTE. However, since the PBTE calculations are performed in reciprocal space, the formalism is difficult to be applied to non-periodic systems, though defects scattering [18, 19], boundary scattering in simple geometry [20] can be treated as perturbation. For more complicated geometries, other approaches are needed.

For nanostructured materials, the PBTE has to be solved in real space [21-23]. By assuming material-dependent relaxation time of each phonon mode, the phonon-phonon scattering within each material can be estimated. Also if the possibility of a specific phonon transmitting across the interface is known, one can estimate the interfacial scattering. Combining these two properties, the phonon transport in nanostructured materials can be predicted through direct solving of the PBTE or other numerical approaches. The real-space PBTE formalism has been demonstrated as a powerful tool to design nanostructured materials with desirable properties. While the phonon relaxation time can be directly computed through the Fermi's golden rule, the mode-specific phonon transmission across the interface is more difficult to obtain. Several theoretical models have been proposed, including the DMM/AMM model [24], wavepacket method [25], lattice dynamics [26] and atomistic Green's function (AGF) approach [27]. Among them, the AGF approach is the most promising one, because it requires less input parameters and also provides the strong capabilities to study materials with different atomic structures. First-principles calculations have also been proposed to be integrated into the AGF approach [28]. However, due to lattice mismatch and species mixing in the interfacial region, simulations with large domains are required, which make the first-principles calculations quite challenging.

The second approach for predicting the phonon conductivity is molecular dynamics (MD) simulation based methods [29-31]. In MD simulations, phonons are not treated explicitly but the trajectories and velocities of all atoms are predicted by solving the Newton's law. The most widely used approaches to calculate the thermal conductivity are the equilibrium MD method with Green-Kubo formalism and the non-equilibrium MD method based on the Fourier's law. Due to its atomistic nature, MD approach can easily deal with complicated systems, including superlattices, nanowires, nanocomposites etc. However, there are some drawbacks in MD simulations. One of

the most important concerns is the interatomic potential which describes the interactions between atoms and is vital to phonon transport properties of the materials studied. The accuracy of the empirical potentials is quite questionable, even for simple crystals, such as silicon [32]. Therefore, it is quite challenging to predict the thermal and phonon properties of the novel materials. Even though accurate *ab initio* molecular dynamics simulations [33] have been proposed to extract thermal conductivity so that the empirical potentials are not needed any more, such approaches suffer from the strong size effects, that is, the thermal conductivity is highly dependent on the size of system, due to the long mean free path of phonons [34]. While the simulation systems with a characteristic size less than 10 nm can be handled with first-principles method, the simulation domains that span up to tens or hundreds of nanometers are required to eliminate the size effects. Therefore, how to integrate first-principles calculations efficiently and effectively is a key issue to further improve the MD methods.

Although great success has been made in the past few years to develop phonon modeling tools, there remain many challenges, in particular, to accurately and efficiently predict the thermal conductivity in different kinds of solid structures with the help of first-principles calculations. We will further develop the first-principles-based phonon modeling tools in this thesis, and mainly focus on two categories of materials, two-dimensional (2D) materials and Mg_2Si-based thermoelectric materials.

I.3 Two-dimensional materials

Since its discovery in 2004 by Novoselov *et al*. [35, 36], graphene has attracted intensive attention due to its unique physical properties and potential applications in electronics, photonics

and many other fields [37, 38]. Inspired by the success of graphene, many other two-dimensional (2D) materials [39, 40], such as hexagonal boron nitride (h-BN), silicene, transition metal dichalcogenides (TMDs), transition metal oxides, five-layered V-VI trichalcogenides and black phosphorus, have been synthesized and studied. Figure I.2 shows the lattice structures of some typical 2D materials. Many of these 2D materials have been shown to have similar or even superior properties than graphene. For example, while pristine graphene has no bandgap, some monolayer transition metal dichalcogenides, including MoS_2 and WS_2, exhibit direct bandgap, making them ideal for a wide range of applications in electronics and optoelectronics [41, 42]. Compared to conventional silicon-based electronics, these 2D material-enabled devices promise to be more efficient due to their smaller sizes. However, heat dissipation of these devices could become a bottleneck limiting their performance and reliability as thermal conductivity of many of these 2D materials could be very low. Understanding phonon transport and thermal conductivities in the 2D crystals could be very important for the design of novel devices using the 2D materials.

Significant progress has been made on understanding nanoscale heat transfer over the past two decades with the focus on nanostructures, such as such as thin films [43], nanowires [22, 44, 45], superlattices [46, 47] and nanocomposites [21, 23, 48, 49]. In these interface-dominant nanomaterials, interfaces play a crucial role on deviating thermal transport mechanisms from bulk materials, either through inducing an interfacial thermal resistance or the formation of new phonon bands [50]. The thermal conductivity of these nanostructures could be significantly lowered compared with their bulk counterparts, which can be exploited in various applications, such as thermoelectrics [51], thermal insulation [52] and thermal protection [53]. On the other hand, the surface of the ultrathin 2D materials does not necessarily hinder the thermal transport by scattering

energy carriers due to its atomic smoothness, which results in very different phonon transport and thermal conductivity in 2D materials from conventional thin films.

There have been quite some studies on thermal transport in 2D materials. As the first 2D material that gained overwhelming attention, graphene has been intensively studied in the past few years [54-57]. With a very high thermal conductivity in the range of 2000-5000 W/mK at room temperature, even higher than diamond, many works have been centered around understanding the thermal transport mechanisms and exploiting the applications of this superior heat-conducting material. Apparently those studies on phonon transport and thermal conductivity of graphene have laid a great foundation for other emerging 2D materials. However, there are still quite some issues that the consensus has not been reached by researchers, even for graphene, the most well-studied 2D material. In addition, the crystal structures of many novel 2D materials are different from the "one-atom-thick" graphene, making the direct deduction of the knowledge from graphene to other 2D materials questionable.

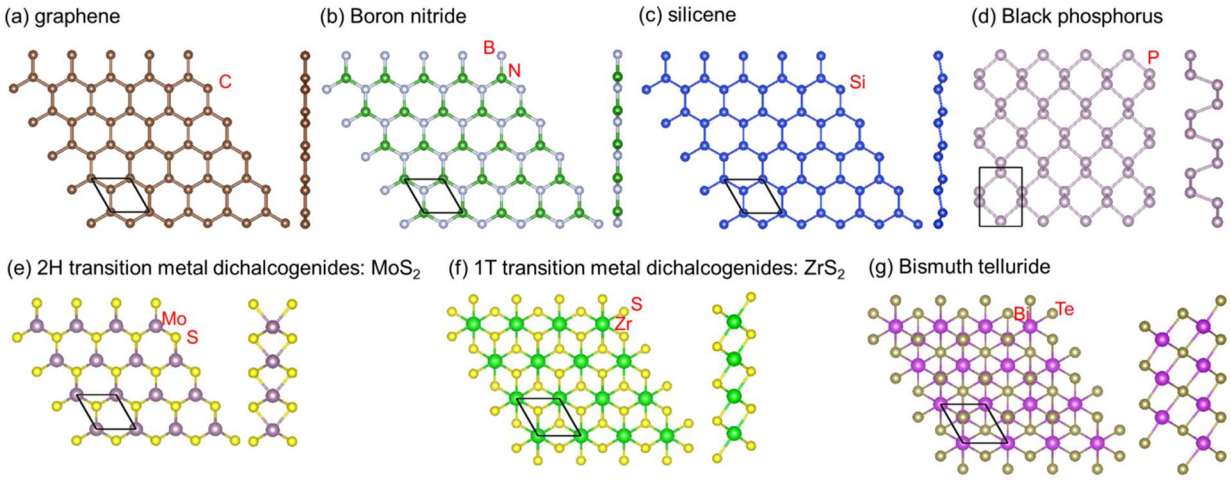

Figure. I.2: Top view and side view of some typical 2D materials. The primitive unit cell of each material is indicated by black lines in the top view.

Many geometrical constraints and physical factors can be used to change the thermal conductivity of 2D materials, which could lead to new applications in thermal management and energy conversion. For example, the thickness and the feature size in the basal plane of 2D material thin films can be tuned, which in turn can be used to control thermal transport of 2D materials. Defects and mechanical strains can also be utilized to manipulate the thermal conductivity. Furthermore, thermal transport in 2D materials is highly dependent on their interaction with the environment. For example, the coupling with substrates and other 2D crystals in heterostructures could significantly alter phonon transport in 2D materials. Surface functionalization and intercalation also significantly alter thermal transport of 2D materials. Figure I.3 summarize the geometric and physical factors that have been exploited to control the thermal conductivity of 2D materials.

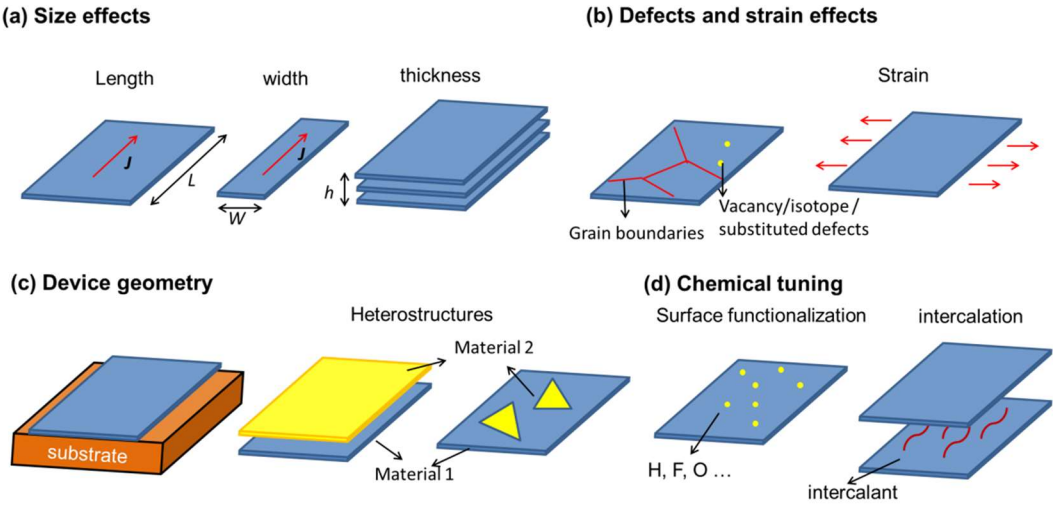

Figure I.3. The geometrical and physical factors that affect the thermal conductivity of 2D materials.

I.4 Thermoelectric materials

Thermoelectric effects include the Seebeck effect and the Peltier effect. The Seebeck effect means the phenomenon that a voltage is generated when a temperature gradient is applied on a conductor or semiconductor, while the Peltier effect is that applying electrical current can create cooling or heat pumping at the junction between two dissimilar materials. Due to the strong need to replace the conventional fossil fuels with renewable energies, using thermoelectric effects to generate electricity became a hot research topic in the past two decades, and the main task is to seek the materials with exceptional thermoelectric performance.

The thermoelectric performance of a material is usually characterized by the dimensionless figure of merit ZT, which is expressed as

$$\mathrm{ZT} = \frac{S^2\sigma}{\kappa}T \tag{I.1}$$

where S is the Seebeck coefficient, σ is the electrical conductivity, T is the temperature, and κ is the thermal conductivity. Obviously, achieving larger ZT requires a material with larger power factor $S^2\sigma$ and smaller thermal conductivity.

The research on thermoelectric materials dates back to 1950s. At that time most efforts were exerted to search bulk and alloy materials with high ZT. Some good thermoelectric materials were identified, such as Bi_2Te_3 and its alloy, PbTe and its alloy [58, 59]. In the following 30 years, progress on searching materials with high ZT was relatively slow until 1990s. Recent 20 years witness the renew of the research on thermoelectrics since some new concepts were proposed, such as nanostructuring.

The popular routes to achieve high ZT at present include searching bulk thermoelectric materials [60], fabricating individual nanostructures, such as nanowires [45], and synthesizing

bulk nanostructures, such as superlattice [61] and nanocomposites [48]. For the latter two approaches, the high ZT is mainly due to the low thermal conductivity of these nanostructured materials, and the low thermal conductivity is achieved by inducing strong phonon-interface scattering [6]. Therefore, understanding the interplay between phonons and interfaces is crucial to further enhance the thermoelectric performance of these nanostructured materials.

I.5 Objectives of the thesis

The main objectives of this study are to further develop first-principles-based theoretical modeling tools to understand the physics of phonon transport in solid materials as well as to predict the phonon transport properties in many novel materials. In particular, considering the importance of phonon MFP and phonon transmission, our efforts are mainly put to accurately predict these parameters with the state-of-art first-principles calculations.

First, we demonstrate the use of PBTE-based method to predict the thermal conductivity of 2D materials and explore the phonon scattering mechanisms in these materials. Two kinds of novel 2D materials will be studied, one is silicene, and the others are single-layer transition metal dichalcogenides.

As many geometrical constraints and physical factors can change the thermal conductivity of 2D materials, which could lead to new applications in thermal management and energy conversion, it is beneficial to understand the effects of these factors on thermal conductivity of 2D materials. We will focus on the effects of layer thickness and defects/nanodomains on the thermal conductivity of 2D materials. The first-principles-based PBTE method will be employed to study

the thermal conductivity of few-layer MoS_2 and $Mo_{1-x}W_xS_2$ alloy embedded with nanodomains as examples.

In addition, we show the prediction of phonon transmission across the interfaces with complicated atomic structures using the AGF approach. Due to the numerical challenge for first-principles to model an interfacial region, mass approximation is always employed, where the lattice mismatch and differences of force field are ignored. However, both factors are expected to change the phonon transmission. To avoid such simplification and to capture the essentials in the interfacial region, a method beyond the mass approximation is proposed to be integrated into the AGF. The adopted higher-order force constant model overcomes the numerical challenging in first-principles calculations and retains the accuracy. This integrated simulation method will then be applied to study the Mg_2Si/Mg_2Sn interfacial system with large lattice mismatch.

I.6 Organization of the thesis

In chapter I, the motivation and the objectives of this thesis for the phonon transport in two-dimensional materials and nanostructures are discussed. In chapter II, we apply the PBTE formalism to predict the thermal conductivity of silicene. By comparing the phonon transport in graphene and silicene, we reveal the unique features of phonon transport in "non-one-atom-thick" 2D materials. In Chapter III, we investigate another group of 2D materials, transition metal dichalcogenides (TMDs). The roles of atomic mass, bonding strength of single-layer TMDs, and the thickness of TMDs on the phonon transport are explored. In Chapter IV, we integrate the AGF approach with the BTE formalism and use this method to study the thermal conductivity of single-layer molybdenum tungsten alloy embedded with nanodomains. Such alloy-based 2D materials

are of low thermal conductivity, and may find its application in thermoelectrics. In Chapter V, we extend the AGF approach by integrating the interatomic force constants from first-principles into the AGF formalism. With the developed DFT-AGF method, we study the effects of local strain field on the phonon transmission across Mg_2Si/Mg_2Sn interfaces and investigate how phonon transport across the pure material/alloy interface, which could potentially guide the design of nanostructures with superb thermoelectric performance. In Chapter VI, a summary of the thesis is presented and future work is proposed based on the discussions in the thesis.

CHAPTER II FIRST-PRINCIPLES PREDICTION OF PHONONIC THERMAL CONDUCTIVITY OF SILICENE: A COMPARISON WITH GRAPHENE

II.1 Introduction

Since its discovery, graphene has attracted great attention due to its superb material properties for both fundamental science and various technological applications [37, 62, 63]. Both theoretical and experimental work reported a very high thermal conductivity for graphene, in the range of 2000 to 5000 W/mK at room temperature [54, 56, 57]. There have been thus a significant number of studies on the mechanism of phonon transport in graphene, although consensus has not yet been reached [13, 64-68]. and on the potential applications of graphene as an enabling thermal management material beyond its electronic and optoelectronic applications [69-73].

Stimulated by the advances in graphene, more recently there has been great interest in many other two-dimensional materials [39, 74], such as silicene and MoS_2 [75-78], which are expected to possess some of graphene's excellent properties along with other unique properties that graphene does not have. One of the most promising materials is silicene, which is a two-dimensional graphene-like honeycomb crystal made of silicon element that is expected to be more easily integrated with silicon-based semiconductor devices. Due to the similarity of the lattice structures of graphene and silicene, silicene shares many similar electronic properties with graphene. For example, the charge carrier of silicene is massless fermion just like as in graphene [77, 79]. However, compared with the planar structure of graphene, the honeycomb lattice of silicene is slightly buckled, which leads to some new characteristics. For instance, the buckled

structure breaks the symmetry of the crystal, making it possible to open a bandgap by applying an electric field [80, 81], which is a nontrivial challenge for graphene.

Unlike electronic properties, the thermal transport properties of silicene are still not well studied, though they are crucial to the reliability and performance of potential electronic and optoelectric devices that integrate silicene as a component. Due to the similarities and differences of lattice structure between silicene and graphene, it is of great interest to explore and compare the phonon transport mechanisms in these two 2D materials, which might shed some light on the phonon transport mechanisms of other 2D material systems which might exhibit a large variation of thermal conductivity. The presence of flexural phonons, corresponding to out-of-plane atomic vibrations, is a key signature of two-dimensional materials. In graphene, such flexural phonon modes contribute more than 50% of its large thermal conductivity [66, 67]. Until now, it has been very unclear whether the flexural phonon modes in silicene are as important as they are in graphene. For example, recent classical molecular dynamics simulations gave the conflicting conclusions depending on the empirical potentials used by different authors [82, 83]. Another important and unsettled issue in two-dimensional materials is the length dependence of the thermal conductivity. Quite a few numerical calculations have been done, but the results have been contradictory. For example, most molecular dynamics calculations, which are limited by the finite size of simulation domains, have suggested that the thermal conductivity is finite when the length exceeds a critical value [65, 68], while some lattice dynamics calculations showed that it might be divergent [13]. On the experimental side, very recent measurements showed that the thermal conductivity of graphene keeps increasing even when the size of the graphene sheet is larger than 10 μm [84]. While most of these studies were focused on graphene, other two-dimensional materials, such as silicene, have not been well studied.

Most theoretical studies on phonon transport in silicene are based on classical molecular dynamics simulations, which heavily rely on the empirical interatomic potentials. The reported values of the thermal conductivity of silicene from these molecular dynamics simulations range about one order of magnitude, from 5 W/mK to 50 W/mK [82, 83, 85, 86]. Although some of the empirical potentials, such as the Tersoff potential [83] and the modified Stillinger-Weber potential [82], are able to reasonably reproduce the phonon dispersion calculated from first-principles calculations, the predicted thermal conductivities of silicene are quite inconsistent. Although there have been some efforts to correctly reproduce the buckled structure of silicene [82], the anharmonic interactions in such buckled structures are usually not taken into account when developing the empirical potentials. A more detailed investigation beyond using empirical potentials is very much desirable.

Recently, the phonon Boltzmann transport equation (PBTE) formalism with both harmonic second-order and anharmonic higher-order force constants from the first-principles calculations has been used to study the phonon transport in a wide range of semiconductors [8, 15, 19, 87] and thermoelectric materials [88-90], both in crystalline form and nanostructured materials (including superlattice [91, 92] and nanowires [65, 93]), and two-dimensional materials, such as graphene [66, 94]. With the accurate and reliable inputs from first-principles calculations, the calculated thermal conductivity agrees quite well with experimental measurements. Furthermore, such newly developed simulation tool can accurately predict phonon dispersion, and the phonon scattering time of each phonon mode, which is essential to understand the thermal conduction mechanisms in unknown materials.

In this chapter, we study phonon transport in silicene and compare it with phonon transport in graphene. The PBTE formalism with interatomic force constants from the first-principles

calculations is employed to predict the phononic thermal conductivity of silicene. The roles of different phonon branches are carefully examined. In addition, the length-dependent thermal conductivity and the corresponding mechanism are explored.

II.2 Theoretical methods

Both graphene and silicene have the honeycomb structure with two bases in the primitive cell. The crystal structure and the corresponding first Brillouin zone are shown in Fig. II.1 (a) and (b), where the two-dimensional material are placed in the *x*-*y* plane. Since thermal transport in graphene and silicene is isotropic due to the crystal symmetry, only the thermal conductivity in the *x* direction is considered. Figure II.1(c) shows that the two-dimensional sheet with an infinite lateral length is sandwiched between two reservoirs with a distance L apart. When the two reservoirs are kept as the same temperature T, the local heat flux, J, is zero. If a small temperature difference ΔT is applied to the two reservoirs, a steady state temperature profile will be established along the *x* direction leading to a nonzero heat flux J, which can be computed by summing up the contributions from all phonon modes through

$$J = \frac{1}{(2\pi)^3} \sum_s \int \hbar \omega_{\mathbf{q}s} v_{\mathbf{q}s}^x n_{\mathbf{q}s} d\mathbf{q}, \tag{II.1}$$

where $\mathbf{q}s$ stands for the *s*-th phonon mode at $\mathbf{q}$ in the first Brillouin zone, $\hbar$ is the Planck constant, and $\omega_{\mathbf{q}s}$, $v_{\mathbf{q}s}^x$ and $n_{\mathbf{q}s}$ are the phonon frequency, group velocity in the *x* direction and the non-equilibrium phonon distribution function of mode $\mathbf{q}s$, respectively. After J is calculated from the contributions of each phonon mode, the macroscopic thermal conductivity can then be calculated from the Fourier's law of heat conduction, $K_{xx} = J / (\Delta T / L)$.

In order to evaluate the heat flux driven by the steady-state small temperature difference, we need to calculate the phonon frequency, group velocity and phonon distribution of each phonon mode in Eq. (II.1), as presented below using first-principles-based phonon Boltzmann transport equation.

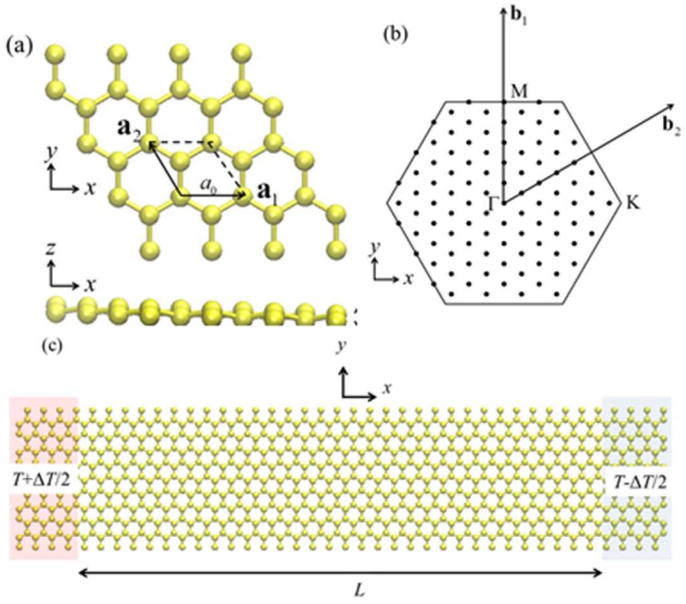

Fig. II.1. (a) Top and side views of the buckled atomic structure of silicene. The parallelogram denotes the primitive unit cell of silicene. (b) First Brillouin zone of silicene (as well as graphene). The black dots are the q-grid points used to calculate the thermal conductivity. (c) The schematics of the simulation domain for a finite size L sample.

II.2.1 First-principles calculations for phonon dispersion and phonon scattering rate

First-principles calculations are employed to calculate phonon dispersion and phonon scattering rate by calculating the harmonic second-order force constants and anharmonic third-order force constants which are the second and third derivatives of the total energy of the crystal with respect to the displacements of individual atoms in the crystal, respectively. The standard small displacement method, as described in Ref. [95] is applied. One carbon (silicon) atom noted as $\mathbf{R}\tau$, *i.e.*, the τth basis atom in the unit cell which is represented by the translation vectors $\mathbf{R}$, in a graphene (silicene) supercell is displaced with a small distance $\Delta = 0.015$ Å from its equilibrium position along the $\pm x$, $\pm y$ and $\pm z$ directions, while other atoms remain in their equilibrium positions. The force acting on each atom due to this small displacement is recorded from the output of the first-principles calculations. The harmonic force constants with respect to the displacement of atom $\mathbf{R}\tau$ in the α direction and the displacement of atom $\mathbf{R}'\tau'$ in the β direction can then be calculated as

$$\phi^{\alpha\beta}_{\mathbf{R}\tau,\mathbf{R}'\tau'} = -\frac{F^{\beta}_{\mathbf{R}'\tau'}\left(u^{\alpha}_{\mathbf{R}\tau} = \Delta\right) - F^{\beta}_{\mathbf{R}'\tau'}\left(u^{\alpha}_{\mathbf{R}\tau} = -\Delta\right)}{2\Delta} \qquad \text{(II. 2)}$$

where F is the force and u is the displacement. Taking the advantage of the periodicity and symmetry of the lattice structure, moving one atom is enough to extract all independent harmonic force constants. With the harmonic force constants calculated from the first-principle calculations, the dynamical matrix D with the pairs (τ,α) and (τ',β) as indices can then be solved for phonon dispersion,

$$D^{\alpha\beta}_{\tau\tau'}(\mathbf{q}) = \frac{1}{\sqrt{M_{\tau}M_{\tau'}}}\sum_{\mathbf{R}'}\phi^{\alpha\beta}_{\mathbf{0}\tau,\mathbf{R}'\tau'}e^{i\mathbf{q}\cdot\mathbf{R}'}, \qquad \text{(II.3)}$$

where M_{τ} is the atomic mass of the τth basis of the primitive cell. The phonon frequency $\omega_{\mathbf{q}s}$ is the square root of the s-th eigenvalue of the dynamical matrix and the group velocity $v^{x}_{\mathbf{q}s}$ is

calculated as $\partial\omega_{\mathbf{q}s}/\partial q_x$. The third-order force constants are calculated by the similar procedures but moving two atoms simultaneously. The third-order force constants with respect to the displacements of atom $\mathbf{R}\tau$, atom $\mathbf{R}'\tau'$ and atom $\mathbf{R}''\tau''$ along the α, β, and γ directions are written as

$$\begin{aligned}\psi^{\alpha\beta\gamma}_{\mathbf{R}\tau,\mathbf{R}'\tau',\mathbf{R}''\tau''} = -\frac{1}{4\Delta^2}\Big[& F^{\gamma}_{\mathbf{R}''\tau''}\left(u^{\alpha}_{\mathbf{R}\tau}=\Delta, u^{\beta}_{\mathbf{R}'\tau'}=\Delta\right) - F^{\gamma}_{\mathbf{R}''\tau''}\left(u^{\alpha}_{\mathbf{R}\tau}=\Delta, u^{\beta}_{\mathbf{R}'\tau'}=-\Delta\right) \\ & -F^{\gamma}_{\mathbf{R}''\tau''}\left(u^{\alpha}_{\mathbf{R}\tau}=-\Delta, u^{\beta}_{\mathbf{R}'\tau'}=\Delta\right) + F^{\gamma}_{\mathbf{R}''\tau''}\left(u^{\alpha}_{\mathbf{R}\tau}=-\Delta, u^{\beta}_{\mathbf{R}'\tau'}=-\Delta\right)\Big]\end{aligned}. \tag{II.4}$$

With the third-order force constants calculated from the first-principles, the three-phonon scattering rate can be calculated using the Fermi's golden rule. Once three phonons satisfy the momentum conservation condition $\mathbf{q}\pm\mathbf{q}'=\mathbf{q}''+\mathbf{G}$, with $\mathbf{G}$ representing a reciprocal vector, the transition probabilities of the three-phonon processes $\mathbf{q}s+\mathbf{q}'s'\rightarrow\mathbf{q}''s''$ and $\mathbf{q}s\rightarrow\mathbf{q}'s'+\mathbf{q}''s''$ are written as [96]

$$W^{\mathbf{q}''s''}_{\mathbf{q}s,\mathbf{q}'s'} = 2\pi n_{\mathbf{q}s}n_{\mathbf{q}'s'}\left(n_{\mathbf{q}''s''}+1\right)\left|V_3\left(-\mathbf{q}s,-\mathbf{q}'s',\mathbf{q}''s''\right)\right|^2\delta\left(\omega_{\mathbf{q}s}+\omega_{\mathbf{q}'s'}-\omega_{\mathbf{q}''s''}\right)$$

$$W^{\mathbf{q}'s',\mathbf{q}''s''}_{\mathbf{q}s} = 2\pi n_{\mathbf{q}s}\left(n_{\mathbf{q}'s'}+1\right)\left(n_{\mathbf{q}''s''}+1\right)\left|V_3\left(-\mathbf{q}s,\mathbf{q}'s',\mathbf{q}''s''\right)\right|^2\delta\left(\omega_{\mathbf{q}s}-\omega_{\mathbf{q}'s'}-\omega_{\mathbf{q}''s''}\right), \tag{II.5}$$

where the delta function denotes the energy conservation condition $\omega_{\mathbf{q}s}\pm\omega_{\mathbf{q}'s'}=\omega_{\mathbf{q}''s''}$ for the three-phonon scattering process, the + and - signs represent the annihilation and decay processes, respectively and V_3 is the three-phonon scattering matrix

$$V_3\left(\mathbf{q}s,\mathbf{q}'s',\mathbf{q}''s''\right) = \left(\frac{\hbar}{8N_0\omega_{\mathbf{q}s}\omega_{\mathbf{q}'s'}\omega_{\mathbf{q}''s''}}\right)^{1/2}\sum_{\tau}\sum_{\mathbf{R}'\tau'}\sum_{\mathbf{R}''\tau''}\sum_{\alpha\beta\gamma}\psi^{\alpha\beta\gamma}_{0\tau,\mathbf{R}'\tau',\mathbf{R}''\tau''}e^{i\mathbf{q}'\cdot\mathbf{R}'}e^{i\mathbf{q}''\cdot\mathbf{R}''}\frac{e^{\tau\alpha}_{\mathbf{q}s}e^{\tau'\beta}_{\mathbf{q}'s'}e^{\tau''\gamma}_{\mathbf{q}''s''}}{\sqrt{M_{\tau}M_{\tau'}M_{\tau''}}}. \tag{II.6}$$

where e is the eigenvector of the dynamical matrix, N_0 is the number of unit cells. We have considered both the normal (when $\mathbf{G}=\mathbf{0}$) and the Umklapp (when G represents a reciprocal vector)

three-phonon processes in current PBTE framework. All the first-principles calculations are performed with the first-principle software package Quantum-Espresso[97] using norm-conserving pseudopotentials. Plane-wave basis sets with kinetic-energy cut-offs of 80 Ry and 60 Ry are used in the graphene and silicene calculations, respectively. A 28×28×1 Monkhorst-Pack *k*-point mesh is used to relax the structure. The kinetic energy cut-off and *k*-point mesh are carefully tested so that the calculated thermal conductivity will not change even if the number of *k*-point is decreased to the half and the kinetic-energy cut-offs are reduced by 20 Ry. The cutoffs of interaction are applied to the atoms within the ninth and third nearest neighbors for harmonic and third-order force constants, respectively. The dispersion relation is found not to change by taking more neighbors into account. The translational invariance is imposed to make the set of interatomic force constants physically correct. Because we extract the interatomic force constants when atoms are in their equilibrium position, the effect of temperature on the interatomic force constants are not taken into account. For most materials, the force constants at 0K provide reasonable description of the phonon transport processes [17].

II.2.2 Numerical solution of phonon Boltzmann transport equation

The linearized PBTE is then solved to find the phonon distribution function $n_{\mathbf{q}s}$ in Eq. (II.1) considering the balance between phonon diffusion driven by the small temperature difference and phonon scatterings due to various scattering mechanisms.

In addition to the intrinsic three-phonon scattering described in Section II.2.1, the boundary scattering plays an important role at low temperature and in the low-dimensional systems. The

relaxation time of boundary scattering of phonons for finite size sample can be modeled using the partially specular and partially diffusive model, written as [98]

$$\tau_{\mathbf{q}s}^{\mathrm{B}} = \frac{1+p}{1-p}\frac{L}{2\left|v_{\mathbf{q}s}^{x}\right|}, \tag{II.7}$$

where p and $1-p$ are the fractions of phonons that are specularly and diffusively scattered at the interface, respectively. By comparing the wavelength of the dominant phonon modes from 200 K to 800 K and the roughness of the boundary, we expect that the boundary scattering is predominantly diffusive [21]. Considering that directly quantify the specularity p is still a challenge, we use the fully diffusive scattering, i.e. $p=0$, to model the boundary scattering. The thermal conductivity for a partially specular and partially diffuse boundary scattering can be extrapolated without significant difficulty. Such treatment of boundary scattering has been proved to correctly reproduce the transition between diffusive transport and the ballistic transport and has been employed in the studies on the phonon transport in many other low-dimensional materials, such as carbon nanotubes [12] and graphene [67].

Taking both the intrinsic three-phonon scatterings and the phonon-boundary scatterings into account, the linearized PBTE is now expressed as [96]

$$v_{\mathbf{q}s}^{x}\frac{\partial T}{\partial x}\frac{\partial n_{\mathbf{q}s}^{0}}{\partial T} = \sum_{\mathbf{q}'s',\mathbf{q}''s''}\left[\left(W_{\mathbf{q}''s''}^{\mathbf{q}s,\mathbf{q}'s'} - W_{\mathbf{q}s,\mathbf{q}'s'}^{\mathbf{q}''s''}\right) + \frac{1}{2}\left(W_{\mathbf{q}'s',\mathbf{q}''s''}^{\mathbf{q}s} - W_{\mathbf{q}s}^{\mathbf{q}'s',\mathbf{q}''s''}\right)\right] - \frac{n_{\mathbf{q}s}-n_{\mathbf{q}s}^{0}}{\tau_{\mathbf{q}s}^{\mathbf{B}}}. \tag{II.8}$$

To solve Eq. (8), we can write $n_{\mathbf{q}s}$ as $n_{\mathbf{q}s}^{0} + n_{\mathbf{q}s}^{0}\left(n_{\mathbf{q}s}^{0}+1\right)\varphi_{\mathbf{q}s}$ with the unknown deviation function $\varphi_{\mathbf{q}s}$ [99], which is a function of the temperature gradient. When the temperature gradient vanishes, $\varphi_{\mathbf{q}s}$ would be zero and the non-equilibrium phonon distribution function recovers to the equilibrium one. Expanding $\varphi_{\mathbf{q}s}$ into the Taylor series with respect to the temperature gradient and neglecting the higher-order terms in the limit of a small temperature gradient, $\varphi_{\mathbf{q}s}$ can further be assumed

proportional to the temperature gradient, $\varphi_{\mathbf{q}s} = \frac{\partial T}{\partial x} F_{\mathbf{q}s}$. We then can write $n_{\mathbf{q}s} = n^0_{\mathbf{q}s} + n^0_{\mathbf{q}s}\left(n^0_{\mathbf{q}s}+1\right)\frac{\partial T}{\partial x} F_{\mathbf{q}s}$. With this substitution, Eq. (8) is then recast to the form,

$$v^x_{\mathbf{q}s}\frac{\partial n^0_{\mathbf{q}s}}{\partial T} = \sum_{\mathbf{q}'s',\mathbf{q}''s''}\left[\tilde{W}^{\mathbf{q}''s''}_{\mathbf{q}s,\mathbf{q}'s'}\left(F_{\mathbf{q}''s''} - F_{\mathbf{q}'s'} - F_{\mathbf{q}s}\right) + \frac{1}{2}\tilde{W}^{\mathbf{q}'s',\mathbf{q}''s''}_{\mathbf{q}s}\left(F_{\mathbf{q}''s''} + F_{\mathbf{q}'s'} - F_{\mathbf{q}s}\right)\right] - \frac{n^0_{\mathbf{q}s}\left(n^0_{\mathbf{q}s}+1\right)F_{\mathbf{q}s}}{L/2\left|v^x_{\mathbf{q}s}\right|} \quad \text{(II.9)}$$

where $\tilde{W}^{\mathbf{q}''s''}_{\mathbf{q}s,\mathbf{q}'s'}$ and $\tilde{W}^{\mathbf{q}'s',\mathbf{q}''s''}_{\mathbf{q}s}$ are the equilibrium transition probabilities, sharing the same form as Eq. (II.5) but with the non-equilibrium phonon distribution functions ($n_{\mathbf{q}s}$, $n_{\mathbf{q}'s'}$, and $n_{\mathbf{q}''s''}$) replaced by the equilibrium functions ($n^0_{\mathbf{q}s}$, $n^0_{\mathbf{q}'s'}$, and $n^0_{\mathbf{q}''s''}$).

In order to perform the summation of the three-phonon scattering events in Eq. (9) to solve for the phonon distribution function $F_{\mathbf{q}s}$, the first Brillouin zone is discretized into a $N \times N$ Γ-point centered grid, as shown in Fig. II.1(b). The grid points are located at $\mathbf{q} = \frac{m}{N}\mathbf{b}_1 + \frac{n}{N}\mathbf{b}_2$, where $\mathbf{b}_1$ and $\mathbf{b}_2$ are reciprocal primitive lattice vectors, and *m* and *n* are integers. The delta function in Eq. (II.5) that guarantees that the energy conservation in the three-phonon processes is replaced by a Gaussian function with adaptive broadening [93, 100].

$$\delta\left(\omega_{\mathbf{q}s} \pm \omega_{\mathbf{q}'s'} - \omega_{\mathbf{q}''s''}\right) = \frac{1}{\sqrt{\pi}\sigma}\exp\left(-\left(\omega_{\mathbf{q}s} \pm \omega_{\mathbf{q}'s'} - \omega_{\mathbf{q}''s''}\right)^2 / \sigma^2\right) \quad \text{(II.10)}$$

where

$$\sigma = \left|\nabla\omega_{\mathbf{q}'s'} - \nabla\omega_{\mathbf{q}''s''}\right|\Delta q \quad \text{(II.11)}$$

and Δq is the distance between neighboring sampling points. Contrasting with the common practice of setting the broadening parameter σ to a constant value for all the three-phonon scattering events [20, 94], the adaptive scheme is able to take the non-uniformity of the energy

spacing into account. Moreover, it avoids the relatively arbitrary choice of σ in the constant broadening parameter scheme.

The set of linear equations Eq. (II.9), with respect to $F_{\mathbf{q}s}$, can then be self-consistently solved. Here we employ the biconjugate gradient stabilized method (Bi-CGSTAB), a variant of the conjugate gradient algorithm, to iteratively solve it. The details of the algorithm are provided in Ref. [101]. This algorithm successfully removes the numerical instability [20, 102, 103] that appeared in the original iterative algorithm proposed by Omini and Sparavigna [102].

After $F_{\mathbf{q}s}$ is calculated, the thermal conductivity of the two-dimensional material can be written as

$$K_{xx}\left(x\right)=\frac{2\hbar}{N_0\sqrt{3}a_0^2h}\sum_{\mathbf{q}s}\omega_{\mathbf{q}s}v_{\mathbf{q}s}^{x}n_{\mathbf{q}s}^{0}\left(n_{\mathbf{q}s}^{0}+1\right)F_{\mathbf{q}s}\,. \tag{II.12}$$

Aside from the iterative solution of Eq. (II.9), if $F_{\mathbf{q}'s'}$ and $F_{\mathbf{q}''s''}$ are set to be zero in Eq. (II.10), we can easily solve $F_{\mathbf{q}s}$ and obtain the widely used solution of PBTE under single-mode relaxation time approximation (RTA). The thermal conductivity under single-mode RTA is

$$K_{xx}=\frac{2\hbar^2}{N_0\sqrt{3}a_0^2hk_{\mathrm{B}}T^2}\sum_{\mathbf{q}s}\omega_{qs}^{2}\left(v_{\mathbf{q}s}^{x}\right)^2n_{\mathbf{q}s}^{0}\left(n_{\mathbf{q}s}^{0}+1\right)\tau_{\mathbf{q}s} \tag{II.13}$$

where $\tau_{\mathbf{q}s}=1/(1/\tau_{\mathbf{q}s}^{\mathrm{ph}}+1/\tau_{\mathbf{q}s}^{\mathrm{B}})$ is the relaxation time of mode $\mathbf{q}s$ with the relaxation time due to phonon-phonon scattering, $\tau_{\mathbf{q}s}^{\mathrm{ph}}$, which is expressed as

$$\tau_{\mathbf{q}s}^{\mathrm{ph}}=\frac{n_{\mathbf{q}s}^{0}(n_{\mathbf{q}s}^{0}+1)}{\sum_{\mathbf{q}'s',\mathbf{q}''s''}\left(\tilde{W}_{\mathbf{q}s,\mathbf{q}'s'}^{\mathbf{q}''s''}+\frac{1}{2}\tilde{W}_{\mathbf{q}s}^{\mathbf{q}'s',\mathbf{q}''s''}\right)}. \tag{II.14}$$

II.3 Phonon dispersion

Our DFT calculation yields an equilibrium lattice constant a_0 = 3.824 Å and buckling distance δ = 0.42 Å for silicene. These lattice parameters are in good agreement with previous studies [104]. For graphene, a lattice constant of a_0 = 2.437 Å is obtained after relaxation. We use the nominal layer thicknesses h = 0.335 nm and h = 0.42 nm for graphene and silicene, corresponding to the van der Waals radii of carbon and silicon atoms [83] to report our results.

Figure 2 shows the phonon dispersion of graphene and silicene in the high-symmetry directions. Due to two bases in the primitive unit cell of graphene and silicene, there are six phonon branches for each material: longitudinal acoustic (LA), transverse acoustic (TA), flexural out-of-plane acoustic branches (ZA), longitudinal optical (LO), transverse optical (TO), and flexural out-of-plane optical (ZO) branches. The frequency of the LO (or TO) mode of graphene at the Γ point is 1630 cm^{-1}, which is in good agreement with the measured G peak Raman signal [105]. The calculated phonon dispersion of silicene is identical to other calculations considering different ranges of interaction cutoff and using different source codes in literature [80, 106, 107]. In the phonon dispersion of graphene and silicene shown in Fig. II.2, we notice that the ZA branch near the Γ point shows a quadratic trend for both materials, which is a typical features of two-dimensional materials and could be explained by the macroscopic elastic theory of thin plates [62, 108]. However, while the phonon dispersion of graphene's ZA branch follows exactly the $\omega_{ZA} \propto q^2$ relation near the Γ point, a small but non-zero sound velocity for the ZA branch of silicene with a value of 1010 m/s is observed, which is an order of magnitude smaller than that of LA and TA branches. This observation is consistent with density functional perturbation theory calculation from other studies [109]. The different shape of the ZA phonon dispersion makes the

group velocity and equilibrium phonon distribution function different for graphene and silicene near the zone center: $v \propto q$ and $n^0 \propto q^{-2}$ for graphene while $v \propto q^0$ and $n^0 \propto q^{-1}$ for silicene. This difference on the shape of ZA branches near the zone center comes from the structural difference of the two materials: graphene is planar while silicene is a buckled structure. From a microscopic point of view, the $\omega_{ZA} \propto q^2$ relation near the Γ point for graphene is the direct result of two factors: 1) the rigid rotational invariance when the material rotates along any axis within the plane and 2) the decoupling of in-plane modes and out-of-plane modes due to the one-atom-thick nature of graphene. The details of the derivation can be found in the supplemental material of ref. [66]. However, silicene does not obey the rigid rotational invariance nor does it exhibit the decoupling of in-plane and out-of-plane phonon modes due to its buckled structure. In Appendix A.1, we provide a proof to show that the dispersion of the ZA branch of silicene near the Gamma point always contains a linear component, just as it does in an acoustic phonon branch in a conventional three-dimensional material.

It is worthwhile to mention that the quadratic dispersion of the ZA branch might lead to problematically strong scattering for in-plane acoustic phonons [66, 103]. Mariani and von Oppen [110] theoretically proved that the coupling of bending and stretching modes renormalizes the quadratic ZA dispersion to $\omega \propto q^{3/2}$ as $q \to 0$. In this work, the dispersion relation for ZA branch near the zone center in graphene is slightly modified to make the ZA dispersion follow the derived renormalized dispersion relation [110]. More discussions are given in Appendix A.2. In Sec.II.3.4, we show that we can get rid of the problematically strong scattering using the dispersion relation $\omega \propto q^{3/2}$ for ZA branch.

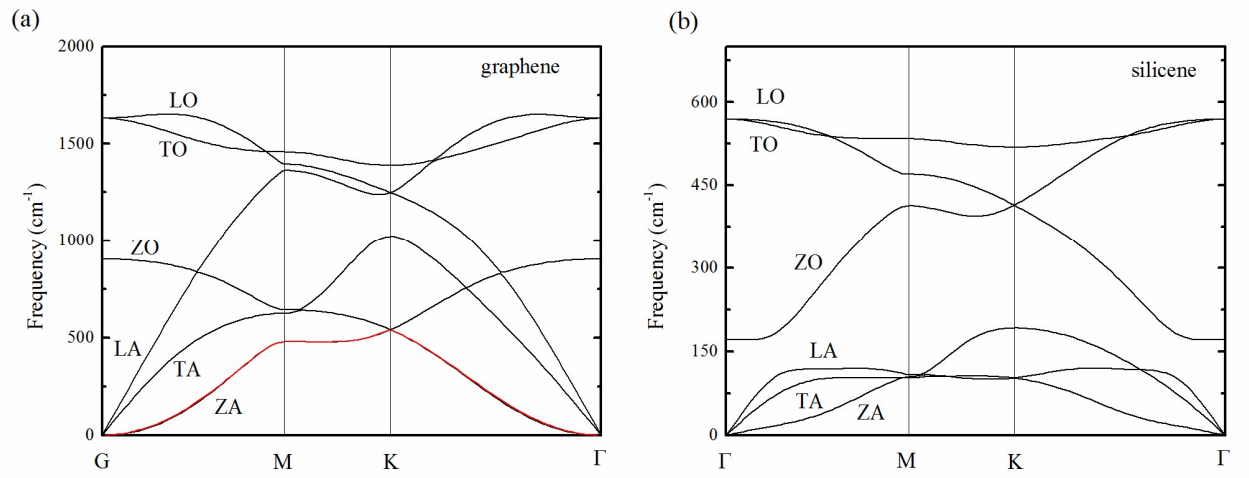

Figure II.2. Phonon dispersion of graphene (a) and silicene (b) calculated from the first-principles. The red line in (a) is the renormalized dispersion curve for ZA modes which satisfies $\omega \propto q^{3/2}$ *near the zone center. This renormalized dispersion relation is used to calculate and analyze the phonon scattering process and thermal conductivity of graphene in this work.*

II.4 Intrinsic thermal conductivity of graphene and silicene

Figure II.3 shows the dependence of calculated thermal conductivity of graphene and silicene with the sample size $L = 3\mu$m as a function of the number of q-grids used. Thermal conductivities are found to increase with the number of q-grid sampling points. Such a dependence on the q-grids can be qualitatively explained by the single-mode RTA. The thermal conductivity formula under the single-mode RTA can be expressed as

$$K \propto \sum_{s} \int \left(v_{\mathbf{q}s}^{x}\right)^{2} \omega_{\mathbf{q}s}^{2} n_{\mathbf{q}s} (n_{\mathbf{q}s} + 1) \tau_{\mathbf{q}s} d\mathbf{q} \qquad \text{(II.15)}$$

If a coarse q-grid is used, the zone center will not be well sampled. Taking advantage of the isotropicity of the frequencies near the zone center, the double integrals over **q** vector in Eq. (II.15) can be transformed to a one-dimensional integral over scale q. The difference between the thermal conductivities calculated from an idealized infinitely dense grid and that from a finite q-grid can be estimated as

$$\Delta K \propto \sum_{s} \int_{0}^{q_{\text{cut}}} v_{\mathbf{q}s}^{2} \omega_{\mathbf{q}s}^{2} n_{\mathbf{q}s} (n_{\mathbf{q}s} + 1) \tau_{\mathbf{q}s} q dq \,, \tag{II.16}$$

where q_{cut} is on the order of the difference between two neighboring q points. Eq. (II.16) also gives the estimation of the contribution from long-wavelength phonons to the total thermal conductivity. If the integrand scales with q^n with $n > 0$ as $q \to 0$, the error ΔK converges rapidly to zero as $q_{\text{cut}} \to 0$. Otherwise, the Γ point becomes a singular point, which makes ΔK highly dependent on q_{cut} and causes the q-grid dependence on the calculated thermal conductivity as shown in Fig. II.3. Since the long-wavelength acoustic phonons tend to be less scattered by other phonons, the relaxation time due to phonon scattering approaches infinity as $q \to 0$. The relaxation time of the boundary scattering $\tau_{\mathbf{q}s} = L / 2 \left| v_{\mathbf{q}s} \right|$ plays a more significant role than the intrinsic phonon-phonon scattering. As a result, ΔK scale as q_{cut}^2 for acoustic phonons with linear dispersion relation.

In order to get rid of the dependence of the thermal conductivity on the q-grid, we calculate the thermal conductivity using several q-grids with different number of sampling points up to 16384 ($N = 128$) and then extrapolate the thermal conductivity to an infinitely dense grid using the relation $\Delta K \propto q_{\text{cut}}^2$, based on the above analysis, as shown in Fig. II.3. We also note that ΔK might not be exactly proportional to q^2 since the effective phonon relaxation time also has the

contributions from the intrinsic phonon-phonon scattering. To test the robustness of the extrapolation process, we also perform linear and cubic extrapolations. The difference between different extrapolation methods is within 2% of the thermal conductivity.

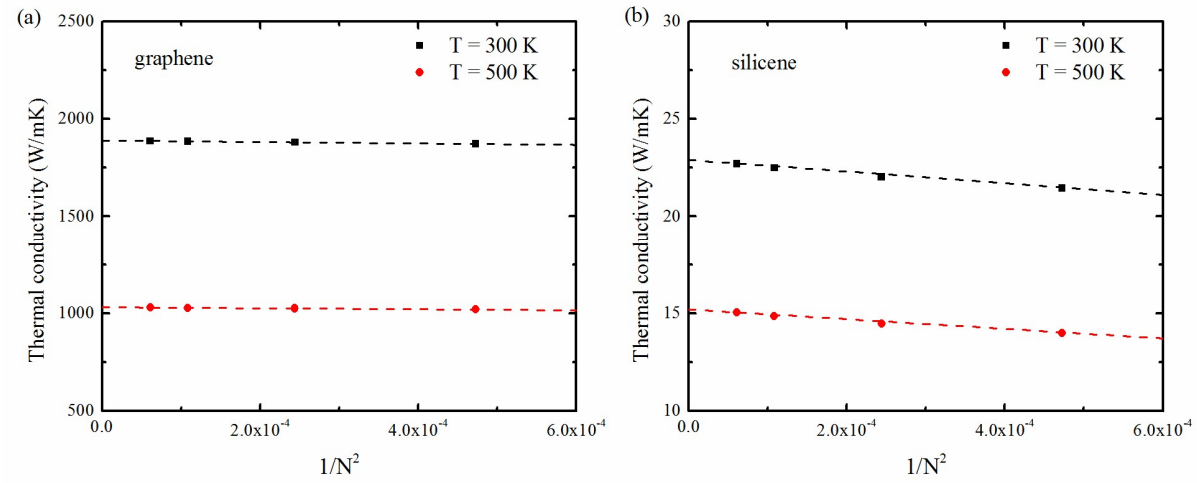

Figure II.3. The dependence of the thermal conductivity on q-grid for graphene (a) and silicene (b) with sample size $L = 3\mu\text{m}$.

To validate the approach that we employ, the calculated thermal conductivity of graphene was compared with the data available from literature, including both numerical simulations and experimental measurement. Figure II.4 shows the thermal conductivity of graphene as a function of temperature. The solid, dashed, dashed-dotted black lines are our calculated thermal conductivity for graphene with *L*=100 μm, 10 μm and 3 μm using the modified ZA dispersion as discussed in Appendix A.2. For completeness, we also show the thermal conductivity of the sample with *L*=100 μm using the ZA dispersion from DFT calculations, as indicated by the blue dotted line. It is clear that the modified ZA dispersion only slightly changes the value of the thermal conductivity of graphene. The green line is theoretical predictions from other groups' work using

similar PBTE formalism [64]. Our calculated values for a graphene sheet with L=100 μm is very close to Singh *et al*'s calculation for an infinitely large graphene sheet [64], where they employed the optimized Tersoff potential [111] to describe the interatomic interaction of graphene. The slightly larger value obtained in our prediction is probably due to the different force constants used. Figure II.4 also includes several experimental measurements using Raman spectroscopy [112-115]. Since in thermal conductivity measurement experiments graphene sheets are always suspended above holes with diameters of several microns, it is more reasonable to compare these experimental results to our calculated values with L= 3 μm to 10 μm. Although the measurement data is quite scattered due to experimental accuracy and sample processing, the values from our theoretical calculations follow a similar trend as these experimental measurements. The results shown in Fig. II.4 indicate the PBTE approach with first-principles force constants is able to give reliable predictions for the thermal conductivity of two-dimensional materials.

Figure 5 shows the temperature dependence of the thermal conductivity of silicene for different sample sizes. Dramatically different from graphene whose thermal conductivity is comparable to or even larger than its bulk forms, graphite or diamond, the thermal conductivity of silicene is an order of magnitude lower than that of bulk silicon. For example, it is around 26 W/mK for a silicene sheet with $L = 10\mu$m at 300 K while the thermal conductivity of silicon is ~140 W/mK at room temperature. Indeed the thermal conductivity of silicene with $L = 10\mu$m is comparable to the conductivity of silicon nanowires with a diameter of 55 nm [44] and thin films with a thickness of 20 nm [116]. When sample length decreases, the thermal conductivity is further reduced and shows weaker temperature dependence due to the stronger boundary scattering.

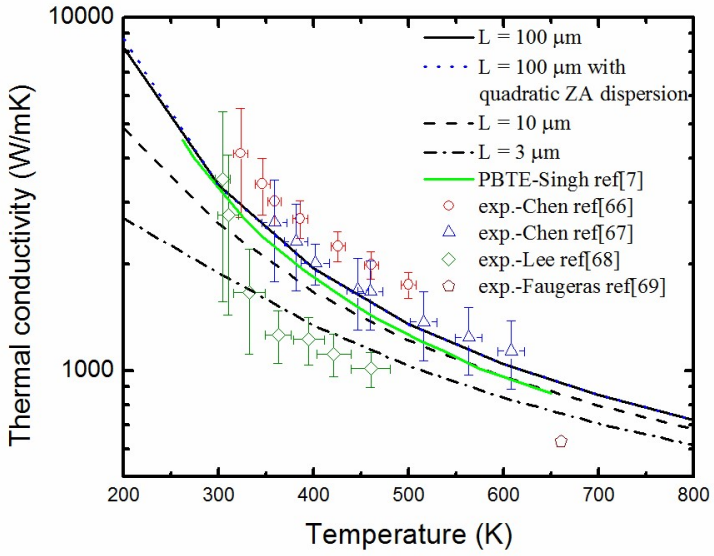

Figure II.4. Thermal conductivity of graphene as a function of temperature. The solid, dashed, dashed-dotted black lines are the calculated thermal conductivity of graphene with sample sizes L=100 μm, 10 μm and 3 μm, respectively. The pink line is the PBTE solution from Singh et al's work [64] for an infinite size sample. Experimental values [112-115] are represented by open symbols: circles [112] represent measured values for isotopically enriched graphene with 99.99% ^{12}C and 0.01% ^{13}C, while triangles [113], diamonds [114] and pentagons [115] are the values for naturally occurring graphene.

We notice that a very recent study using molecular dynamics simulations reported a much smaller thermal conductivity for silicene, ~5 W/mK, than our results. In their work, equilibrium molecular dynamics simulations is used to study the thermal conductivity of silicene with a modified Stillinger-Weber potential [82], which was originally developed for bulk silicon. Although the empirical potential they used has been optimized to better match the phonon dispersion of the silicene from DFT calculations than the original Stillinger-Weber potential [117],

the difference likely originates from two reasons: 1). the phonon dispersion relations from the empirical potential, especially the acoustic branches, are still different from those from DFT calculations; 2). anharmonic properties which are essential for predicting phonon-phonon scattering rate were not taken into account in the development of the potential. In addition to the quantitative difference on the predicted thermal conductivity, first-principle-based PBTE method provides much more detailed information of each phonon mode as discussed in this work.

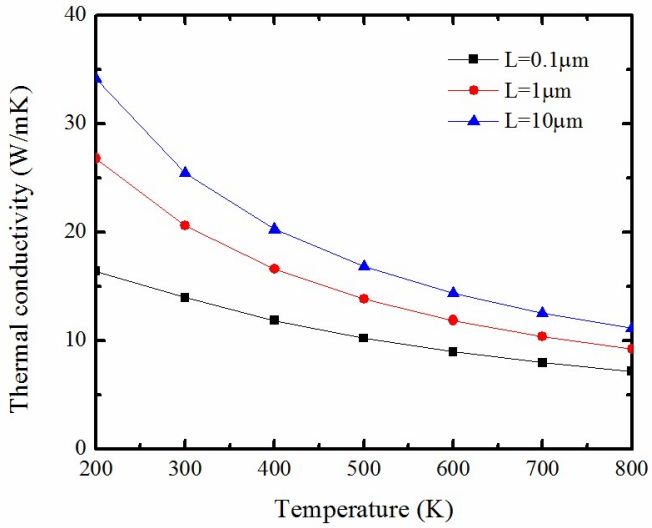

Figure II.5. Calculated thermal conductivity of silicene as a function of temperature.

To understand why silicene has a much lower thermal conductivity than silicon and graphene, we examine the contributions of the different phonon branches in graphene and silicene, as shown in Fig. II.6. When L= 10 μm, while the ZA branch contributes about 75% of the large thermal conductivity of graphene, only around 7.5% is conducted by the ZA branch in silicene. The LA and TA branches together contribute 20% and 70% to the total thermal conductivity for graphene and silicene, respectively. From this comparison, one can conclude that the overall low thermal

conductivity of silicene should be related to the strong scattering of the ZA modes. It is noted that the relative contribution of the ZA modes to the thermal conductivity of graphene is different from some other theoretical works, including the calculations using relaxation time approximation[73, 74] and MD simulations.[75, 76] Considering that the approximate nature of the empirical expressions for phonon relaxation time or empirical potentials employed, these methods might not give accurate results, though the studies could still provide valuable insights.

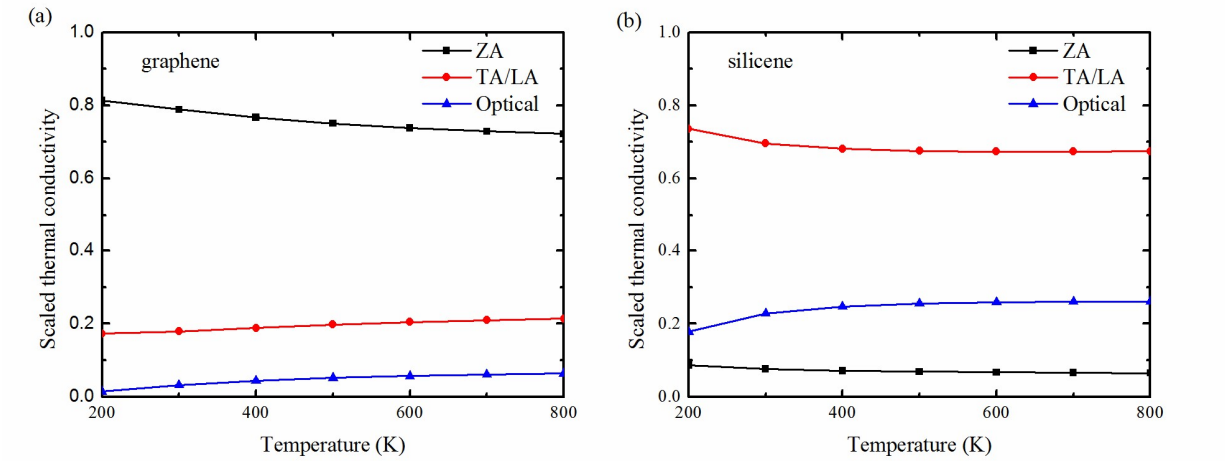

Figure II.6. Scaled thermal conductivities from different phonon branches of (a) graphene and (b) silicene with sample size $L = 10\,\mu\mathrm{m}$ *as a function of temperature.*

II.5 The role of the ZA branch

Considering that there exists the significant difference in the contribution of the ZA modes to the total thermal conductivity in graphene and silicene, it is worthwhile to perform a more detailed investigation of the scattering mechanism of the ZA modes in graphene and silicene. Figure II.7 shows the calculated scattering rates of acoustic phonons due to phonon-phonon scattering. The

scattering rate is defined as the inverse of the relaxation time, $\Gamma_{\mathbf{q}s} \propto q$ characterizing the strength of the scattering mechanism. The larger the scattering rate is, the more likely a phonon is to be scattered, i.e., with shorter lifetime. Figure II.7 shows clearly that the scattering rates of ZA modes in graphene modes are much smaller than the in-plane acoustic phonon modes. However, the scattering rates for the ZA modes in silicene are comparable to that of the other acoustic phonon modes.

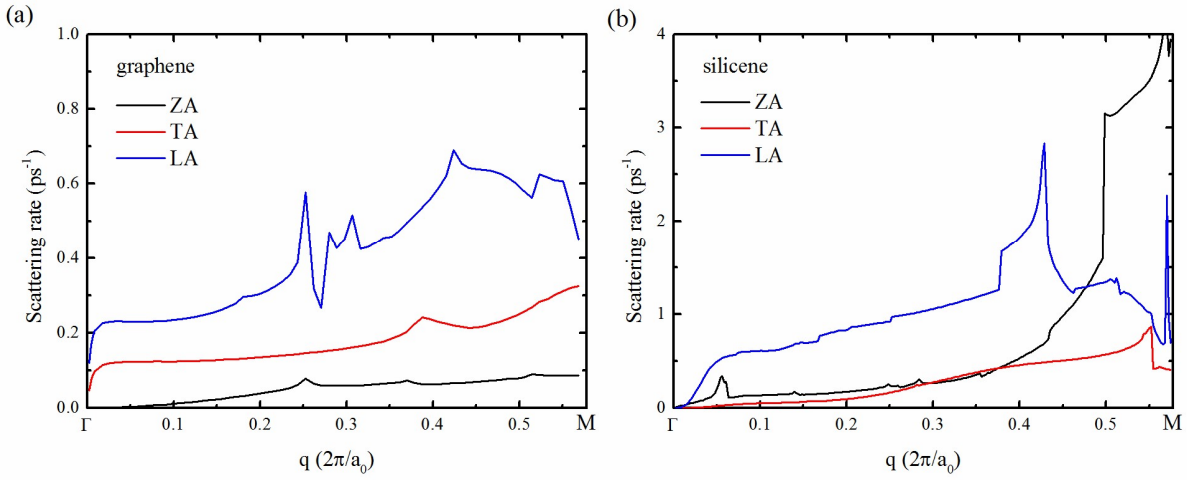

Figure II.7. Scattering rates of acoustic phonon modes of graphene (a) and silicene (b) along Γ-M direction at 300 K.

To understand the difference in the scattering rates of ZA modes in silicene and graphene, we decompose the total scattering rates of the ZA modes into different scattering channels, as shown in Fig. II.8. Figure II.8(a) shows that the ZA phonons in graphene are dominantly scattered through the absorption processes in which two ZA phonons combine to produce one in-plane acoustic phonon (LA or TA). However, Figure II.8(b) shows that absorption processes dominate the scattering channel of ZA modes where a ZA phonon is produced involving two in-plane LA or TA

acoustic phonons. The absorption processes also contribute to ~10% of the total scattering close to the zone center. These scattering channels are not observed in graphene. This is because of a symmetry selection rule [67] in graphene: for one-atom-thick materials, reflection symmetry makes the third-order force constants involving an odd number of z components vanish. As a result, scattering with odd number of out-of-plane modes, such as ZA+TA->LA and ZA+ZA->ZA, could never happen. However, due to the buckled structure in silicene, the symmetry selection rule does not apply. Therefore, the out-of-plane ZA phonon modes in silicene have more scattering channels than that in graphene as long as there is another out-of-plane or in-plane phonon available. To further explore the importance of the scattering channels involving an odd number of out-of-plane phonons on the total scattering rate of the ZA modes, Fig. II.8(b) also shows the scattering rate when these scattering channels are tuned off. The scattering rates of the ZA phonons, especially the long-wavelength phonons are greatly suppressed and reach a value comparable to the scattering rates in graphene. This investigation testifies that the scattering rate of the ZA modes in silicene is greatly increased, compared with graphene, due to the buckled structure where the symmetry selection rule that applies in graphene is broken.

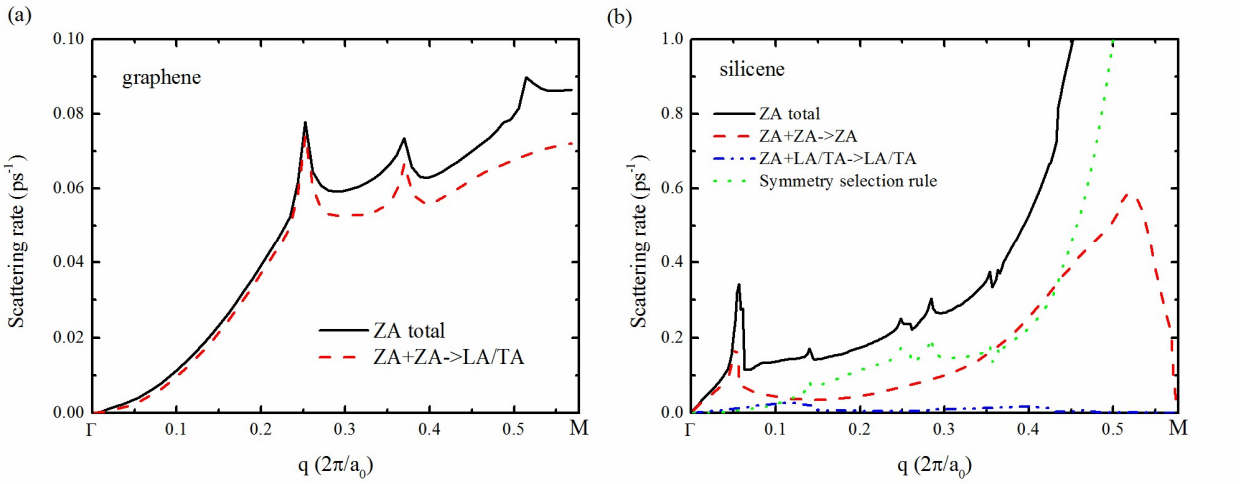

Figure II.8. Scattering rates of out-of-plane acoustic phonon modes of graphene (a) and silicene (b) along Γ-M direction at 300 K.

II.6 Length dependence of the thermal conductivity

One might conceive that the thermal conductivity of silicene would saturate quickly as the length increases because the thermal conductivity of silicene is low and the phonon mean free path in silicene might be short. However, we observe a length-dependent thermal conductivity even when the length of the silicene sample is larger than 30 μm, as discussed below.

Figure II.9 shows the thermal conductivity of graphene and silicene at 300 K as a function of sample size *L*. While the thermal conductivity of graphene appears to converge when the sample size is larger than 100μm, the thermal conductivity of silicene increases logarithmically with the sample size in the range studied in this work. The thermal conductivity of silicene increases from 18 W/mK to 28 W/mK when the size is increased from 0.3 μm to 30 μm. The unbounded thermal conductivity occurs in the whole temperature range studied in this work. The divergent (unbounded) thermal transport phenomenon of silicene with the increase of sample size can also

be verified by examining the dependence of the thermal conductivity on the *q*-grid when the boundary scattering is absent, as shown in the inset of Fig. II.9(b). To understand such anomalous phenomenon, the contributions of thermal conductivity from different phonon branches are also shown in Fig. II.9. As the sample size increases, the contributions from the optical modes and the out-of-plane ZA acoustic phonon modes of silicene become constant when $L > 1$ μm. The continuous increase of the thermal conductivity with respect to the sample size is indeed due to the in-plane acoustic phonons. Therefore, we then examine how the thermal conductivity of in-plane acoustic phonons varies with the sample size. Figure II.10 shows the accumulated thermal conductivity of the LA and TA in-plane phonon modes of two silicene sheets with different sample size, $L = 10$ μm and $L = 30$ μm, as a function of phonon frequency. It is obvious that the difference of the thermal conductivity between the $L = 10$ μm and $L = 30$ μm samples is caused by the low-frequency/long-wavelength phonons.

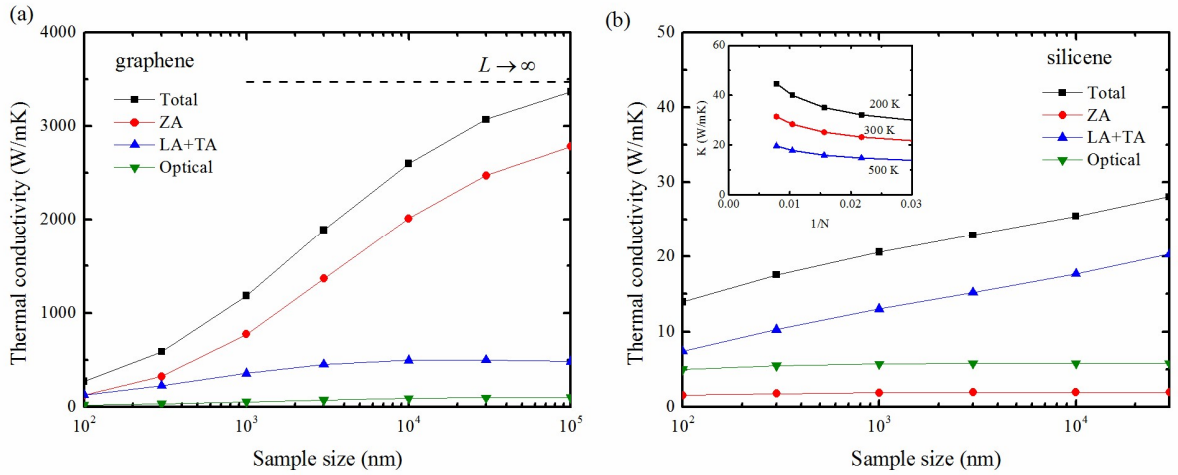

Figure II.9. Length dependence of thermal conductivity of each phonon branch of (a) graphene and (b) silicene. The inset in (b) is the q-dependence of thermal conductivity of silicene when the boundary scattering is not considered.

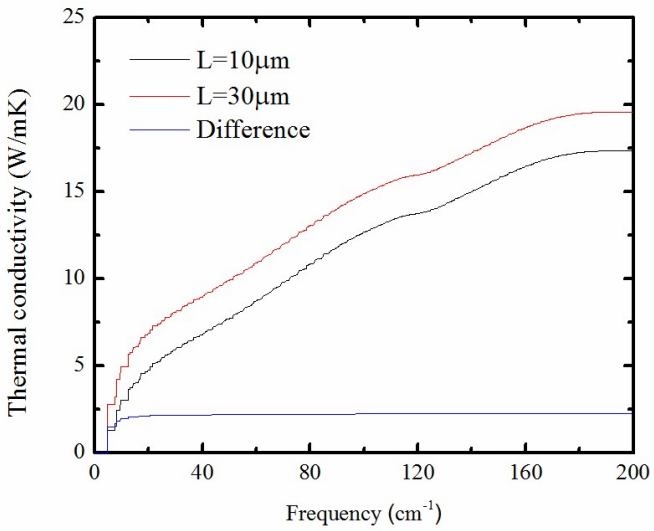

Figure II.10. Accumulated thermal conductivity of the LA and TA branches of silicene as a function of phonon frequency. The values are calculated using a 128×128 *q-grid.*

With a known linear dispersion of long-wavelength in-plane acoustic phonons as discussed in Sec. II.3.1, we are able to find out whether the thermal conductivity becomes unbounded if the relaxation time is known. According to Eq. (II.16), a finite thermal conductivity will be obtained if the relaxation time of the long-wavelength in-plane phonons which has linear dispersion follow q^n if $n > -2$. We thus perform a careful investigation on how long-wavelength in-plane acoustic phonons are scattered in graphene and silicene.

In Fig. II.11, the scattering rates of the LA and TA in-plane acoustic phonons are plotted using a log-log scale. Figure II.11(a) shows that the scattering rates of the in-plane acoustic phonons in graphene linearly decreases to zero with respect to the wavenumber q at the zone center as $q \to 0$. We noticed that the LA and TA phonon modes of graphene in the region $0<q<0.05(2\pi/a_0)$ are

scattered almost exclusively by decaying into two out-of-plane ZA modes. We can now follow an approach similar to that presented by Bonini *et al* [66], where they studied the analytic limit as $q \to 0$ by considering the decaying process of the scattering of LA and TA modes into two ZA modes on the quadratic dispersion. In a similar analysis shown in Appendix A.3, we find that the analytic limit of the scattering rate is $\Gamma_{\mathbf{qs}} \propto q$ when in-plane acoustic phonon modes are scattered to two phonons on the ZA branch with $\omega \propto q^{3/2}$ dispersion, which can explain well the numerical results observed. According to $\Gamma_{\mathbf{qs}} = 1/\tau_{\mathbf{qs}} \propto q$, the thermal conductivity of the long-wavelength LA and TA branches of graphene should be finite, since the relaxation time follows the relation that ensures the finite thermal conductivity, $\tau_{\mathbf{qs}} \propto q^n$ with $n = -1 > -2$. In addition, the modified dispersion for ZA modes makes the product $\omega_{\mathbf{qs}}\tau_{\mathbf{qs}}$ approaches constant values, instead of zero as observed when the quadratic dispersion is used [66, 103]. From our numerical calculation, the constant values are around 8 for LA modes and 14 for TA modes, both of which are much larger than unity. The larger-than-unity constant values of $\omega_{\mathbf{qs}}\tau_{\mathbf{qs}}$ ensure the condition for the existence of phonons as elementary excitations [118] is valid for long-wavlength in-plane LA and TA phonons of graphene. Therefore, by considering the renormalization of ZA phonons [110] as discussed in Appendix A.2, the problematic large scattering of the long-wavelength in-plane acoustic phonons in graphene can be avoided.

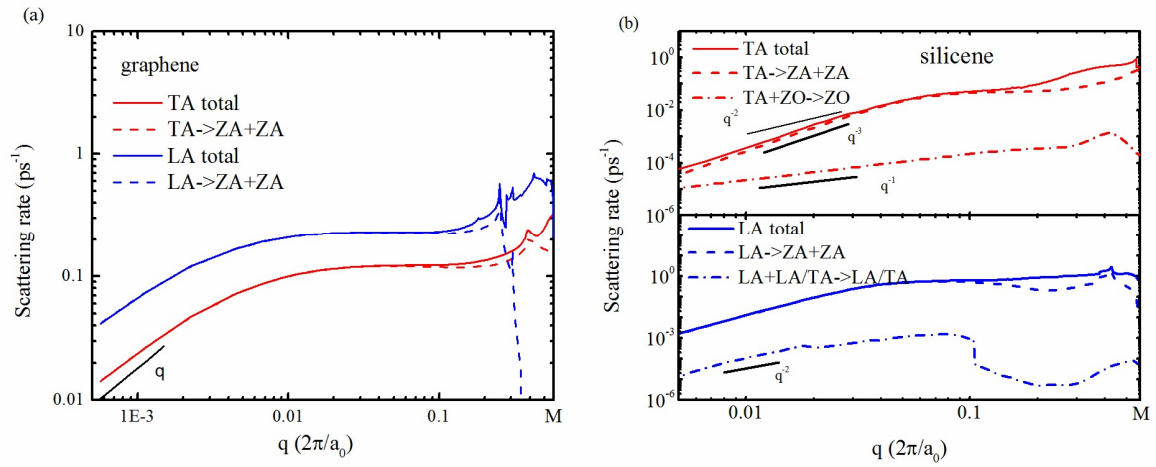

Figure II.11. Scattering rates of in-plane LA and TA acoustic phonon modes in graphene (a) and silicene (b) along the Γ-M direction at 300 K using log-log scale.

Figure II.11(b) shows that the scattering rates of silicene also approach zero when the wavenumber q goes to zero, but with a much steeper slope than that for graphene. It is found that the scattering of the in-plane LA and TA phonon modes also mainly comes from the decay processes into two ZA modes at the small wavenumber regime $0.01(2\pi/a_0)<q<0.1(2\pi/a_0)$. However, the out-of-plane ZA phonon branch on a linear dispersion is not able to scatter the LA and TA phonons as efficiently as that in graphene. The scattering process for three acoustic phonons on linear dispersions are derived in detail in Appendix A.4 which shows that the inverse of the scattering rate, or the relaxation time, scales with q^n with $n=-3<-2$ as $q\rightarrow 0$.

In addition to the decay processes, a long-wavelength LA or TA mode, $\mathbf{q}s$, in silicene can also annihilate with another mode, $\mathbf{q}'s'$, and generate the third mode $\mathbf{q}''s''$ which needs to satisfy the momentum conservation $(\mathbf{q}''=\mathbf{q}+\mathbf{q}'+\mathbf{G})$. The analytical limits of the scattering rate for the annihilation processes are also derived in Appendix A.4. If modes $\mathbf{q}'s'$ and $\mathbf{q}''s''$ are on different

branches, for example, LA+LA/TA->TA/LA, the scattering rate of the in-plane acoustic phonons scales with q^2 as $q \to 0$. If modes $\mathbf{q}'s'$ and $\mathbf{q}''s''$ are on the same branch, such as TA+ZO->ZO, the scattering rate of the in-plane TA branch has the form $\Gamma_{\mathbf{q}s} = 1/\tau_{\mathbf{q}s} \propto q$ as $q \to 0$. This linear dependence of the scattering rate on the wavenumber q for the in-plane TA modes ensures that the condition $\tau_{\mathbf{q}s} \propto q^n$ with $n > -2$ is satisfied as $q \to 0$ and thus the thermal conductivity of TA branch is finite.

However, unlike in-plane TA modes, the annihilation process for a long-wavelength in-plane LA phonon with two phonon modes on the same branch are always prohibited. This is because the group velocity of the long-wavelength in-plane LA modes, v_{LA}, is the largest of all phonon modes so that the frequency of the long-wavelength in-plane LA mode $\mathbf{q}s$, which can be estimated by $v_{\mathrm{LA}}q$ due to the linear dispersion, is always larger than the frequency difference between the modes $\mathbf{q}'s'$ and $\mathbf{q}''s''$, which can be written as $\left|\mathbf{v}_{\mathbf{q}'s'} \cdot \mathbf{q}\right|$ $\left(\le v_{\mathbf{q}'s'}q < v_{\mathrm{LA}}q\right)$ as $q \to 0$. As a result, the annihilation scattering with two phonon modes on the different branches becomes the dominant scattering mechanism for long-wavelength LA phonon as $q \to 0$.

The total scattering rate of the long-wavelength LA phonons would follows q^2 as $q \to 0$. According to Eq. (II.16), the thermal conductivity of the long-wavelength LA modes is $\Delta K \propto \int_0^{q_{\mathrm{cut}}} q^{-1} dq$, leading to a divergent thermal conductivity when the boundary scattering is absent. When the boundary scattering is included, $\Delta K \propto \int_0^{q_{\mathrm{cut}}} \frac{q}{q^2 + L} dq \propto \ln L$. This analytical limit is consistent with the observation of our numerical results, as shown in Fig. II.9(b). However we wanted to that the derived scaling relation of the relaxation time or the scattering rate with respect

to the wavenumber q for long-wavelength in-plane phonon modes would hold in the region very close to the zone center. The logarithmic dependence on the sample length we observe should be the outcome of the combination of different phonon branches, not just from the long-wavelength LA phonons.

We found a recent work on the prediction of the thermal conductivity of silicene from relaxation time approximation with interatomic force constants from first-principles calculations [119]. In their work, only three-phonon processes are considered and the calculated thermal conductivity is about 9 W/mK for an infinitely large silicene sheet, much smaller than the results from our calculations. The relaxation times of long wave-length acoustic phonon modes from their work approach zero as the wavevector $q \to 0$, which is opposite to the scaling relation we derived in this work, and also contradicts the classical theory that low-frequency phonon modes are not likely to scattered. The possible reason is that a too small cutoff of the third-order anharmonic force constants is chosen in their work. If no translational invariance is imposed, the low-frequency phonons are unphysically severely scattered, and thermal conductivity tends to be underestimated [17].

Finally, we note that the observed logarithmic length dependence of the thermal conductivity in silicene might not hold when higher-order phonon scatterings are taken into account since our calculations and analysis only consider the three-phonon process. It is worthwhile to further study the dependence of thermal conductivity on sample size in two-dimensional materials at high temperature, where higher-order phonon scattering might play a role in some of the 2D materials. Currently there are no widely-accepted conclusions on the contributions of four-phonon processes to the thermal conductivity of solids. On one hand, Raman scattering experiments clearly show the importance of four-phonon processes on the frequency shift and line width of optical phonons,e.g.

Balkanski et al [120]. On the other hand, theoretical estimation of three-dimensional bulk materials by Ecsedy and Klemens [121], shows that the scattering rate of the four-phonon processes is at least two orders of magnitude smaller than the three-phonon processes even at the temperature as high as 1000 K. Whether the four-phonon processes are important in two-dimensional materials is even more unclear. It is thus very desirable to carry out first-principles calculations on the thermal conductivity arising from both cubic and higher-order anharmonicity. However, such a calculation is by no means trivial [120] due to the limitation of computational power. We have thus considered only the three-phonon processes and expect the results very likely to be valid for a wide range of temperature by looking at the contributions of optical phonons to the total thermal conductivity.

II.7 Summary of this chapter

In conclusion, we use the phonon Boltzmann transport equation with the phonon properties calculated by interatomic force constants from the first-principles to predict the thermal conductivity of silicene and graphene. With a detailed analysis on phonon scattering rate, we have shown that silicene has a much smaller thermal conductivity than graphene. Unlike graphene, where most of the heat is conducted by out-of-plane acoustic phonons, the out-of-plane acoustic phonons contribute to only ~10% of the thermal conductivity in silicene. More importantly, in-plane acoustic phonons make the thermal conductivity of silicene unbounded with the increase of the sample size. The differences in phonon transport in silicene and graphene can be attributed to the buckled atomic structure. The buckled structure in silicene breaks the symmetry selection rule that applies to graphene, making the ZA phonon modes strongly scattered so that they contribute very little to heat transport in silicene. The buckled structure also changes the phonon dispersion

curve of the ZA branch from $q^{3/2}$ in graphene to linear, so the most important scattering channel in silicene for long wavelength LA phonon modes, LA->ZA+ZA, becomes not as efficient as in graphene to render a finite value for the intrinsic thermal conductivity. In contrast, we proved analytically that the thermal conductivity increases logarithmically with respect to the sample size when both intrinsic phonon-phonon scattering and boundary scattering are considered. This study might shed some light on the fundamental phonon transport mechanisms in other 2D materials such as transition metal dichalcogenides. For example, strong length-dependence of the thermal conductivity might be expected in MoS_2 and WS_2 due to a similarly linear dispersion of ZA phonons in these non-one-atom-thick two-dimensional materials.

CHAPTER III PHONON TRANSPORT IN SINGLE-LAYER AND FEW-LAYER TRANSITION-METAL DICHALCOGENIDES

III.1 Introduction

As a family of novel two-dimensional (2D) materials beyond graphene, monolayer and few-layer transition metal dichalcogenides (TMDs) have attracted considerable interests shortly after they were isolated or synthesized due to their unique physical properties and potential applications [40-42]. Generally monolayer TMDs can have a three-layer structure that one layer of transition metal atoms is sandwiched by two layers of chalcogenide atoms. Depending on how the chalcogenide atoms are sitting on each side of the metal layer, there are two polymorphs for monolayer TMDs: 1T phase with D_{3d} point group and 2H phase with D_{3h} point group, as shown in Fig. III.1. The physical properties of molybdenum disulfide (MoS_2) with 2H structure, as a representative 2D TMD, have been widely studied. It exhibits a series of intriguing attributes that are different from its bulk form and from that of graphene, including the switchable thickness-dependent band gap [122], strong photoluminescence [123] and significant anisotropic response under tensile strain [78]. In addition to MoS_2, other TMDs with the same 2H crystal structure, such as $MoSe_2$, WS_2 and WSe_2, might be of similar or even superior properties to MoS_2. For example, these TMDs are also of the thickness-dependent band gap [124, 125]. Triangular WS_2 monolayer displays strong room-temperature photoluminescence at the edge [126]. Compared with 2H TMDs, 1T TMDs gain relatively less attention, but might also possess some interesting properties. For

example, 1T Zirconium and hafnium dichalcogenides are considered for photovoltaic application due to their suitable band gap for visible light absorption [127, 128]. In addition, both the bandgap of single-layer ZrS_2 can be effectively tuned by mechanical strain [129].

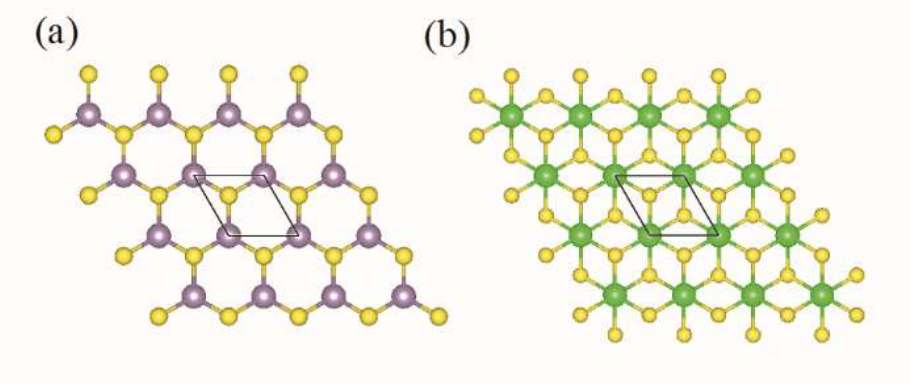

Figure III.1. Crystal structures of (a) MoS_2 and (b) ZrS_2 monolayers as examples for 2H and 1T single-layer TMDs, with the Mo atom in purple, the Zr atom in green, and the S atom in yellow.

Unlike the electronic, optical and mechanical properties of single-layer or few-layer TMDs, which have been intensively explored, the study on the thermal properties are still in its infancy, though its importance on the performance and reliability on the nano-devices are well recognized. According to the classical theory, the thermal conductivities of TMDs are thought to be low due to their heavy atom mass and low Debye temperature [130]. This has led to the consideration of single-layer or few-layer TMDs as potential thermoelectric materials [131-133]. While it is generally true that the cross-plane thermal conductivity of TMDs are low due to the weak inter-layer bonding [130], the in-plane thermal properties are unclear. There have recently been some studies on the in-plane thermal conductivity of monolayer or few-layer MoS_2 [134-142]. While some classical molecular dynamics (MD) simulations using empirical interatomic potentials reported the thermal conductivity for the single-layer MoS_2 to be less than 10W/mK [139, 140],

the measured thermal conductivity values for the single-layer and multilayer MoS_2 are usually larger than 30 W/mK [134-136]. Considering the large uncertainty in the available thermal conductivity measurement data and the inaccuracy of the empirical potentials used in molecular dynamics simulations, the first-principles-based approach with predictive power has its unique strength to explore the phonon transport in 2D TMDs.

In addition to the thermal conductivity of single-layer TMDs, the layer thickness-dependent thermal conductivity of TMDs is also of interest. In the past two decades, considerable attention has been paid to the size effects of phonon transport in semiconductor nanostructures, such as thin films [43], nanowires [22, 44, 45], superlattices [46, 47] and nanocomposites [21, 23, 48, 49]. In these semiconductor nanostructures, interfaces play a crucial role on reducing the thermal conductivity compared with their bulk counterparts by inducing additional interface scattering of phonons. However, such interface scattering might not be as important for the van der Waals solids, where two-dimensional layers are stacked together through very weak van der Waals bonding and the surface of few-layer two-dimensional materials can be atomically smooth when the thickness is reduced to only a few layers [143]. For example, both experiments [144] and numerical simulations [64, 145, 146] showed that the thermal conductivity of graphene gradually decreases when the layer number is increased and approaches to the bulk value when there are four to five layers. It is generally believed that the thermal conductivity reduction in few-layer graphene is due to the breakdown of the selection rule that arises out of the reflection symmetry of the single-layer graphene [67]. However, some other two-dimensional materials with different crystal structures, such as Bi_2Te_3 and $TaSe_2$, exhibit quite different layer-dependence of the thermal conductivity from graphene. Pettes *et al* [147]. reported the trend of decreasing thermal conductivity when the thickness of suspended Bi_2Te_3 film decreases from 25 nm to 9 nm, indicating that the interfacial

scattering in Bi_2Te_3 is still non-negligible when the thickness is larger than 9 nm. Qiu and Ruan [148] found a non-monotonic dependence of the thermal conductivity on layer thickness of Bi_2Te_3 from their equilibrium molecular dynamics simulations. The single-layer Bi_2Te_3 has the highest thermal conductivity, which is then reduced to the minimum value for the three-layer Bi_2Te_3, and then converged back to the bulk value. Yan et al. [149] measured the thermal conductivity of two-dimensional transition metal dichalcogenide $TaSe_2$ with 1T structure using the optothermal Raman measurement, and found that the thermal conductivity of these $TaSe_2$ films at room temperature decreases from its bulk value of 16 W/mK to 9 W/mK in 45-nm-thick films. These studies indicate that the crystal structures of the two-dimensional materials might play an important role in determining their layer thickness-dependent thermal conductivity. Because the crystal structure of MoS_2 is quite different from the materials studied before, it is unclear how the thermal conductivity of two-dimensional MoS_2 changes with its layer thickness.

Along this line of curiosity, many experimental works have been conducted to measure the thermal conductivity of single-layer, few-layer and bulk MoS_2. The measured results are 34.5 W/mK [135] and 84 W/mK [150] for single-layer one, 77 W/mK [150], 46 W/mK [136], 50 W/mK [136] and 52 W/mK [151] for 2-layer, 4-layer, 7-layer and 11-layer MoS_2, respectively. Liu *et al*. [152] reported a large thermal conductivity value for bulk MoS_2, around 100 W/mK. The details of these measurements are summarized in Table III.1. Direct comparison among these experimental data is challenging since both sample quality and experiment conditions are different from different research groups.

Theoretical work has also been employed to study the thermal conductivity in single-layer and few-layer MoS_2. A recent MD study using Stillinger-Weber (SW) potential showed that the thermal conductivity of MoS_2 is about 5 W/mK for all MoS_2 with different layer numbers [153].

This calculated thermal conductivity is one to two orders-of-magnitude smaller than the measured results [152], which indicates that the anharmonicity of the intralayer interaction from the empirical potential is severely overestimated. On the other hand, the first-principles-based Peierls-Boltzmann transport equation (PBTE) method [8, 16, 20, 103, 154, 155] has been applied to predict the thermal conductivity of many bulk and two-dimensional materials, including single-layer MoS_2 [138, 156], which showed satisfactory agreement with the experiment results.

Table III.1. Experimental studies on the thermal conductivity in MoS_2. χ is the temperature coefficient of Raman signal and α is the absorption ratio used for data fitting. The details of measurements are summarized in a recent review (Ref. [143]).

Ref.	Method	Sample type	Room-temperature thermal conductivity (W/mK)	Experimental conditions
Yan [135]	Raman	Exfoliated, transferred	34.5±4 (1-Layer)	A_{1g} mode, χ =0.011 cm^{-1}/K, α=9±1% ,170 nm diameter laser spot, suspended on 1.2-μm-diameter holes, ambient condition
Zhang [150]	Raman	Exfoliated, transferred	84±17 (1-Layer)	A_{1g} mode, χ =0.0203 cm^{-1}/K, α=5.2±0.1%,460-620 nm diameter laser spot, suspended on 2.5-to-5.0-μm-diameter holes, ambient condition
Zhang [150]	Raman	Exfoliated, transferred	77±25 (2-Layer)	A_{1g} mode, χ =0.0136 cm^{-1}/K, α=11.5±0.1%,460-620 nm diameter laser spot, suspended on 2.5-to-5.0-μm-diameter holes, ambient condition
Jo [136]	Micro-bridge	Exfoliated, transferred	44–50 (4-Layer)	Suspended sample; length: 3 μm, width: 5.2 μm.
Jo [136]	Micro-bridge	Exfoliated, transferred	48-52 (7-Layer)	Suspended sample; length: 8 μm, width: 2.2 μm.
Sahoo [151]	Raman	CVD, transferred	52 (11-Layer)	A_{1g} mode, χ= 1.23 × 10^{-2}cm/K, α = 10%,1-1.5 μm laser spot, suspended on a 10- μm-radius quadrant, ambient condition
Liu [152]	Pump-probe	Bulk	85-112	Modulation frequency of pump beam: 10.7 MHz

In this chapter, we first present a systematic study of the phonon transport in single-layer TMDs MX_2 (M = Mo, W, Zr and Hf, X = S and Se) by solving the PBTE with interatomic force constants inputs from first-principles calculations. The validity of applying SMRTA to predict the thermal conductivity of single-layer TMDs is assessed first by comparing the calculation results of

SMRTA and the iterative solution of the PBTE on MoS_2. The thermal conductivities of the eight single-layer TMDs are then predicted from the iterative solution of the PBTE. Much higher thermal conductivity is found in 2H TMDs, especially WS_2, comparing to that of 1T TMDs. The origins of their distinct thermal transport properties are explored by detailed phonon scattering analysis. Then, we study the dependence of thermal conductivity of two-dimensional MoS_2 on its layer thickness. Due to the computational power limitations, we calculate the thermal conductivity of one- to three-layer MoS_2, but compare them with bulk MoS_2. The thermal conductivity of single-layer MoS_2 is found to be the highest among all samples studied, and the thermal conductivity decreases with the thickness changing from one to three layers. Detailed phonon scattering rate analysis shows that the anharmonicity is significantly increased in the bi- and tri- layer MoS_2 compared with single-layer MoS_2, which suppresses the heat conduction ability of flexural acoustic phonons.

III.2 Numerical methods

In the first-principles-based approach, the accurate second-order harmonic and third-order anharmonic force constants are first extracted from density functional theory, which are employed to calculate the phonon transport properties, including phonon dispersion relation and three-phonon scattering rates. Such phonon dynamics information is then used as the inputs for the PBTE, which considers the balance between phonon diffusion driven by the small temperature difference and phonon scatterings due to various scattering mechanisms. Here, we consider three kinds of phonon scattering mechanisms, three-phonon scattering, isotope scattering and diffusive boundary scattering. The solution of PBTE provides the information of the population of each phonon mode and enables us to evaluate the thermal conductivity. The theoretical background of PBTE,

including the phonon scattering mechanisms and the solution of PBTE from the SMRTA and the iterative approach, can be found in Chapter II.

Since phonon properties and the calculated thermal conductivity are very sensitive to the interatomic force constants, we perform the following tests to validate our extracted force constants. Figure III.2 shows the calculated phonon dispersion curves of bulk MoS_2 using the extracted harmonic force constants, which are in reasonable agreement with the available experimental data of from the inelastic neutron scattering measurement [157].

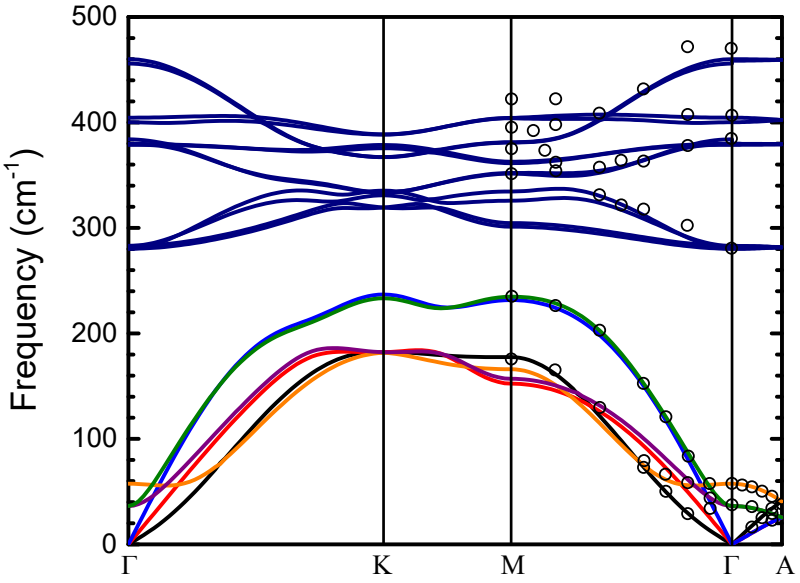

Figure III.2. Phonon dispersion of bulk MoS_2. Black lines are the results calculated using the second-order harmonic force constants from first-principles calculations. Dots are the experimental data from inelastic neutron scattering measurement [157].

We then turn to the verification of the third-order anharmonic force constants. Recent studies have shown that the cutoff of anharmonic interaction is crucial to the calculation of thermal conductivity [158]. While too small a cutoff tends to overestimate the thermal conductivity, a larger cutoff requires much more computational resources. To make our calculations affordable, we carefully chose the range of anharmonic interaction to be 6 Å. We validate the extracted third-order force constants by calculating the mode-specific Gruneisen parameters, which serve as indicators for the degree of anharmonicity of the crystal, using bulk MoS_2 as a testing case. The mode-specific Gruneisen parameters can be calculated in two ways. The finite difference approach gives

$$\gamma_{\mathbf{q}s} = -\left(\Delta\omega_{\mathbf{q}s}/\Delta V\right)/\left(\omega_{\mathbf{q}s}/V\right), \tag{III. 1}$$

with the crystal volume V.

From the perturbation theory using the third-order force constants as inputs, the mode-specific Gruneisen parameter is expressed as [8, 159]

$$\gamma_{\mathbf{q}s} = \frac{1}{6\omega_{\boldsymbol{qs}}^2}\sum_{\tau,\boldsymbol{R}'\tau',\boldsymbol{R}''\tau''}\sum_{\alpha\beta\gamma}\Psi^{\alpha\beta\gamma}_{0\tau,\boldsymbol{R}'\tau',\boldsymbol{R}''\tau''}\frac{\varepsilon^{\tau\alpha}_{\boldsymbol{qs}}\varepsilon^{\tau'\beta}_{\boldsymbol{q}'s'}}{\sqrt{M_\tau M_{\tau'}}}\exp(i\boldsymbol{q}\cdot\boldsymbol{R}')\,\boldsymbol{r}^{\gamma}_{\boldsymbol{R}''\tau''}, \tag{III.2}$$

where $(\boldsymbol{R},\tau,\alpha)$ refers to the degree of freedom corresponding to the α direction of the τ-th basis atom in the unit cell located at position $\boldsymbol{R}$, Ψ is the third-order anharmonic force constant, ε and $\boldsymbol{r}$ are the polarization vector component and equilibrium atomic position.

Figure III.3 shows the calculated mode-specific Gruneisen parameters of acoustic and low-lying optical (below the frequency gap at around 250 cm^{-1}) phonon modes for bulk MoS_2. These phonon modes account for more than 90% of its total thermal conductivity. Clearly, the results from these two computing methods are consistent with each other, confirming that our choice on the cutoff for the anharmonic interaction indeed gives converged results.

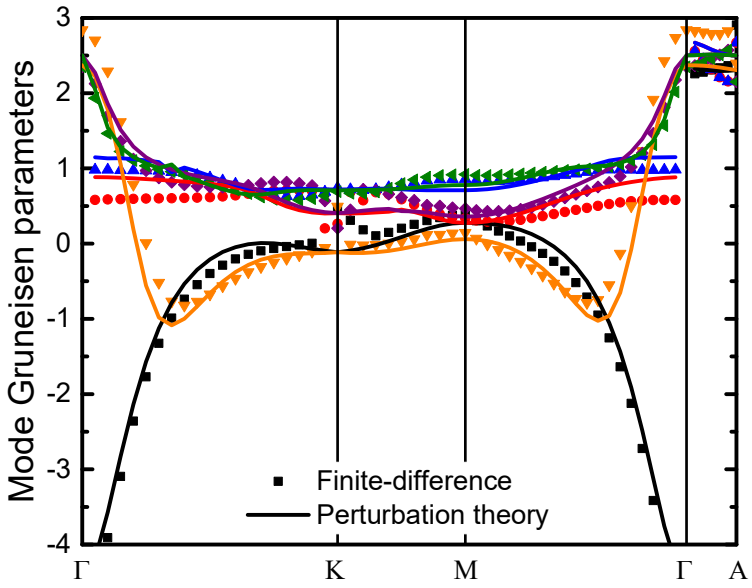

Figure III.3. Mode-specific Gruneisen parameters of acoustic and low-lying optical phonons of bulk MoS_2. Dots and lines represent the Grunesien parameters calculated from the finite-difference method and the perturbation theory, respectively. Different colors are assigned according to which branches the data represents (see Fig. III.2).

III.3 Thermal conductivity of single-layer TMDs

Table III.2 summarizes the calculated lattice constants for the eight TMDs studied in this work, which are in excellent agreement with the available measured values for monolayer [160] and bulk TMDs [161-163]. To report the values of thermal conductivity, the thicknesses of the monolayers, h, are also listed, which are defined as the measured cross-plane lattice constants or half of the lattice constants of the bulk materials, depending on 1T or 2H single-layer TMDs. We also examine the bonding stiffness of these materials by calculating their spring constant, K, which is

defined as the trace of the harmonic force constant tensor of the nearest neighboring atom pairs (the metal atom M and the chalcogenide atom X), and written as [164] $K = \phi_{MX}^{xx} + \phi_{MX}^{yy} + \phi_{MX}^{zz}$, where $\phi_{MX}^{\alpha\alpha}$ is the second derivatives of the energy with respect to the displacement of atoms M and X along the Cartesian axis α. Contradictory to the previous understanding that the bonding is weak in TMDs, the bonding in single-layer molybdenum and tungsten dichalcogenides are indeed surprisingly stiff, even stiffer than silicon with a spring constant of 9.7 eV/Å. In general, the sulfides are 15% stiffer than the selenides, while the molybdenum dichalcogenides are 4% less stiff than tungsten dichalcogenides. Considering that the difference in the bonding strength in the group of 2H TMDs is small, the mass of the basis atoms plays a key role in determine their phonon dispersion relations, which in term determines the related group velocity and thermal properties. Comparing to 2H TMDs, the bonding in the 1T zirconium and hafnium dichalcogenides is about 50% weaker than their molybdenum and tungsten counterparts.

Table III.2. Lattice constants and spring constants of single-layer TMDs from DFT calculations, and the lattice constants from literature.

material	lattice constant			thickness	spring constant
	a (Å) (DFT)	*a* (Å) (Exp. momolayer)	*a* (Å) (Exp. bulk)	*h* (Å) (Exp.)	*K* (eV/Å)
MoS_2	3.19	3.22[a]	3.16 [b]	6.15 [b]	11.2
WS_2	3.19	3.23[a]	3.15 [c]	6.16 [c]	11.7
$MoSe_2$	3.32	-	3.30 [b]	6.47 [b]	9.8
WSe_2	3.325	3.27[a]	3.28 [c]	6.48 [d]	10.2
ZrS_2	3.691	-	3.66 [d]	5.85 [d]	4.6
HfS_2	3.646	-	3.62 [d]	5.88 [d]	5.2
$ZrSe_2$	3.806	-	3.76 [d]	6.15 [d]	3.7
$HfSe_2$	3.771	-	3.73 [d]	6.14 [d]	4.2

a Ref[[160]]
b Ref[[161]]
c Ref[[162]]
d Ref[[163]]

Figure III.4 show the length-dependent thermal conductivity of MoS_2 at 300K calculated using both the iterative solution of PBTE and from SMRTA. Our SMRTA results are very close to Li *et al*'s calculations using a similar approach [138]. When the length of the monolayer sheet L is smaller than 30 nm, the difference between two approaches is less than 5%. This is because the dominant phonon scattering comes from elastic boundary scattering when the concept of relaxation time is applicable. However, as the length increases where the phonon-phonon scattering becomes dominant, SMRTA cannot distinguish the resistive Umklapp process and the normal process, which does not directly provide the resistance to the heat flow. The under-prediction of SMRTA becomes distinguishable when the scattering due to normal process is strong. For example, when L = 1 μm, the thermal conductivity from the iterative solution of the PBTE is 103 W/mK, which is ~25% higher than the value of 83 W/mK from SMRTA. Due to such non-negligible difference between the two methods, PBTE is strictly solved with the iterative approach in this work to accurately predict the thermal conductivity of TMDs. Although SMRTA tends to underestimate considerably the thermal conductivity of single-layer TMDs, the concept of phonon lifetime or scattering rate, that is used in SMRTA, of each phonon mode can still provide useful information on the strength of phonon-phonon scattering. We have thus still employ SMRTA when needed to qualitatively interpret the scattering mechanism in different materials.

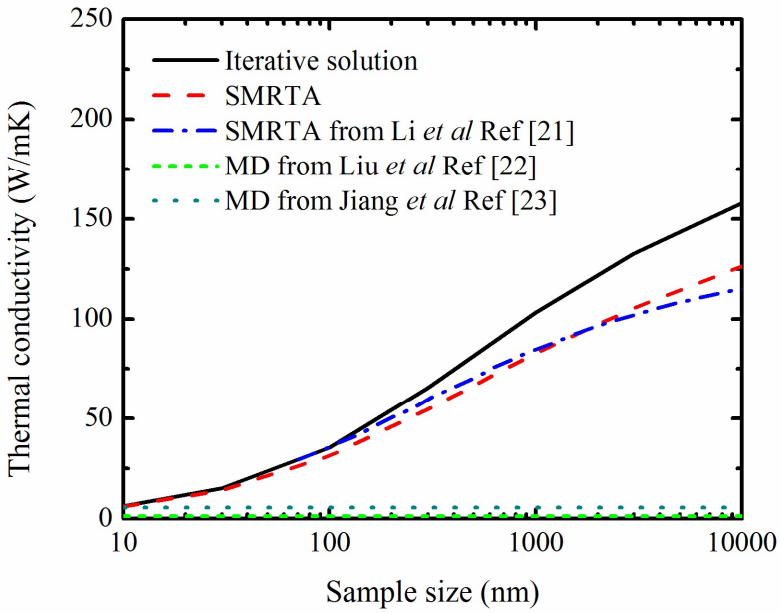

Figure III.4. The calculated thermal conductivity of MoS_2 at 300K as a function of sample size.

The calculated thermal conductivity of MoS_2 using MD simulations with empirical interatomic potentials [139, 140] is shown in Fig. III.2. Clearly MD simulations have predicted a far too low thermal conductivity value comparing to the first-principles calculations. Although some of the potentials used in MD can reasonably reproduce the phonon dispersion, the anharmonicity was not taken into account when the empirical potentials were developed. The low thermal conductivity prediction from MD indicates that the anharmonicity in these empirical potentials has been overestimated.

Figure III.5 shows the calculated thermal conductivities of TMDs with the sample size $L = 1\mu$m as a function of temperature, along with the available measurement data of single-layer TMDs. Among the four single-layer 2H TMDs, WS_2 is of the highest thermal conductivity, 142 W/mK at room temperature and then followed by MoS_2 (103 W/mK), $MoSe_2$ (54 W/mK) and

WSe_2 (53 W/mK). It is notable that the thermal conductivity of WS_2 is the highest among all TMDs studied and about 40% larger than that of MoS_2. The atomic mass of W is about twice as heavy as Mo. Table III.2 shows that the bonding in WS_2 is only ~ 4% stiffer than that in MoS_2 according to the spring constants. The large thermal conductivity of WS_2 is contradictory to the classical theory which would expect a smaller phononic thermal conductivity due to the much heavier atom mass and weaker bonding stiffness [96]. Figure III.6 shows the phonon dispersion of MoS_2 and WS_2. As expected, all the three acoustic branches of WS_2 are lower than that of MoS_2 due to the difference in atom mass and bonding stiffness between MoS_2 and WS_2. As a result, the group velocity and heat capacity of the acoustic phonons in MoS_2 are larger than WS_2, both of which facility the heat transport. However, much weaker phonon-phonon scattering is observed in WS_2 is than in MoS_2, especially for middle-range frequency phonon modes (50 cm^{-1} to 200 cm^{-1}) by examining the phonon scattering rate, as shown in Fig. III.7.

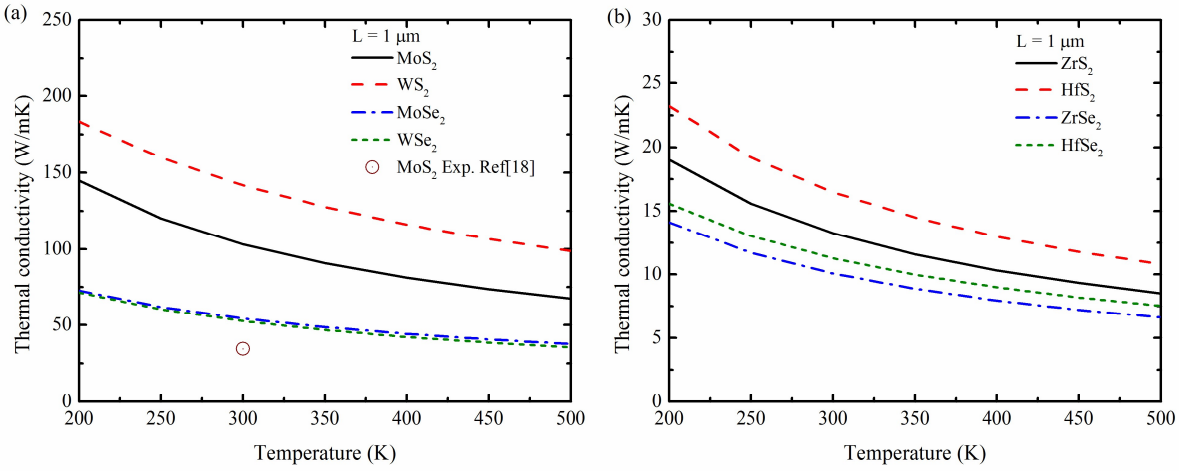

Figure III.5. The thermal conductivity of (a) 2H and (b) 1T TMD monolayers as a function of temperature.

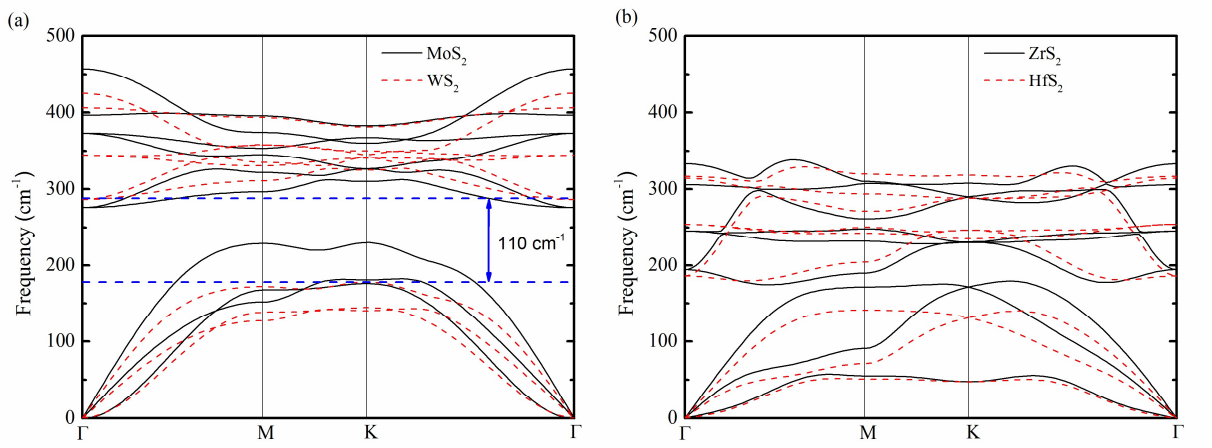

Figure III.6. Phonon dispersion of (a) MoS_2 and WS_2, and (b) ZrS_2 and HfS_2 calculated from the first-principles simulations.

In Figure III.6, we also observe a very large frequency gap between the optical and acoustic phonon branches in WS_2, due to the large mass difference of the basis atoms of WS_2. The frequency gap is as large as 110 cm^{-1}, which is close to the range of acoustic phonons of WS_2 (178 cm^{-1}), while the gap is only 45 cm^{-1} for MoS_2, much smaller than the range of acoustic phonons (230 cm^{-1}). Because of the large phonon frequency gap of WS_2, one important phonon scattering channel, the annihilation process of two acoustic phonon modes into one optical one (acoustic+acoustic->optical), becomes ineffective due to the requirement on energy conservation for phonon-phonon scattering, although such scatterings are not totally prohibited. The scattering through such scattering channel is usually the resistive Umklapp scattering [165]. As a result, the weaker phonon-phonon scattering rate is observed in WS_2 which renders to a much higher thermal conductivity.

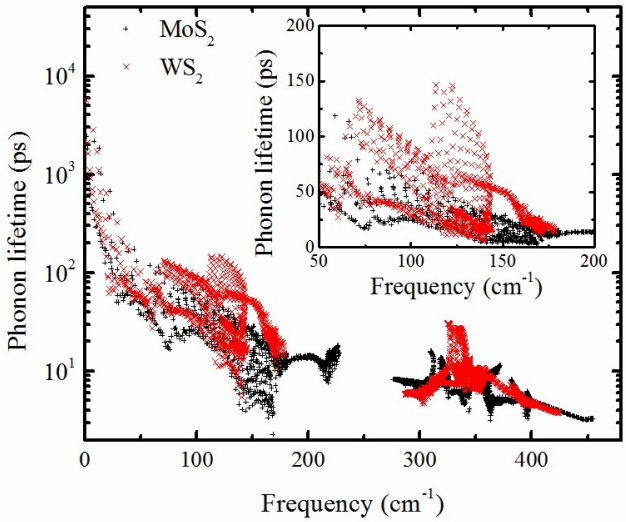

Figure III.7. Phonon lifetime of MoS_2 and WS_2 at 300K as a function of phonon frequency.

To further show that the large phonon frequency gap leads to the large thermal conductivity of WS_2, we shift the phonon frequency of each optical phonon mode downward by the same amount to reduce the frequency gap, and then recalculate the thermal conductivity of the WS_2-like material. Figure III.8 shows the calculated thermal conductivity as a function of the size of the phonon frequency gap. Clearly, the thermal conductivity monotonically decreases when the phonon frequency gap becomes smaller. In particular, when the frequency gap is the same as that of MoS_2, the thermal conductivity is reduced to 60 W/mK, a value even smaller than that in MoS_2. Recently, the first-principles calculations have been used to predict very high thermal conductivity of some three-dimensional bulk materials, such as Bas [165] and AlSb [17], primary due to a large frequency gap. Our simulations confirm that examining the acoustic-optical frequency gap could be a powerful search for 2D materials with high thermal conductivity. We also plot results calculated from SMRTA in Fig. III.8. The ratio between the thermal conductivities from the iterative solution and the SMRTA increases when the gap becomes large. This can be partially

attributed to less resistive Umklapp scattering through the channel of acoustic+acoustic->optical. This observation confirms the importance of fully solving the PBTE to accurately predict the thermal conductivity of TMDs.

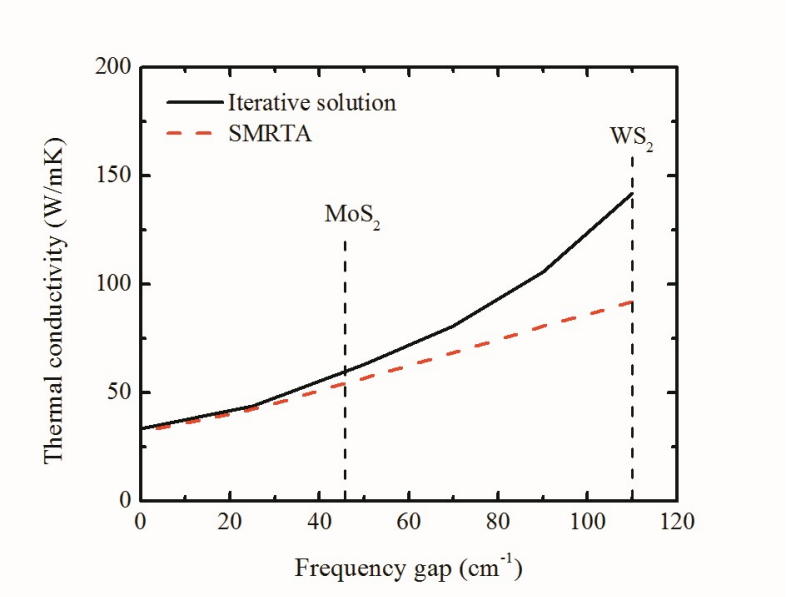

Figure III.8. Calculated thermal conductivity of WS_2-like material at 300K as a function of the frequency gap between acoustic and optical branches. The black dashed lines indicate the frequency gap of MoS_2 and WS_2.

Unlike the high thermal conductivity of 2H molybdenum and tungsten dichalcogenides, the thermal conductivities of zirconium and hafnium dichalcogenides are found to be much lower, ranging from 10 W/mK to 30 W/mK when the size of sample is 1 μm, as shown in Fig. III.6(b). To explore the origin of the low thermal conductivity of these materials, we examine phonon dispersion and phonon lifetime of 1T TMDs and compare them with 2H TMDs. Figure III.5(b) shows the phonon dispersion of ZrS_2 and HfS_2. The span of the phonon frequency is much smaller than 2H MoS_2 and WS_2, which could be attributed to the weak bonding stiffness. Figure III.9 show

the phonon lifetimes of both 2H and 1T TMDs. While the phonon lifetimes of 2H TMDs are all above 1 ps, the phonon lifetimes of 1T TMDs are almost one order-of-magnitude smaller than that of 2H TMDs. The strong scattering in 1T TMDs is also correlated to their relatively small range of the phonon frequency. In 1T TMDs, the separation between acoustic and the optical phonon branches is smaller, which results in much more frequent scattering between acoustic modes and optical modes. In addition, the strength of such scatterings is expected to be strong compared with the case in 2H TMDs, because the population of the lower-frequency optical phonon modes involving the scattering with acoustic modes is larger according to the Bose-Einstein statistics, and the elements of the three-phonon scattering matrix is larger due to it inversely proportional relation with the phonon frequency.

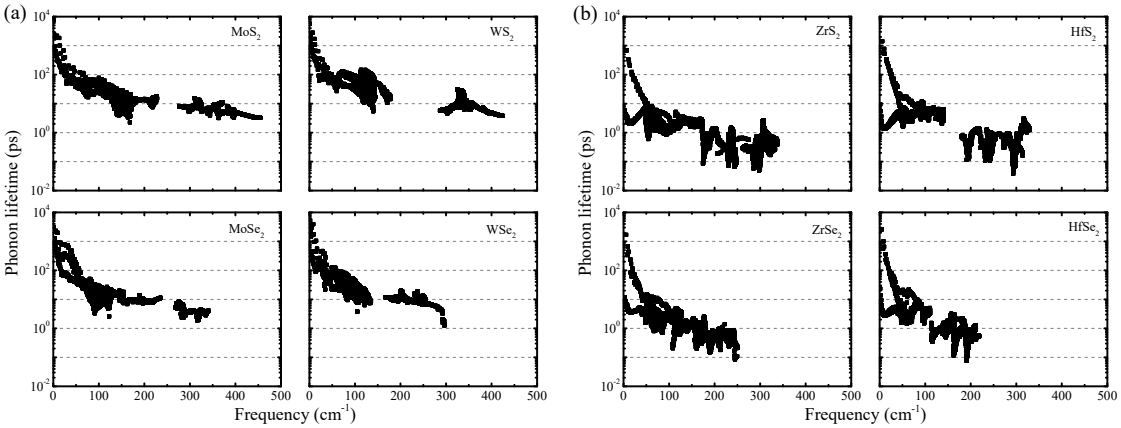

Figure III.9. Phonon lifetime for (a) 2H TMDs and (b) 1T TMDs.

III.4 Thermal conductivity of bulk MoS_2

Figure III.10 shows the calculated basal-plane thermal conductivity of an infinitely large bulk MoS_2 as a function of temperature, in comparison with the available experiment data. The basal-plane thermal conductivity of bulk MoS_2 made up of the naturally occurring Mo and S isotopes

decreases from 340 W/mK to 73 W/mK when the temperature increases from 100 K to 400 K, while the cross-plane thermal conductivity changes from 11.4 W/mK to 2.6 W/mK. At room temperature, the basal-plane thermal conductivity from our calculation is 98 W/mK, which falls in the range of 85-112 W/mK obtained from a recent pump-probe measurement [152]. The thermal conductivity of isotopically pure MoS_2 is also shown in Fig. III.10. Due to the absence of isotope scattering, the basal-plane thermal conductivity is 117 W/mK in the isotopically pure crystal, about 20% higher than the naturally occurring one.

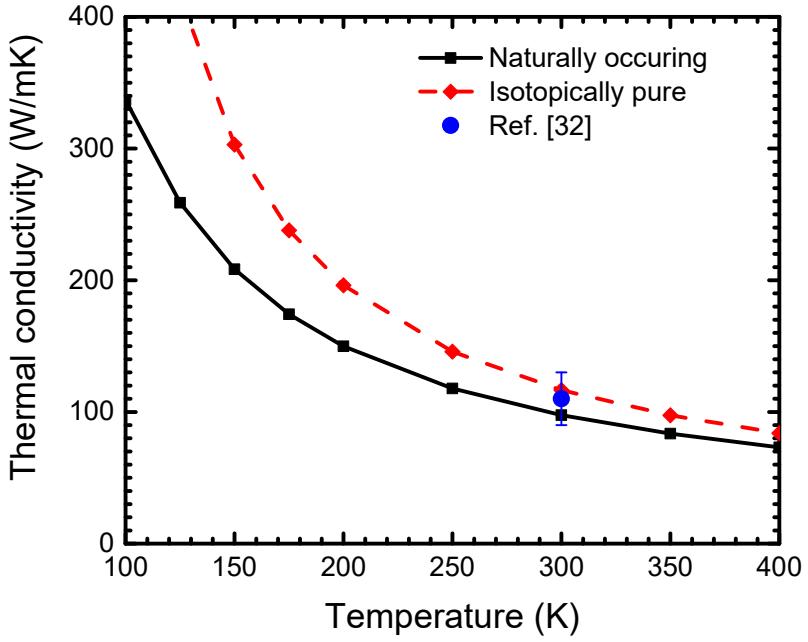

Figure III.10. Basal-plane thermal conductivity of bulk MoS_2 as a function of temperature. Blue dot is the experimental data from pump-probe measurement [152].

Figure III.11 shows the cross-plane thermal conductivity of bulk MoS_2. The cross-plane thermal conductivity of the naturally occurring MoS_2 is calculated to be 3.5 W/mK at room

temperature. We notice that the measured cross-plane thermal conductivity ranges from 2 W/mK to 2.5 W/mK using ultrafast laser-based pump-and-probe measurements [130, 152], which is consistently lower than the calculated value. This indicates that sample quality and measurement geometry could play an important role in the determination of the measured cross-plane thermal conductivity.

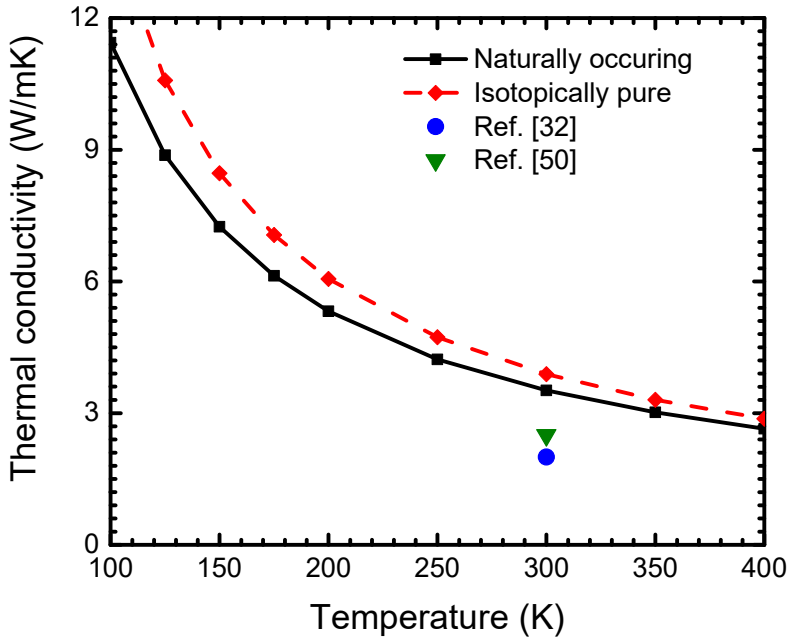

Figure III.11. Cross-plane thermal conductivity of bulk MoS_2 as a function of temperature. Blue and Green dots are the experimental data from pump-probe measurement [130, 152].

As shown above, our numerical results for basal-plane thermal conductivity are consistent with the measurements but those for cross-plane thermal conductivity are not. One possible explanation for this difference is that the thermal conductivity extracted from the pump-and-probe measurements is dependent on the modulation frequency [166]. The pump beam with a modulation frequency of ω_{pump} could only heat a limited region away from the surface heated by the beam

spot. The length scale of the heated region can be roughly estimated as the thermal diffusion depth $l_d = \sqrt{\kappa/\pi C \omega_{\text{pump}}}$ with the heat capacity of the material C (=1.89 J/cm^{3}K for bulk MoS_2). For basal-plane transport, we use a basal plane thermal conductivity of 100 W/mK to calculate the thermal diffusion length in the radial direction and it ranges from 1 μm to 4 μm when the frequency changes from 10 MHz to 1 MHz. Because beam spot size in the measurements is usually very large, for example, a 12-μm-in-diameter spot size was used in Ref. [152], the excited phonons will travel through a long distance in the order of 10 μm on average to the unheated region. This length is larger than or comparable to the mean free path of most of the heat-carrying phonons. Therefore, the phonon transport along the radial direction is diffusive and the measured basal-plane thermal conductivity is close to our calculations. But for phonon transport in the cross-plane direction, we find that the thermal diffusion length is only about 200-300 nm with the common modulation frequency $\omega_{\text{pump}} (\approx 10$ MHz) [152] employed in these experiments, along with the estimated cross-plane thermal conductivity of bulk MoS_2 , 2-5 W/mK. This indicates that the heat carried by the phonons with mean free paths larger than ~250 nm is suppressed in the pump-probe measurements. As a result, the deduced thermal conductivity from the pump-and-probe measurement has a lower value than its true thermal conductivity. To evaluate the contribution from these long mean free path phonons, we calculate the cross-plane thermal conductivity of MoS_2 by leaving the two reservoirs 250 nm apart, mimicking the phonon transport across the heating region in the pump-and-probe measurements. We find that the thermal conductivity from this simulation with short distance is about 2.1 W/mK, which indeed fall into the range of the measured cross-plane thermal conductivity of MoS_2.

III.5 Layer-dependent thermal conductivity of MoS_2

After the validation of the theoretical calculations on bulk MoS_2 with the insights to the pump-and-probe measurements, we study the thermal conductivity of single- and few-layer MoS_2. To mimic the measurement conditions for the in-plane thermal conductivity, where the characteristic size of the suspended samples is usually in the order of several microns, we impose a sample size of 10 μm to include boundary scattering to solve the PBTE. Figure III.12 shows the calculated thermal conductivity of MoS_2 as a function of layer number at room temperature, in comparison with the recent measurement results [135, 136, 150-152]. For naturally occurring MoS_2, the calculated thermal conductivity values are 138 W/mK, 108 W/mK, 98 W/mK and 94 W/mK for single-layer, bi-layer, tri-layer and bulk samples, respectively. For the isotopically pure samples, the thermal conductivity values are consistently higher at 155 W/mK, 125 W/mK, 115 W/mK, and 112 W/mK, respectively. It is evident that the thermal conductivity of few-layer MoS_2, both naturally occurring and isotopically pure, decreases with the thickness from single layer to three layers, and the thermal conductivity of the tri-layer MoS_2 almost approaches to the bulk value.

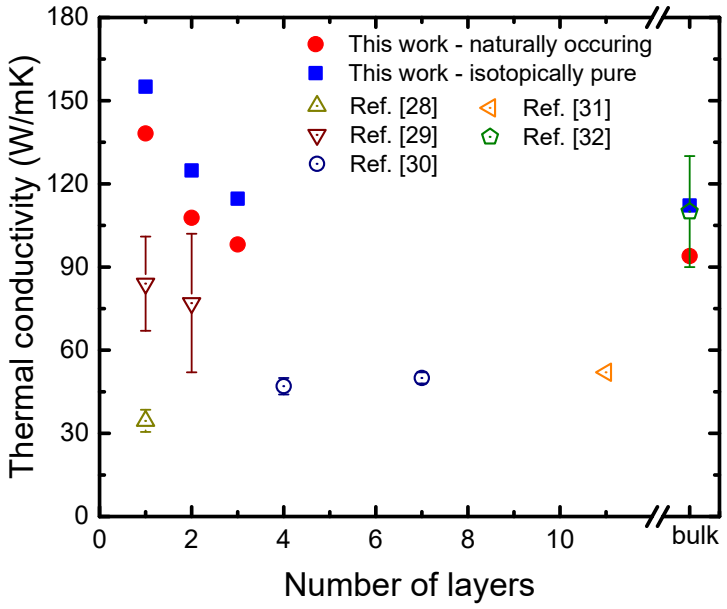

Figure III.12. Room-temperature basal-plane thermal conductivity of MoS_2 as a function of layer numbers.

To understand the mechanisms of thermal conductivity reduction from single-layer MoS_2 to thicker ones, we examine the contributions from the changed phonon dispersion curves of MoS_2 with one to three layers. Figure III.13 shows the dispersion curves of acoustic and low-frequency optical branches (< 250 cm^{-1}), which together contribute to more than 90% of the total thermal conductivity. In the single-layer MoS_2, there are three acoustic branches, including one longitudinal acoustic (LA) branch, one transverse acoustic (TA) branch and one flexural acoustic (ZA) branch, whose frequencies becomes zero as the wavenumber q approaches to zero, shown as the black solid curves in both Fig. III.13(a) and III.13(b). For N-layer MoS_2 (N=2,3), there are $3N$-3 low-frequency optical phonon branches beneath the frequency gap around 250 cm^{-1} in addition to the 3 acoustic branches due to more basis atoms involved. It is clearly seen that the three groups of phonon branches, each of which involves N branches are almost degenerated/overlapped with

each other for the region away from the first Brillouin zone center, which is similar to the observation on multi-layer graphene. We denote these phonon branches in multi-layer MoS_2 as LA_i, TA_i and ZA_i branches (i = 1,.., N), where LA_i (TA_i and ZA_i) are sorted ascendingly according to the phonon frequency at $q = 0$.

For multi-layer graphene, the N branches in each groups become nondegenerated near the first Brillouin zone center [64, 145, 167]. While the acoustic branch has a zero frequency at the zone center, the other N-1 (optical) branches gradually become less dispersive (for TA_i and LA_i branches) or even flat (for ZA_i branches) as $q \to 0$. Unlike multi-layer graphene, the phonon dispersion in multi-layer MoS_2 are dramatically different. Two acoustic branches and N-2 optical branch are found in the group of ZA_i while one acoustic branch and N-1 optical branches in the group of TA_i, and even more interestingly, all N LA_i are optical modes. In Fig. III.13(a) and (b), we also observe kinks, indicated by arrows, occur at $q \approx 0.05\ (2\pi/a_0)$ on the ZA_i branches, changing the shapes of ZA_i and LA_i branches. Near each kink, the corresponding ZA_i branch experiences a flat-to-dispersive transition as q decreases. The ZA_2 even becomes an acoustic branch with a large sound velocity due to the transition. In contrast, LA_i branches turn from dispersive to flat. As a result, the LA_2 and the ZA_2 in bi-layer MoS_2, as well as the LA_1 and the ZA_2, or the LA_3 and the ZA_3 in tri-layer MoS_2, do not cross each other. Similar phenomena have been also reported in other materials [168, 169], and are called avoided-crossing in literature [168]. For example, in some caged structures encapsulating guest atoms, such as clathrates [168], a dispersive acoustic-phonon branch and a flat branch corresponding to the movement of guest atom do not cross each other but transit to be flat and dispersive, respectively. The avoided-crossing in the few-layer MoS_2 reduces the group velocity of the acoustic phonon modes nearby. In addition to reduced group velocities of the phonon modes near the avoided-crossing, the long-wavelength

optical phonon modes in few-layer MoS_2 generally have slightly smaller group velocities than the acoustic phonons, reducing the average group velocity for the heat carrying phonons compared with the single-layer MoS_2.

One might expect that such changes in the phonon dispersion from one-layer to multi-layer MoS_2 could lead to significant change on thermal conductivity, due to the lower group velocity. To test this hypothesis, we recalculate the thermal conductivity of naturally occurring bi-layer and tri-layer MoS_2 using their own phonon dispersion as shown in Figure III.13, but ignoring the third-order anharmonic force constants corresponding to the interlayer interaction and assigning their intralayer anharmonic force constants with the anharmonic force constants of single-layer MoS_2. The recalculated thermal conductivity of bi-layer and tri-layer MoS_2 is only 12% and 15% lower than the single-layer one, respectively, which is definitely smaller than 22% and 29% obtained from the calculations using their own anharmonic force constants. Apparently, the change in phonon dispersion is an important factor to reduce the thermal conductivity from a higher value at the single layer to the multi-layer MoS_2. However, phonon dispersion change is not the single factor. The change of anharmonic force constants could be as important in reducing the thermal conductivity values from single-layer to multi-layer MoS_2.

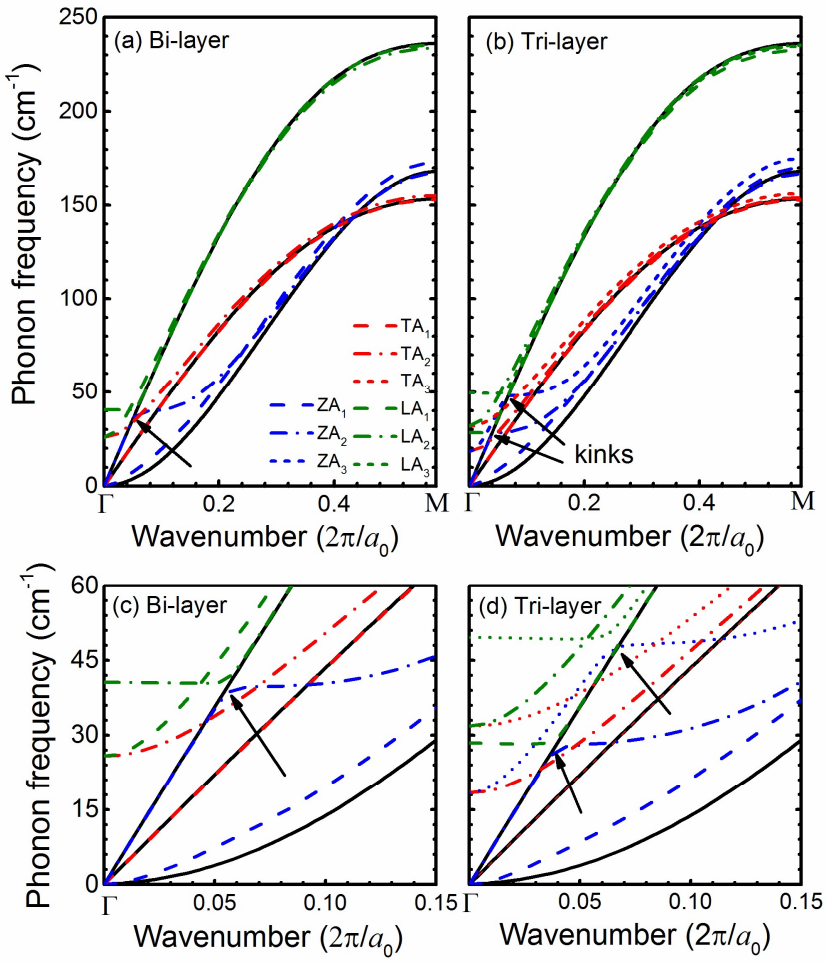

Figure III.13. Phonon dispersion of few-layer MoS_2. Black lines are the dispersion for single-layer MoS_2. Blue, red and green lines refer to the ZA_i, TA_i and LA_i branches, respectively. Dash, dash-dot and short-dash lines refer to i=1, 2, 3, respectively.

Figure III.14 shows the phonon scattering rate, or the inverse of phonon lifetime, of the acoustic and low-lying optical modes for single-layer and bi-layer MoS_2 along the Γ-K direction, calculated using their respective third-order anharmonic force constants. Clearly the scattering rates for the in-plane phonon modes (TA_i and LA_i) in bi-layer MoS_2, except the modes near the zone center, are almost unchanged compared with their counterparts (TA_1 and LA_1) in single-layer MoS_2. Since

there is only a small fraction of phonons near the zone center, the total thermal conductivity of TA_i and LA_i branches should be very close to that of TA_1 and LA_1 in single-layer MoS_2.

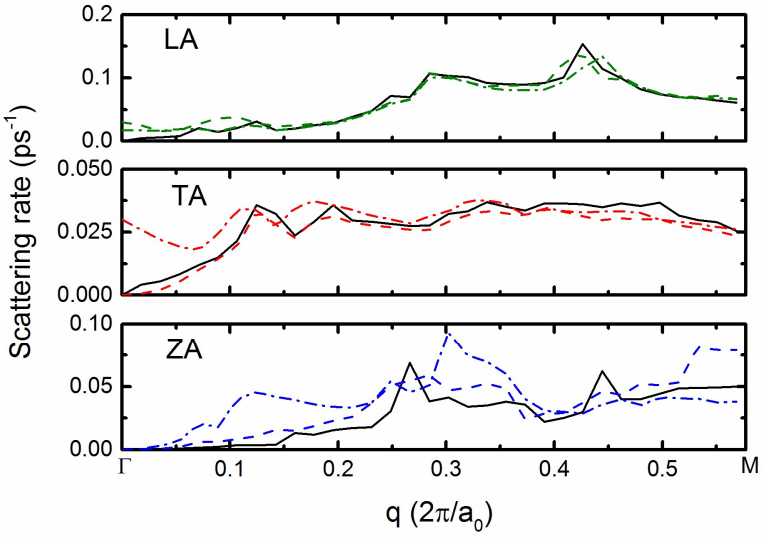

Figure III.14. Scattering rates of the acoustic and low-lying optical branches of phonons in single-layer and bi-layer MoS_2. Black lines are the scattering rates for single-layer MoS_2. Blue, red and green lines refer to the ZA_i, TA_i and LA_i branches, respectively. Dash and dash-dot lines refer to i =1, 2, respectively.

In comparison, the scattering rates of ZA_i phonons in bi-layer MoS_2 are significantly larger than ZA_1 phonons in single-layer MoS_2 throughout the entire first Brillouin zone. This could be understood by closely examining the third-order anharmonic force constants. Assuming that *n*, *m* and *l* refer to any Mo atoms in the same layer, the force constants, $\psi_{n,m,l}^{z,z,z}$, which are the third-order derivatives of the total energy of the crystal with respect to the *z* coordinates of atom *n*, *m* and *l*, are found to be zero in single-layer MoS_2 because of the mirror symmetry. This means that there is no anharmonicity induced by the relative motion among the three Mo atoms along z direction.

Since the dominating atomic motion of ZA phonons is along z direction, the scattering rates of these ZA phonon modes are thus very small. When two MoS_2 monolayers are in contact with each other, the mirror symmetry breaks down. As a result, the third-order anharmonic force constants $\psi_{n,m,l}^{z,z,z}$ become non-zero, leading to stronger scattering of ZA_i phonons in bi-layer MoS_2. In addition to the third-order anharmonic force constants involving the out-of-plane motion of three Mo atoms, the third-order anharmonic force constants corresponding to the interlayer interaction also contribute to the anharmonicity, which is absent in the single-layer MoS_2.

The observation of low scattering rate of ZA modes in single layer MoS_2 induced by mirror symmetry is indeed similar to graphene. In graphene, the scattering with odd number of out-of-plane modes, such as ZA + TA -> LA and ZA + ZA -> ZA, are totally prohibited due to its mirror symmetry [67]. However, there is still a notable difference between MoS_2 and graphene. Because the atom vibration of ZA modes also involves S atoms, the forbidden scattering channels in graphene are not totally forbidden in MoS_2. Therefore, while the thermal conductivity reduction from single-layer graphene to bi-layer graphene is mainly attributed to the stronger phonon scattering in bi-layer graphene due to the breakdown of the symmetry selection rule, which accounts for 70% reduction [145], both the change of phonon dispersion and the enhanced phonon scattering strength are important for explaining the thermal conductivity reduction from single layer to multilayer MoS_2.

III.6 Summary of this chapter

In summary, we have used the first-principles-based PBTE approach to systematically predict the phononic thermal conductivity of eight typical single-layer TMDs. The validity of the single-

mode relaxation time approximation to predict the thermal conductivity of TMDs is also assessed by comparing with the iterative solution of the phonon Boltzmann transport equation. We found that the thermal conductivities of MoS_2 and WS_2 are as high as 103 W/mK and 142 W/mK when the size of the sample is 1 μm, respectively. The large thermal conductivity of WS_2 can be attributed to the large acoustic-optical frequency gap due to the large mass difference of W and S, which makes inefficient scattering among acoustic and optical phonon modes. The thermal conductivities of 1T-type TMDs are generally smaller than the 2H-type TMDs due to the low bonding stiffness.

The basal-plane thermal conductivity of MoS_2 is found to monotonically reduce from 138 W/mK to 98 W/mK for naturally occurring MoS_2 with a sample size of 10 μm, and from 155 W/mK to 115 W/mK for isotopically pure MoS_2, when its thickness increases from one layer to three layers. The thermal conductivity of tri-layer MoS_2 approaches to that of bulk MoS_2. Both the change of phonon dispersion and the thickness-induced anharmonicity are important for explaining such a thermal conductivity reduction. The increased anharmonicity in bi-layer MoS_2 results in stronger phonon scattering for ZA_i modes, which is linked to the breakdown of the symmetry in single-layer MoS_2.

CHAPTER IV PHONON TRANSPORT IN TWO-DIMENSIONAL MOLYBDENUM TUNGSTEN ALLOY EMBEDDED WITH NANODOMAINS

IV.1 Introduction

Two-dimensional (2-D) transition metal dichalcogenides (TMDs) have shown numerous interesting physical and chemical properties [41, 42, 170], making them promising materials for electronic, optoelectronic, and energy applications. For many of these technological applications, materials are expected to possess a few desired functions or properties simultaneously, which can hardly be fulfilled by the intrinsic properties of a single material. Therefore, various attempts, such as reducing dimensions [171, 172], intercalation [173, 174], heterostructuring[175-177] and alloying [178, 179], have been made to tune the electronic and optical properties of 2-D TMDs to expand the applicability of 2-D TMDs for different applications.

Phonon and thermal properties of 2-D TMDs is of great interest because it is highly relevant to the functionality, performance and reliability of 2-D TMD-enabled devices. Many efforts have been devoted to investigate the thermal conductivity of 2-D TMDs, both theoretically [138, 156, 180] and experimentally [134-136, 181]. While the 2-D TMDs with high thermal conductivity might be beneficial to thermal management and electronic cooling, those with low thermal conductivity could be used as the thermal barrier materials [182] and thermoelectric materials [51]. Tuning the thermal conductivity of 2-D TMDs could significantly broaden their applications [143].

For example, recent experiments showed that MoS_2 is of a relatively high power factor [183, 184]. Apparently if the thermal conductivity of 2-D MoS_2 can be suppressed without significant change in power factor, it could be a promising thermoelectric material.

Inspired by the so-called "nanoparticle-in-alloy" approach used to reduce the thermal conductivity of three-dimensional (3-D) bulk materials, *i.e.,* nanocomposites [48, 49, 185], one might expect very low thermal conductivity of 2-D TMD alloys when embedded with nanodomains. Interestingly, both 2-D MoS_2-based alloys [178, 179] and heterostructures with triangular nanodomains have been recently synthesized [175-177], which laid the foundation for synthesizing 2-D TMD alloys embedded with nanodomains. However, it is unclear how low the thermal conductivity can be achieved using the "nanodomains in 2-D alloy" approach. This calls for a fundamental study on how alloying and embedding nanodomains affect phonon transport and thermal conductivity of 2-D TMDs.

In this chapter, we study the lattice (phonon) thermal conductivity of single-layer $Mo_{1-x}W_xS_2$ alloy and $Mo_{1-x}W_xS_2$ alloy embedded with triangular WS_2 nanodomains. Since MoS_2 and WS_2 are almost lattice matched [156], the nanostructures we studied here could be dislocation free and are expected to retain a relatively high power factor without significantly shortening electron mean free paths [48, 49, 185]. The first-principles-based Pierels-Boltzmann transport equation (PBTE) approach is employed to calculate the thermal conductivity of the nanostructures. The phonon scattering mechanisms, including three-phonon scattering, phonon-alloy scattering and phonon-nanodomain scattering, are all accounted for in the solution of the PBTE. The phonon scattering rates due to both alloying and embedding nanodomains are evaluated by the Green's function approach [186, 187]. The effects of area fraction, nanodomain size and the composition of alloy on the thermal conductivity are investigated. The thermal conductivity was found to be reduced to

one-tenth of the defect-free single-layer MoS_2 mainly due to the strong phonon-alloy scattering. Nanodomains can also play a role in thermal conductivity reduction.

IV.2 Numerical methods

IV.2.1 Pierels-Boltzmann transport equation for lattice thermal conductivity

Figure IV.1 shows a single-layer $Mo_{1-x}W_xS_2$ alloy embedded with triangular WS_2 nanodomains lying in the *x*-*y* plane. A typical atomic configuration for the alloy with nanodomains is also presented in Fig. IV.1. Assuming that all the nanodomains are of the same size but randomly embedded, the 2-D crystal is then characterized by three parameters, including the composition of alloy, *x*, the area fraction, f^{ND}, and the side length, *a*, of WS_2 nanodomains. $f^{\mathrm{ND}}/A^{\mathrm{ND}}$ defines the number density of nanodomains per unit area N^{ND}, where A^{ND} is the area of each nanodomain.

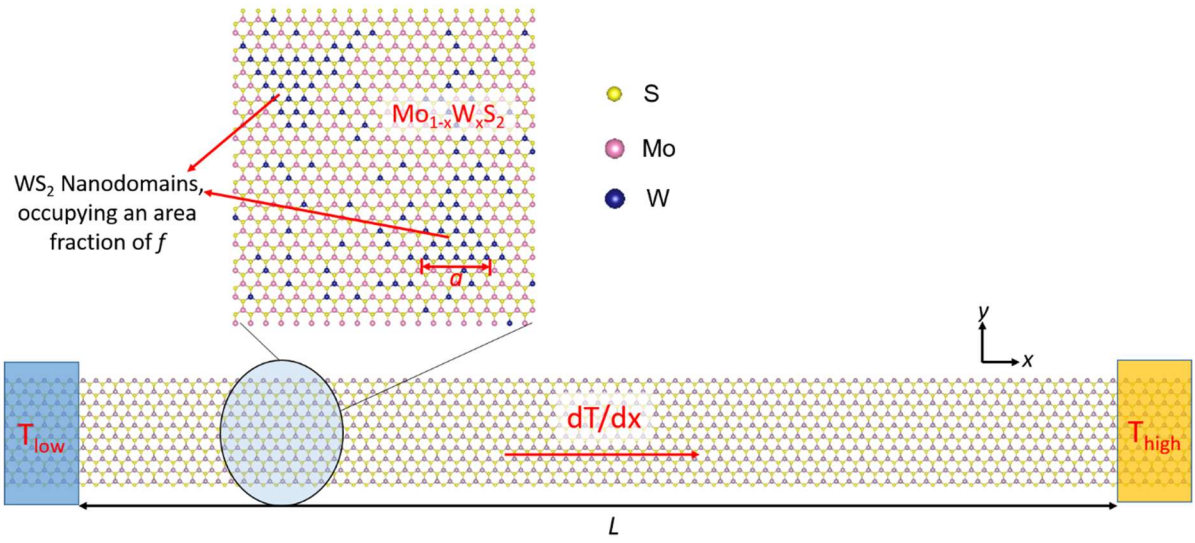

Figure IV.1. The schematic of the simulation domain. The inset shows a typical atomic configuration for the $Mo_{1-x}W_xS_2$ alloy embedded triangular WS_2 nanodomains.

To calculate the in-plane thermal conductivity of the 2-D materials, a small temperature difference ΔT is applied to the two ends of the monolayer with a distance L apart, resulting in a temperature gradient along x direction, dT/dx. The effective thermal conductivity can then be expressed as the summation of the thermal conductivity contributed by each phonon mode in first Brillouin zone, and is written as [155, 188]

$$\kappa^{xx} = \frac{1}{(2\pi)^2 h}\sum_s \int \hbar\omega_{\mathbf{q}s} v^x_{\mathbf{q}s} n^0_{\mathbf{q}s}\left(n^0_{\mathbf{q}s}+1\right)F_{\mathbf{q}s}\, d\mathbf{q}, \tag{IV.1}$$

where h is the thickness of the 2-D crystal, $\hbar$ is the Planck constant, $\mathbf{q}s$ stands for the s-th phonon mode with $\hbar\mathbf{q}$ momentum, ω, v and n^0 are the phonon frequency, group velocity and equilibrium phonon population, respectively, which are determined by the phonon dispersion relation of the material. $F_{\mathbf{q}s}$ is the mode-specific deviation function, representing the difference of non-equilibrium phonon population of mode $\mathbf{q}s$, $n_{\mathbf{q}s}\left(=n^0_{\mathbf{q}s}+n^0_{\mathbf{q}s}\left(n^0_{\mathbf{q}s}+1\right)\frac{dT}{dx}F_{\mathbf{q}s}\right)$, from equilibrium population $n^0_{\mathbf{q}s}$. The deviation function can be solved from the PBTE, which describes the balance between phonon diffusion and phonon scatterings due to various scattering mechanisms. Here, we consider the three-phonon scattering due to the anharmonicity of interatomic forces, phonon-boundary scattering, phonon-alloy scattering and phonon-nanodomain scattering, and the corresponding PBTE is expressed as [20, 155]

$$v^\alpha_{\mathbf{q}s}\frac{\partial n^0_{\mathbf{q}s}}{\partial T} = \sum_{\mathbf{q}'s',\mathbf{q}''s''}\left[W^{\mathbf{q}''s''}_{\mathbf{q}s,\mathbf{q}'s'}\left(F^\alpha_{\mathbf{q}''s''}-F^\alpha_{\mathbf{q}'s'}-F^\alpha_{\mathbf{q}s}\right)+\frac{1}{2}W^{\mathbf{q}'s',\mathbf{q}''s''}_{\mathbf{q}s}\left(F^\alpha_{\mathbf{q}''s''}+F^\alpha_{\mathbf{q}'s'}-F^\alpha_{\mathbf{q}s}\right)\right]+\sum_{\mathbf{q}'s'}W^{\text{Alloy}}_{\mathbf{q}s,\mathbf{q}'s'}\left(F^\alpha_{\mathbf{q}'s'}-F^\alpha_{\mathbf{q}s}\right)+\sum_{\mathbf{q}'s'}W^{\text{ND}}_{\mathbf{q}s,\mathbf{q}'s'}\left(F^\alpha_{\mathbf{q}'s'}-F^\alpha_{\mathbf{q}s}\right)-\frac{n^0_{\mathbf{q}s}\left(n^0_{\mathbf{q}s}+1\right)F^\alpha_{\mathbf{q}s}}{L/2\left|v^\alpha_{\mathbf{q}s}\right|}, \tag{IV.2}$$

where $W^{\mathbf{q}''s''}_{\mathbf{q}s,\mathbf{q}'s'}$ and $W^{\mathbf{q}'s',\mathbf{q}''s''}_{\mathbf{q}s}$ are the transition probabilities for three-phonon annihilation and decay processes, and $W^{\text{Alloy}}_{\mathbf{q}s,\mathbf{q}'s'}$ and $W^{\text{ND}}_{\mathbf{q}s,\mathbf{q}'s'}$ are the transition probabilities for phonon-alloy and

phonon-nanodomain scattering processes. The last term in Eq. (IV.2) represents the phonon-boundary scattering due to the limited length of the sample L.

Since atoms in alloy are randomly distributed, it is ambiguous to define the phonon dispersion and other phonon properties of the alloy that are required in Eq. (IV.1) and Eq. (IV.2). The virtual crystal approximation is employed to take into account the alloy effect [189], where the Mo or W atoms in the alloy are replaced by virtual atoms with an atomic mass of $(1-x)M_{\mathrm{Mo}} + xM_{\mathrm{W}}$. Here the lattice parameter and inter-atomic force constants of the virtual crystal are set according to the composition average of the quantities possessed by MoS_2 and WS_2. The optimized crystal structures and the inter-atomic force constants of both MoS_2 and WS_2 are obtained from the first-principles calculations. The phonon dispersion of the virtual crystal is then computed with the obtained atomic masses and the second-order harmonic force constants of the virtual crystal. Under the virtual crystal approximation, the transition probabilities, $W_{\mathbf{q}s,\mathbf{q}'s'}^{\mathbf{q}''s''}$ and $W_{\mathbf{q}s}^{\mathbf{q}'s',\mathbf{q}''s''}$, in Eq. (IV.2) can be straightforwardly computed using the Fermi's golden rule with the third-order force constants of the virtual crystal as inputs. The expressions of $W_{\mathbf{q}s,\mathbf{q}'s'}^{\mathbf{q}''s''}$ and $W_{\mathbf{q}s}^{\mathbf{q}'s',\mathbf{q}''s''}$ are given in in Section II.2.

IV.2.2 Green's function approach for phonon-alloy and phonon-nanodomain scattering rates

Unlike the calculation of inelastic phonon-phonon scattering rates which is quite standard practice these days, it is more challenging to estimate the strengths of elastic scatterings, including phonon-alloy scatterings and phonon-nanodomain scatterings, since they are very sensitive to the detailed atomic configurations of the lattice imperfections. Compared to the virtual crystal, the

randomly distributed Mo and W atoms in the alloy serve as independent impurities of the virtual crystal, which scatter phonons. We note that the distribution of the impurities might lead to phonon interference effects which can result in a different thermal conductivity, but such effects are not considered here. In this work, we employed an assumption of random and uniform distribution of impurities, similar to the many previous theoretical works for the prediction of the thermal conductivity of a few alloys [19, 90] where the theoretical prediction were shown to be consistent with experimental measurements. The scattering strength due to phonon-alloy scattering, $W_{\mathbf{q}s,\mathbf{q}'s'}^{\mathrm{Alloy}}$, can then be decomposed into two parts, one due to the Mo impurities, $W_{\mathbf{q}s,\mathbf{q}'s'}^{\mathrm{Alloy,Mo}}$, and the other due to the W impurities, $W_{\mathbf{q}s,\mathbf{q}'s'}^{\mathrm{Alloy,W}}$. When WS_2 nanodomains are embedded in the alloy, the W clusters in the nanodomains become another type of scatter centers in the virtual crystal leading to the scattering with the rate of $W_{\mathbf{q}s,\mathbf{q}'s'}^{\mathrm{ND}}$. The main effects of these three types of scattering centers result in the mass and force field variation in the virtual crystal, both of which serve as the perturbations on the lattice vibration of the virtual crystal. Since the difference of the bonding stiffness in MoS_2 and WS_2 is quite small (~4%) [156] compared with the mass difference between Mo and W atoms (~90%), we expect that the phonon scattering rate caused by the effects of force field variance is much smaller compared with that caused by mass variance. In fact, we can make a simple estimation on the ratio between phonon scattering rates due to the difference in the bonding stiffness and due to the atomic mass difference. According to the Klemens' theory [190] for a point defect with respect to atom i, the ratio is expressed as $2[((g_i - g)/g)/((M_i - M)/M)]^2$, where g_i is the average stiffness constant of the neareast-neighbor bonds from the impurities to the host lattice, g is the average stiffness constant for host atoms, M_i and M are the mass of the impurity and the host atom. From the simple calculation, the ratio is found to be smaller than 0.5% when a

W atom is inserted into MoS_2. To consider the force field variation after nanodomains are included, one has to perform the first-principles calculations with large supercells or employ higher-order force constant model [191] to obtain the interatomic force constants with respect to the atoms in/near the nanodomains. Considering the weak scattering caused by force field variance, in this work only the mass-difference-induced phonon scattering is taken into account when evaluating the phonon scattering rates due to alloy disorder and nanodomains.

We employ the Green's function approach to calculate the phonon scattering rates due to alloying and nanodomain embedding. This method takes into account fully the changes of dynamical matrix of the medium (virtual crystal) when scattering centers are introduced and thus could accurately estimate the strengths of elastic scatterings, including the phonon-alloy and phonon-nanodomain scatterings, as those applied to study the elastic phonon scattering due to Si/Ge nanoparticles in SiGe alloy [192] and due to vacancy defects in diamond [193]. The phonon scattering strength due to a specific type of scattering centers, *j*, is given by [192]

$$\mathrm{W}^{j}_{\mathbf{q}s,\mathbf{q}'s'} = N^{j}\frac{\Omega\pi}{2\omega^{2}_{\mathbf{q}s}}\left|\langle \mathbf{q}s|\mathbf{T}_{j}\left(\omega^{2}_{\mathbf{q}s}\right)|\mathbf{q}'s'\rangle\right|^{2}\delta\left(\omega_{\mathbf{q}s}-\omega_{\mathbf{q}'s'}\right), \quad \text{(IV. 3)}$$

where $N^{j}(=f^{j}/A^{j})$ is number density of *j*-type scattering centers with the area fraction of the scattering centers f^{j} and the total area of the unit cells occupied by each scatter center A_j, Ω is the volume into which the phonon eigenstates $|\mathbf{q}s\rangle$ are normalized, and $\mathbf{T}_j$ is the scattering matrix corresponding to the *j*-type scattering centers. While the area fraction for nanodomains is f^{ND}, the area fraction is $(1-x)(1-f^{\mathrm{ND}})$ and $x(1-f^{\mathrm{ND}})$ for Mo impurities and W impurities, respectively. The scattering matrix, $\mathbf{T}$, is related to the perturbation matrix, $\mathbf{V}$, which is the difference between the dynamical matrix of the alloy embedded with nanodomains (perturbated crystal) and that of the virtual crystal one (unperturbated crystal), and the Green's function of the virtual crystal, $\mathbf{g}^{+}$. The *T* matrix is expressed as

$$\mathbf{T}_j(\omega^2) = [\mathbf{I} - \mathbf{V}\mathbf{g}^+]^{-1}\mathbf{V}. \quad \text{(IV.4)}$$

Since only the mass difference is considered and the force field difference is ignored in this work, all of the non-zero elements of the perturbation matrix are the diagonal elements corresponding to the *i*-th degrees of freedom associated with the atom τ that has a different mass M_τ from the virtual atom with a mass of M_0. The non-zero elements of the matrix is given by [192]

$$\mathbf{V}_{ii} = -\frac{M_\tau - M_0}{M_0}\omega^2. \quad \text{(IV.5)}$$

The Green's function component with respect to any two degrees of freedom *i* and *j*, is written as [186]

$$\mathbf{g}_{ij}^+(\omega^2) = \lim_{z\to\omega^2+0^+} \sum_{\mathbf{q}s} \frac{\langle i|\mathbf{q}s\rangle\langle \mathbf{q}s|j\rangle}{z-\omega_{\mathbf{q}s}^2}. \quad \text{(IV.6)}$$

The Green's function of unperturbated 3-D crystals can be numerically evaluated by the analytical tetrahedron method proposed by Lambin and Vigneron [194].

With all scattering terms in Eq. (IV.2) are determined, the set of linear equations Eq. (IV.2), with respect to $F_{\boldsymbol{qs}}^{\alpha}$, is then self-consistently solved using the iterative method. Here we employed the biconjugate gradient stabilized method [101], a variant of the conjugate gradient algorithm, to iteratively solve Eq. (IV.2). In our calculation, we use 65×65×1 q-points to sample the reciprocal space for phonon scattering and thermal conductivity calculations respectively, which ensures the presented in-plane thermal conductivity data are converged, with less than 2% difference if the meshes are further refined.

IV.3 Thermal conductivity of $Mo_{1-x}W_xS_2$ alloy

With the phonon scattering rates due to alloying and nanodomain embedding calculated, the thermal conductivity of the alloy embedded with nanodomains can then be straightforwardly calculated using PBTE, i.e., Eq. (IV.2). Figure IV.2(a) shows the calculated thermal conductivity of $Mo_{1-x}W_xS_2$ alloy with a sample length of 10 μm. It is found that the thermal conductivity reduces from 155 W/mK to around 25 W/mK when the composition of W, x, increases from 0% to 30% while the thermal conductivity is almost unchanged as x is in the range between 30% and 70%. Such a U-shape dependence of thermal conductivity on the composition is quite typical for alloys, as seen in 3D alloys such as $Si_{1-x}Ge_x$ [189] and $Mg_2Si_{1-x}Sn_x$ [195].

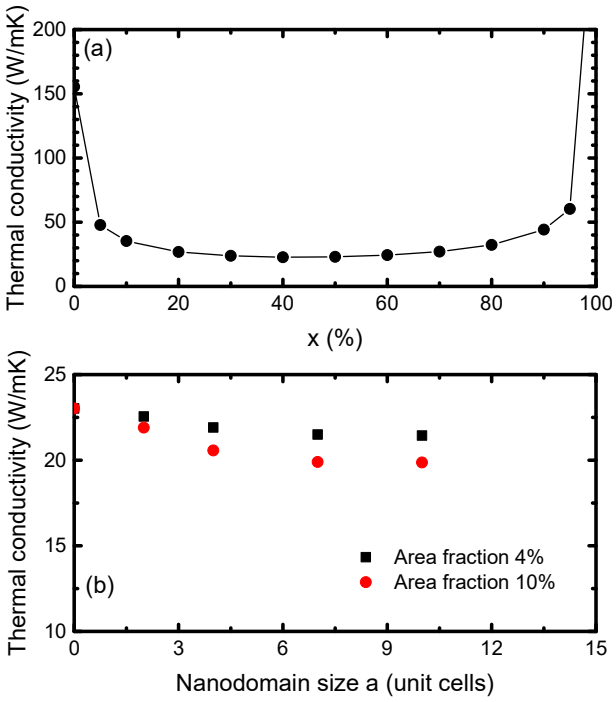

Figure IV.2. (a) Thermal conductivity of $Mo_{1-x}W_xS_2$ at 300K as a function of alloy composition x. (b) Thermal conductivity of $Mo_{1-x}W_xS_2$ alloy embedded with W nanodomains as a function of the size of nanodomains.

By embedding triangular WS_2 nanodomains into alloy, which serve as additional scattering centers for low-frequency phonons, the thermal conductivity of the alloys is further reduced. Figure IV.2(b) shows the dependence of thermal conductivity of $Mo_{0.5}W_{0.5}S_2$ alloy embedded with WS_2 nanodomains as a function of the area fraction and the size of nanodomains. The obtained thermal conductivity plotted as solid symbols, and is found to decrease with the size and area fraction of nanodomains when the area fraction increases from 0 to 10% and the size of nanodomains is changed from 1 to 10 unit cells. Apparently, embedding nanodomains considerably reduces the thermal conductivity below the alloy limit. For example, an additional 16 % reduction is observed when the area fraction of nanodomains f^{ND} is 10% and the side length of each nanodomain a is 10 unit cells. Although the degree of thermal conductivity reduction of $Mo_{1-x}W_xS_2$ alloy due to nanodomains is smaller than some 3-D alloys, where additional factor of 2 to 4 is found when nanoparticles are embedded [49], but it is comparable to nanostructured BiSbTe alloy [48]. In fact, the nanodomain/nanoparticle induced thermal conductivity reduction could be affected by many factors, including the alloy composition, crystal structures and so on. The dimensionality might be another factor that affects the thermal conductivity reduction, which calls for further investigation.

To gain insights about the thermal conductivity reduction when nanodomains are embedded in an alloy matrix, we examine the accumulated thermal conductivity of $Mo_{0.5}W_{0.5}S_2$ alloy and the alloy embedded with nanodomains whose area fraction and side length are 10% and 10 unit cells as a function of phonon frequency, as shown in Fig. IV.3. It is clearly seen that the thermal conductivity difference between the alloy with and without nanodomains is mainly caused by low-frequency phonons. This indicates that the long-wavelength phonons are more effectively scattered by the nanodomains than by the alloy components that are replaced by the nanodomains.

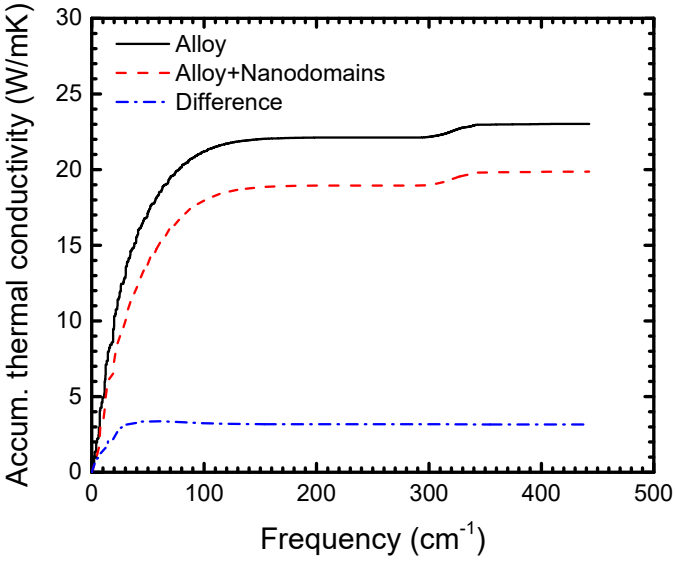

Figure IV.3. The accumulative thermal conductivity of $Mo_{0.5}W_{0.5}S_2$ with and without nanodomains embedded as a function phonon frequency. The thermal conductivity difference is mainly caused by low-frequency phonons.

IV.4 Phonon-nanodomain scattering rates

To understand the scattering mechanisms of long-wavelength/low-frequency phonons in the alloy embedded with nanodomains, we present the calculated phonon-nanodomain scattering rates of longitudinal acoustic phonons of single-layer $Mo_{1-x}W_xS_2$ on a high symmetry line from the Γ point, (0, 0), to the M point, $(0, \pi/a_0\sqrt{3})$, as a function of phonon frequency in the log-log scale, which is shown in Fig. IV.4(a). The scattering rate of a specific mode due to the nanodomains is written as

$$\Gamma_{\mathbf{q}s} = \sum_{\mathbf{q}'s'} W^{\mathrm{ND}}_{\mathbf{q}s,\mathbf{q}'s'} / n^0_{\mathbf{q}s}\left(n^0_{\mathbf{q}s}+1\right), \qquad \text{(IV.6)}.$$

Here the scattering rates are normalized by the area fraction of nanodomains in order to fairly compare the effects of nanodomains with different sizes on phonon scattering. As expected, the

strength of phonon-nanodomain scattering is greatly affected by both the phonon frequency and the size of nanodomains. For low-frequency phonons, whose wavelengths are much larger than the characteristic size of nanodomains, the frequency-dependent scattering rate follows a nice ω^{-3} scaling relation, which is consistent with the characteristics of Rayleigh scattering in 2-D crystals [187]. The scattering rate also increases with the size of nanodomains for these long-wavelength/low-frequency phonons. Figure IV.4(b) shows phonon-nanodomain scattering rates of long-wavelength acoustic phonons with a wavevector of $0.03(0, \pi/a_0\sqrt{3})$ versus the number of W atoms in each nanodomain, *N*, where the scattering rate is found to be proportional to N.

In fact, the phonon scattering rate of the Rayleigh scattering can be easily obtained using the Born approximation, where the **T** matrix in Eq. (IV.3) is replaced by the perturbation matrix **V.** The obtained total scattering rate of a specific mode due to the nanodomains scales as

$$\Gamma_{\mathbf{q}s} \propto \frac{1}{N}\left(N\frac{\Delta M}{M}\right)^2. \quad \text{(IV.7)}$$

From this simple relation between the scattering rate, Γ, and the number of W atoms in each nanodomain, *N*, one can expect that the ratio between the scattering rate due to nanodomains and that due to Mo and W impurities of alloy, which can be regarded as nanodomains with 1 atom, should scale proportionally with N. As a result, the long-wavelength phonons could be more strongly scattered in the alloy embedded with nanodomains than the alloy only.

On the other hand, Fig. IV.4(a) shows that the scattering rate of high-frequency phonons, whose wavevectors are close to the edge of the first Brillouin zone, decreases with the size of nanodomain, which is drastically different from the low-frequency phonons. Figure IV.4(b) shows the phonon scattering rates for the acoustic phonons at (0, 0.97M), which are taken as examples of short-wavelength phonons. The phonon scattering rate clearly follow $\Gamma \propto 1/\sqrt{N}$. This is because it is at the geometric scattering regime [196, 197] where the scattering cross section is limited by

the size of the nanodomain when the wavelength is smaller than the size of nanodomain [196, 198]. Since the scattering rate of the mode $\mathbf{q}s$ is linked to the scattering cross section through $\Gamma_{\mathbf{q}s} = N^{\mathrm{ND}}\sigma_{\mathbf{q}s}v_{\mathbf{q}s}$ in the 2-D systems, where σ is the scattering cross section, v is the phonon group velocity and N^{ND} is the number density of the scatterers, the scattering rate is inversely proportional to the scattering cross section, or equivalently the side length, a, of nanodomains, which scales as $\sqrt{N}$.

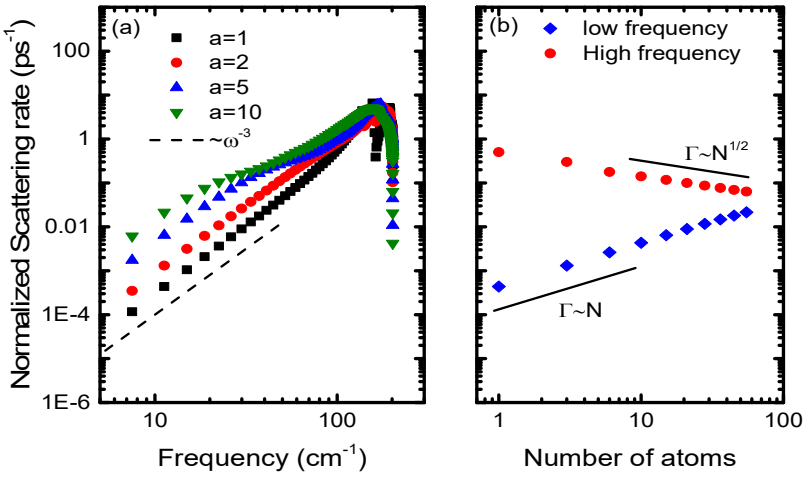

Figure IV.4. (a) The phonon-nanodomain scattering rates of LA phonons from the Γ point to the M point as a function of phonon frequency. (b) The phonon-nanodomain scattering rates of long-wavelength LA phonon at 0.03(0, $\pi/a_0\sqrt{3}$) and short-wavelength LA phonon at 0.97(0, $\pi/a_0\sqrt{3}$). The scattering rates are normalized by the area fraction of the nanodomains.

Because the strengths of phonon scattering for long-wavelength and short-wavelength phonons follow opposite trends with the size of nanodomains, there exists a minimum thermal conductivity with optimal size of nanodomains. Due to the computational limitations, we are not able to directly

evaluate the thermal conductivity of the samples embedded with nanodomains using the Green's function approach when the size of nanodomains is larger than 10 unit cells. However, as seen in Fig. IV.2(b), the optimal size of nanodomains could be around 10 unit cells, where the thermal conductivity of alloy embedded with nanodomains is almost unchanged with the size.

IV.5 Thermal conductivity dependence of alloy composition

Figure IV.5 shows the dependence of thermal conductivity of alloy embedded with nanodomains whose size is 10 unit cells and area fraction is 10% on the composition of alloy matrix. The thermal conductivity value changes non-monotonically with the composition of alloy matrix, just as the alloy without embedding nanodomains. But the minimum thermal conductivity occurs at the composition of $x \approx 20\%$, while that of pure alloy is at $x \approx 50\%$. This means that the pure alloy with the minimum thermal conductivity is not necessarily the best matrix for such nanocomposites to achieve lowest thermal conductivity. For example, the thermal conductivity of alloy embedded with 10-unit-cell-large WS_2 nanodomains at 10% area fraction decreases from 19.8 W/mK to 16.9 W/mK when the composition of W changes from 50% to 20%.

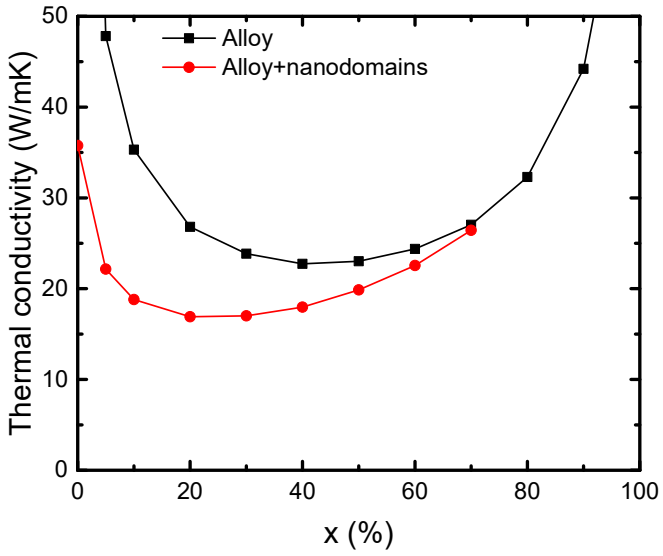

Figure IV.5. Thermal conductivity of $Mo_{1-x}W_xS_2$ alloy embedded with 10-unit-cell-large WS_2 nanodomains at 10% area fraction at 300 K as a function alloy composition x.

To understand the lower thermal conductivity in $Mo_{0.8}W_{0.2}S_2$-based nanocomposites than that in $Mo_{0.5}W_{0.5}S_2$-based nanocomposites with the same WS_2 nanodomains, we compare the phonon-alloy scattering rates and the phonon-nanodomain scattering rates in different alloy compositions, as shown in Fig. IV.6(a) and (b), respectively. As expected, it is seen from Fig. IV.6(a) that the phonon-alloy scattering rates in $Mo_{0.8}W_{0.2}S_2$-based nanocomposite become smaller than those in $Mo_{0.5}W_{0.5}S_2$-based one due to less disorder in $Mo_{0.8}W_{0.2}S_2$ alloy-based nanocomposites. However, Fig. IV.6(b) shows that the scattering rates due to nanodomains become almost doubled in $Mo_{0.8}W_{0.2}S_2$ alloy-based nanocomposites for low-frequency phonons, but the scattering rates are almost unchanged for high-frequency phonons. This is expected because the scattering rates for the low-frequency phonons are mainly determined by the total mass contrast, $(N\Delta M/M)$, between the nanodomain and the averaged mass of alloy matrix, as indicated by the Born approximation,

Eq. (6), while for high-frequency phonons, the scattering rates are governed by the geometrical size of nanodomains, which is almost unchanged with respect to the alloy composition. Since most of heat is conducted by low-frequency phonons in the alloy and nanocomposites, as indicated from Fig. IV.4, the enhanced scattering for low-frequency phonons due to nanodomains can effectively reduce the total conductivity of alloys embedded with nanodomain.

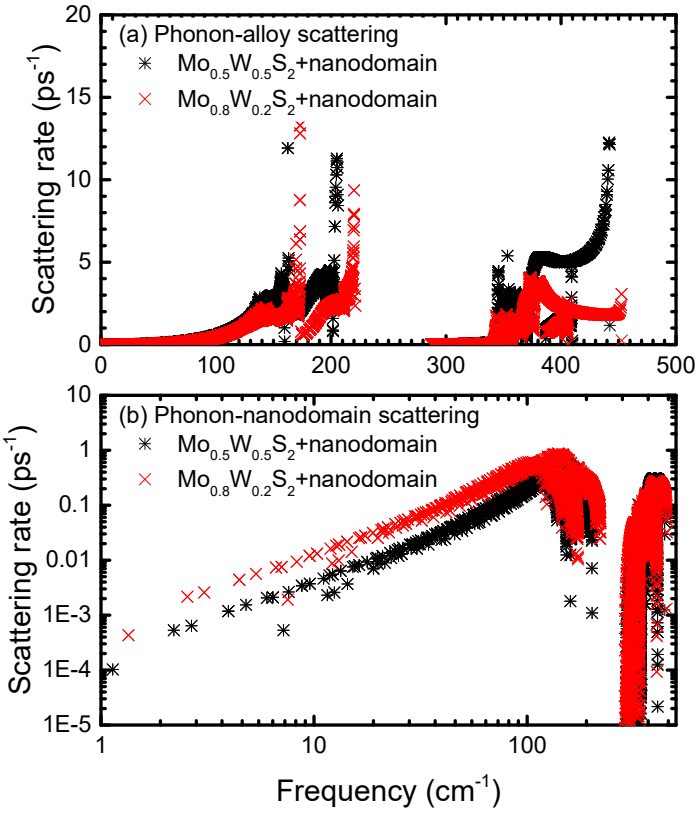

Figure IV.6. (a) Phonon-alloy scattering rates as a function of phonon frequency. (b) Phonon-nanodomain scattering rates as a function of phonon frequency.

IV.6 Summary of this chapter

In this work, we have demonstrated a possible way to significantly reduce the thermal conductivity of single-layer MoS_2 through alloying and nanodomain embedding.

There are indeed plenty of rooms to further tune the thermal conductivity. In current study, all nanodomains are of the same size, but it is expected that embedding nanodomains with different sizes could help to reduce further the thermal conductivity. Another possibility is to either introduce $MoSe_2$ and/or WSe_2 components into the $Mo_{1-x}W_xS_2$ alloy or use them as nanodomains. Because the mass ratio between Se and S atoms is larger than that between W and Mo atoms and the force field difference between the MoS_2 and $MoSe_2$ is also larger than that between MoS_2 and WS_2 [156]. alloying and introducing nanodomains on chalcogen atoms can enhance the phonon scattering in the 2-D alloy compared with the case that only the metal atoms are mixed. Once the monolayers after nanostructuring are obtained, one might be able to stack them together to form a layered material with very low thermal conductivity. Recent study showed that by intercalation layered materials with organic components, the thermoelectric properties can be significantly improved for layered materials mainly due to the lower thermal conductivity [173]. It might be possible to further optimize the obtained layered material through intercalation. Despite these possible approaches to further reduce the thermal conductivity of 2-D materials, it should be noticed that the parameters that determine the thermoelectric performance of the material are usually highly correlated. In order to optimize the thermoelectric performance of the nanostructured 2-D materials, more detailed analysis should be conducted, especially on the electronic properties.

In summary, we study the phonon scattering mechanisms and thermal conductivity in $Mo_{1-x}W_xS_2$ alloy embedded with triangular WS_2 nanodomains using first-principles-based PBTE calculations. The phonon scattering rates due to alloy and nanodomain are evaluated through the Green's function approach. The thermal conductivity of $Mo_{1-x}W_xS_2$ is found to be significant lower than MoS_2. For example, the thermal conductivity of $Mo_{0.5}W_{0.5}S_2$ is only 16% of MoS_2 when the

sample size is 10 μm. By embedding WS_2 nanodomains into $Mo_{0.8}W_{0.2}S_2$, the obtained thermal conductivity of alloy can be 10 times smaller than that of MoS_2 due to both the strong alloy scattering for high-frequency phonons and nanodomain scattering for low-frequency phonons. If the electronic properties of MoS_2 can be retained after introducing nanodomains, $Mo_{1-x}W_xS_2$ alloy embedded with WS_2 could be a good thermoelectric material, which is worth further investigation.

CHAPTER V PHONON TRANSMISSION ACROSS MATERIAL INTERFACES: A FRIST-PRINCIPLES-BASED ATOMISTIC GREEN'S FUNCTION STUDY

V.1 Introduction

Understanding phonon transport in nanostructured materials and devices is of great importance in many technological fields, from thermal management in electronics and photonics [118, 199] to thermoelectric energy conversion [51, 52], to thermal insulation and thermal protection system [200]. Interfaces play a critical role in determining phonon dynamics and thermal conduction in nanostructures. The detailed information of how a phonon quanta with specific energy and momentum is scattered by an interface is essential for designing nanostructures with desirable thermal performance using mesoscopic modeling tools, such as phonon Boltzmann transport equation (BTE) based method and Monte Carlo simulations [21, 23, 201, 202].

In recent years, the atomistic Green's function (AGF) approach has been shown to be an efficient method to study frequency-dependent phonon transport across interfaces of dissimilar materials [27, 203]. The phonon transmission is highly dependent on the details of atomic configuration and interatomic interaction around the interface [204, 205]. AGF approach has been applied to study a wide range of interfaces, including sharp (smooth) interfaces [28, 79, 206], rough interfaces [205], interfaces with vacancy defects and alloyed interfaces [204]. Often the empirical potentials are used in AGF calculations to describe the interatomic interactions [79, 204-207]. The interatomic force constants from the first-principles calculations have also been

integrated with AGF method for studying interfaces of materials, especially when the empirical potentials are not readily available [28, 208, 209].

However, it would be quite challenging to extract the interatomic force constants of realistic material interfaces from the first-principles calculations. Comparing to the first-principles prediction of thermal conductivity of bulk crystals [8, 15-17, 164], the lattice near an interface of two dissimilar materials is likely to be distorted due to the lattice mismatch and the difference in the force field experienced by the atoms in the interfacial region. A large supercell would be required for the first-principles calculations to capture the essential characteristics of the lattice-mismatched interface, which leads to severe numerical challenges. The mass approximation (MA) [28, 50] that was employed to calculate the thermal conductivity of alloys [16, 18, 19] has thus been used to extract interatomic force constants of the interfacial region from the first-principles. Under the MA, the differences in the lattice constants and the force fields between the two dissimilar materials are ignored and only the difference in atomic mass is taken into account. It was recently pointed out that the MA tends to overestimate the thermal conductivity due to the neglect of the local force-field difference [210]. Other studies showed that the MA under-predicts the contribution of high-frequency phonons, which leads to a lower thermal conductivity [211]. It is unclear whether MA is a reasonable approximation when integrated with the AGF approach to calculate the phonon transmission across the interfaces of dissimilar materials where there exist the differences in both lattice constants and force fields.

In this paper, we propose an integrated first-principles-based AGF approach using higher-order force constant model (HOFCM) to compute phonon transmission across interfaces of dissimilar materials. By considering the lattice distortion and the species-dependent local force field, the accuracy of the interatomic force constants extracted is improved compared with that from the MA,

while the required computational resources are significantly less severe than directly extracting force constants from the standard first-principles calculations. As an example, we present the detailed studies of frequency-dependent phonon transmission across $Mg_2Si/Mg_2Si_{1-x}Sn_x$ interface, which is promising thermoelectric material system for intermediate temperature range energy conversion applications [212-214]. We systematically study how the lattice mismatch-induced local force field influences phonon transmission across the interfaces between dissimilar materials, which are inevitably ignored in the MA. This study could provide guidance for designing nanostructured materials with tunable thermal conductivity.

V.2 Modeling approaches

The AGF approach needs the harmonic interatomic force constants as inputs for the dynamical matrix to calculate phonon transmission. The conventional standard method that is used to extract the harmonic interatomic force constants of bulk crystals from the first-principles calculations is infeasible for interfaces where the lattice at the interfacial region is likely distorted due to the lattice mismatch and the local force fields. In this work, we employ the HOFCM, which originates from the MA but considers the local force difference due to the different species, to efficiently calculate the harmonic force constants of the interfacial regions, and then integrate the obtained force constants from the first-principles calculations with the AGF approach. In Sec. II A, we discuss the methods to extract the harmonic constants, including the standard direct methods from the first-principles, the MA, and the HOFCM. A brief summary of the AGF method is given in Sec. II B where the details can be found in literature including the author's prior work [79, 204]. Figure V.1 summarizes the simulation procedures of the first-principles-based atomistic Green's function

approach, including both MA- and the HOFCM-based approaches. The computational details are given in Sec. II C for $Mg_2Si/Mg_2Si_{1-x}Sn_x$ interface.

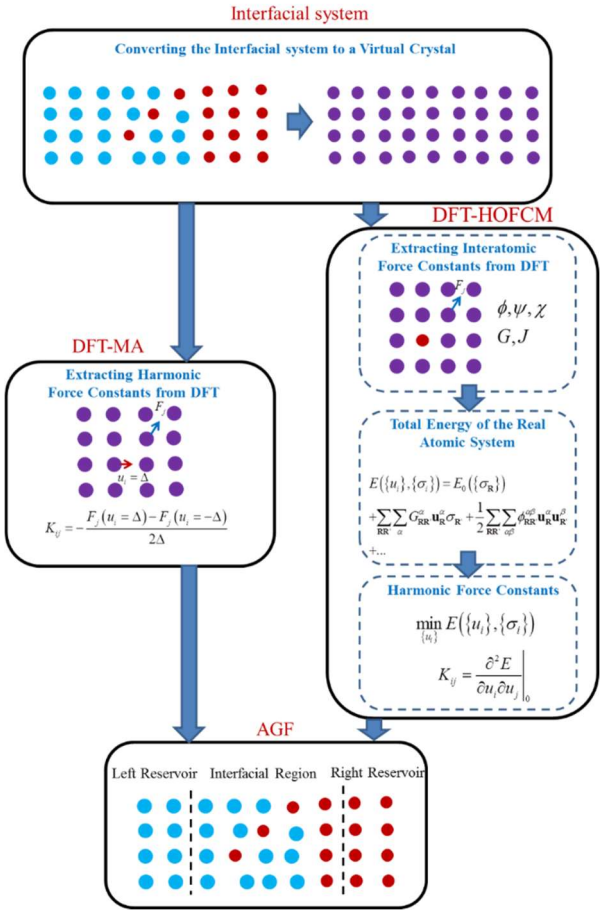

Figure V.1. Numerical simulation procedure of the integrated DFT-AGF approaches: MA-AGF and HOFCM-AGF. In both approaches, an interfacial system is first converted to an effective virtual crystal. In MA, the harmonic force constants are computed from DFT calculations of the virtual crystal, and then directly used as the inputs for AGF calculations. In HOFCM, the interatomic force constants with respect to both the atom displacements and atom species are extracted from DFT calculations. Then a force-field using these interatomic force constants are constructed, which is used to determine the equilibrium configuration of the interfacial system and the corresponding harmonic force constants that are used in AGF calculations.

V.2.1 Interatomic force constants from the first-principles calculations

The harmonic interatomic force constants K that are used in AGF approach are the second-derivatives of the total energy of a system E with respect to the atom displacements

$$K_{\mathbf{RR'}}^{\alpha\beta} = \frac{\partial^2 E}{\partial u_{\mathbf{R}}^{\alpha} \partial u_{\mathbf{R'}}^{\beta}}, \tag{V.1}$$

where $u_{\mathbf{R}}^{\alpha}$ denotes the displacement of an atom along the α direction whose equilibrium position is $\mathbf{R}$. In principle, one could compute the harmonic force constants of a given atomic system from the first-principles by monitoring the response of the total energy of the whole system under small perturbations, such as the small-displacement method [95, 215, 216] or the perturbation approach [217]. For a bulk crystal with a small primitive unit cell, the calculations for harmonic force constants using both methods are computationally affordable. Take the small-displacement method as an example, in which the force constants are calculated in a supercell. A series of first-principles calculations for total energy are performed when one atom in the primitive unit cell is moved with a small distance Δ in the order of 0.01 Å along a Cartesian direction. When all atoms in the primitive unit cell are displaced, the harmonic force constants are then extracted through either the finite difference scheme [95, 215] or fitting the displacement-force relation [216]. Although only the harmonic force constants involving the atoms in the primitive cell are obtained directly, other harmonic force constants between any two atoms in the crystal are extracted simultaneously by taking advantage of the periodicity of the crystal.

However, when dealing with interfaces, such conventional methods would become computationally overwhelming due to the loss of the periodicity of the crystal. The force constants between every atom pair need to be determined independently at least along the direction perpendicular to an interface. In addition, the distortion of lattice due to the mismatch of lattice

constants could extend to several unit cells away from the interface, while the species mixing near the interface might span a few nanometers as well. As a result, very large supercells are needed for extracting the force constants. For example, if we use a supercell with a cross-sectional area of 2×2 conventional unit cells to model an Mg_2Si/Mg_2Sn interfacial region with species mixing that spans 10 unit cells, we have to perform a series of first-principles calculations to generate the displacement-force relation. In each calculation, one atom is displaced from their equilibrium position and the forces on other atoms are recorded. The total number of these first-principles calculations would be at least as large as $40\times 12\times 3\times 2 = 2880$ (40 conventional unit cells, 12 atoms per unit cell for Mg_2Si/Mg_2Sn system, 3 degrees of freedom, and 2 directions along a Cartesian direction). Furthermore, the calculations have to be repeated when the atomic configuration is slightly changed in order to obtain the harmonic force constants of the new system. For convenience, we refer the method just discussed above that the entire interfacial region is modeled to extract harmonic force constants as the direct method.

Due to the computational challenge in the direct method, the mass approximation that was employed to calculate the thermal conductivity of alloys is adopted recently, which models the interfacial region made up of two dissimilar materials to an imaginary (virtual) perfect homogenous bulk crystal so that the force constants can be easily extracted in first-principles calculations with the same procedures used for bulk crystals instead of modeling the entire interfacial region. In the density-functional-theory-based (DFT-based) approach, the type of atom is distinguished by its pseudopotential. A widely-used treatment of the MA in the DFT-based approach is to calculate the force constants in a virtual crystal [218], where the two types of atoms in the simulation are replaced by virtual atoms, whose pseudopotential is the percentage weighted pseudopotentials of the two types of elements through

$$V_{\sigma} = \left[\left(1+\sigma\right)/2\right]V_{\text{elem1}}(\mathbf{r}) + \left[\left(1-\sigma\right)/2\right]V_{\text{elem2}}(\mathbf{r}), \quad \text{(V.2)}$$

where $V_{\text{elem1}}(\mathbf{r})$ and $V_{\text{elem2}}(\mathbf{r})$ are the pseudopotentials for element 1 and element 2, and σ represents the likeliness of the virtual atom to be element 1 or 2. σ=1 and -1 represents element 1 and 2, respectively. When σ=0, the atom is of the averaged properties of element 1 and element 2. σ=0 is the most natural choice for the virtual atoms for an interface constructed by connecting two pure materials with element 1 and element 2.

Since the interfacial region can be treated as the homogenous crystal under the MA, the force field throughout the interfacial region is identical. As a result, the non-uniformity of the strain field resulted from the lattice mismatch in the interfacial region becomes absent. In addition, the local force fields within the bulk phases are no longer the actual ones, which should be determined from the direct method with the species' own pseudopotentials, but shifted to an averaged one. In other words, the vibrational properties of the reservoirs (semi-infinite crystal) could be inaccurate.

To overcome the limitations of the MA, we employ the HOFCM proposed by de Gironcoli [219] to extract the harmonic force constants for the interfacial region. The HOFCM was originally proposed to better describe the vibrational properties of Si/Ge systems beyond single crystals, including superlattices [220] and homogeneous $Si_{1-x}Ge_x$ alloys [221]. Taking advantage of the HOFCM, the first-principles-based calculations can reproduce the Raman spectra of Si_xGe_{1-x} alloy very accurately [219]. In this work, we first approximate an interfacial region of large dimension that contains two species as a virtual crystal. Comparing the realistic interfacial region with the virtual crystal, the difference of their total energies originates from two aspects: 1) the atoms in a real interfacial region are not uniformly distributed as in a virtual crystal but are of small displacements $\mathbf{u}_{\mathbf{R}}$ from their virtual crystal counterparts because the lattice is likely to be distorted near the interface. 2) The type of the atom $\sigma_{\mathbf{R}}$ and the corresponding force field in the real system

is different from the virtual atom. Both of them make the harmonic force constants of the real interface deviated from the virtual crystal. The higher-order force constants with respect to $\mathbf{u}_\mathbf{R}$ and $\sigma_\mathbf{R}$ is then used to refine the total energy of the virtual crystal so that the difference between the real interfacial system and the virtual crystal is eliminated.

The difference between the total energy of the real interfacial region and that under the virtual crystal approximation is calculated using the Taylor's expansion of the total energy of the reference virtual crystal with respect to $\{\mathbf{u}_\mathbf{R}\}$ and $\{\sigma_\mathbf{R}\}$ as

$$\begin{aligned} E\left(\{\mathbf{u}_\mathbf{R}\},\{\sigma_\mathbf{R}\}\right) &= E_{\mathrm{VC}} + \sum_\mathbf{R}\left(\left.\frac{\partial E}{\partial \sigma_\mathbf{R}}\right|_{\mathrm{VC}} \sigma_\mathbf{R} + \left.\frac{\partial E}{\partial \mathbf{u}_\mathbf{R}}\right|_{\mathrm{VC}} \cdot \mathbf{u}_\mathbf{R}\right)\cdots \\ &= E_{\mathrm{VC}} + \left(\sum_\mathbf{R}\left.\frac{\partial E}{\partial \sigma_\mathbf{R}}\right|_{\mathrm{VC}} \sigma_\mathbf{R} + \sum_{\mathbf{RR'}}\left.\frac{\partial^2 E}{\partial \sigma_\mathbf{R}\partial \sigma_{\mathbf{R'}}}\right|_{\mathrm{VC}} \sigma_\mathbf{R}\sigma_{\mathbf{R'}} + \ldots\right) \\ &+ \left(\sum_\mathbf{R}\left.\frac{\partial E}{\partial \mathbf{u}_\mathbf{R}}\right|_{\mathrm{VC}} \cdot \mathbf{u}_\mathbf{R} + \sum_{\mathbf{RR'}}\left.\frac{\partial^2 E}{\partial \mathbf{u}_\mathbf{R}\partial \mathbf{u}_{\mathbf{R'}}}\right|_{\mathrm{VC}} \cdot \mathbf{u}_\mathbf{R}\cdot\mathbf{u}_{\mathbf{R'}} + \sum_{\mathbf{RR'}}\left.\frac{\partial^2 E}{\partial \mathbf{u}_\mathbf{R}\partial \sigma_{\mathbf{R'}}}\right|_{\mathrm{VC}} \cdot \mathbf{u}_\mathbf{R}\cdot\sigma_{\mathbf{R'}} + \ldots\right) \\ &= E_0 + \left(\sum_\mathbf{R}\left.\frac{\partial E}{\partial \mathbf{u}_\mathbf{R}}\right|_{\mathrm{VC}} \cdot \mathbf{u}_\mathbf{R} + \sum_{\mathbf{RR'}}\left.\frac{\partial^2 E}{\partial \mathbf{u}_\mathbf{R}\partial \mathbf{u}_{\mathbf{R'}}}\right|_{\mathrm{VC}} \cdot \mathbf{u}_\mathbf{R}\cdot\mathbf{u}_{\mathbf{R'}} + \sum_{\mathbf{RR'}}\left.\frac{\partial^2 E}{\partial \mathbf{u}_\mathbf{R}\partial \sigma_{\mathbf{R'}}}\right|_{\mathrm{VC}} \cdot \mathbf{u}_\mathbf{R}\cdot\sigma_{\mathbf{R'}} + \ldots\right) \end{aligned} \quad \text{(V.3)},$$

where E_{VC} is the total energy of the virtual crystal. Because the second and the third terms in the second line of Eq. (V.3) involve only the atom type $\{\sigma_\mathbf{R}\}$, they do not influence the forces on the atoms but just shift the total energy. We can simply combine these terms with E_{VC} and note as energy E_0, which is the total energy of the system taking into account atom type difference but with zero displacement. When the atom types are prefixed and the total energy is expanded up to the third-order terms with respect to the atom displacements, the expression can be further written as:

$$E\left(\{\mathbf{u}_{\mathbf{R}}\},\{\sigma_{\mathbf{R}}\}\right)=E_0+\sum_{\mathbf{RR'}}\sum_{\alpha}G^{\alpha}_{\mathbf{RR'}}\mathbf{u}^{\alpha}_{\mathbf{R}}\sigma_{\mathbf{R'}}+\frac{1}{2}\sum_{\mathbf{RR'}}\sum_{\alpha\beta}\phi^{\alpha\beta}_{\mathbf{RR'}}\mathbf{u}^{\alpha}_{\mathbf{R}}\mathbf{u}^{\beta}_{\mathbf{R'}}+\frac{1}{2}\sum_{\mathbf{RR'R''}}\sum_{\alpha}J^{\alpha}_{\mathbf{RR'R''}}\mathbf{u}^{\alpha}_{\mathbf{R}}\sigma_{\mathbf{R'}}\sigma_{\mathbf{R''}}$$
$$+\frac{1}{2}\sum_{\mathbf{RR'R''}}\sum_{\alpha\beta}\chi^{\alpha\beta}_{\mathbf{RR'R''}}\mathbf{u}^{\alpha}_{\mathbf{R}}\mathbf{u}^{\beta}_{\mathbf{R'}}\sigma_{\mathbf{R''}}+\frac{1}{6}\sum_{\mathbf{RR'R''}}\sum_{\alpha\beta\gamma}\psi^{\alpha\beta\gamma}_{\mathbf{RR'R''}}\mathbf{u}^{\alpha}_{\mathbf{R}}\mathbf{u}^{\beta}_{\mathbf{R'}}\mathbf{u}^{\gamma}_{\mathbf{R''}} \tag{V.4}$$

where the coefficients ϕ and ψ are the derivatives of the total energy of the virtual crystal with respect to the displacement of atoms, which are the second-order harmonic and the third-order anharmonic force constants of the virtual crystal, and the coefficients G , J and χ are the derivatives with respect to both atom displacements and atom types. Once these coefficients in Eq. (V.4) are determined, the difference of the total energy from a real interfacial system to that under the virtual crystal approximation can be greatly compensated for by using these terms.

To extract these coefficients in Eq. (V.4), we adopt the small-displacement method [216]. According to Eq. (V.4), the force on each atom is

$$F^{\alpha}_{\mathbf{R}}=-\frac{\partial E}{\partial \mathbf{u}^{\alpha}_{\mathbf{R}}}=-\sum_{\mathbf{R'}}G^{\alpha}_{\mathbf{RR'}}\sigma_{\mathbf{R'}}-\sum_{\mathbf{R'}}\sum_{\beta}\phi^{\alpha\beta}_{\mathbf{RR'}}\mathbf{u}^{\beta}_{\mathbf{R'}}-\frac{1}{2}\sum_{\mathbf{R'R''}}J^{\alpha}_{\mathbf{R'R''}}\sigma_{\mathbf{R'}}\sigma_{\mathbf{R''}}$$
$$-\sum_{\mathbf{R'R''}}\sum_{\beta}\chi^{\alpha\beta}_{\mathbf{RR'R''}}\mathbf{u}^{\beta}_{\mathbf{R'}}\sigma_{\mathbf{R''}}-\frac{1}{2}\sum_{\mathbf{R'R''}}\sum_{\beta\gamma}\psi^{\alpha\beta\gamma}_{\mathbf{RR'R''}}\mathbf{u}^{\beta}_{\mathbf{R'}}\mathbf{u}^{\gamma}_{\mathbf{R''}} \tag{V.5}$$

If the atoms in virtual crystal are displaced by a small distance away from their equilibrium positions or the types of atoms are altered, the force will not be zero anymore and could be accurately predicted in first-principles calculations through the Hellmann-Feynman theorem [222]. By fitting these displacement-type-force relations, the coefficients could be obtained.

We first determine the independent interatomic force constants based on the permutation symmetry of higher-order derivatives and the space group symmetry of the crystal [216]. Then one or two atoms in the virtual crystal are displaced from their equilibrium positions, and the types for all atoms are kept as $\{\sigma_{\mathbf{R}}=0\}$. Through first-principles calculations, the forces on all atoms in the

virtual crystal are computed. Putting the obtained forces, the atomic displacement and $\{\sigma_{\mathbf{R}}=0\}$ into Eq. (V.5), we get a linear equation set with respect to ϕ and ψ as unknown variables. Since the data set is usually larger than the number of independent force constants, the coefficients ϕ and ψ cannot be solved exactly but are extracted from the linear fitting. To obtain physically correct interatomic force constants, the translational and rotational invariances [216, 219] of these interatomic force constants are further considered in fitting procedures and serve as constraints in the fitting procedures. We use the singular value decomposition (SVD) technique to convert the constrained linear least-squares problem to an unconstrained one. The details of the invariances of interatomic force constants and how to impose the invariances are discussed in Appendix A.5. By solving the unconstrained equation sets, the coefficients ϕ and ψ are extracted.

Since the coefficients G, J and χ are related to both the atomic displacement and the atom types, we need to not only displace the atoms but also change the type of one or two atoms from 0 to ± 1 so that the terms on G, J and χ could take effects on the forces on the atoms in the system. Plugging the atomic displacements, the atom type $\{\sigma_{\mathbf{R}}\}$ and the values of the coefficients ϕ and ψ, which have been obtained before, Eq. (V.5) becomes the linear equation set with respect to G, J and χ. Similar to the coefficients ϕ and ψ, the physically correct coefficients G, J and χ also need to satisfy their translational and rotational invariance relations [219], which can be found in Appendix A.5. With the SVD techniques, the coefficients G, J and χ are solved from the linear equation set with the same least-squares method as we used to extract the coefficients ϕ, ψ.

In AGF calculations, the atoms in the system need to be in the equilibrium positions. To determine the equilibrium configuration of the system, the analytical expression Eq. (V.4) are used

to determine the equilibrium configuration of the system by minimizing the total energy of the system. The corresponding harmonic interatomic force constants K used in AGF simulations are then given by taking the derivative of Eq. (V.4):

$$K_{\mathbf{RR'}}^{\alpha\beta} = \phi_{\mathbf{RR'}}^{\alpha\beta} + \sum_{\mathbf{R''}} \chi_{\mathbf{RR'R''}}^{\alpha\beta} \sigma_{\mathbf{R''}} + \sum_{\mathbf{R''}} \sum_{\gamma} \psi_{\mathbf{RR'R''}}^{\alpha\beta\gamma} \mathbf{u}_{\mathbf{R''}}^{\gamma} \tag{V.6}$$

There are a few advantages of using HOFCM for extracting the harmonic interatomic force constants compared with the direct method: 1) It avoids using a large supercell to model the interfacial region. Since all coefficients in Eq. (V.4) are the derivatives of the total energy of the virtual crystal, these coefficients can be extracted using a relatively small supercell just as that used to calculate the harmonic force constants in a bulk crystal with periodicity. 2) When the set of coefficients is obtained, it can be applied to systems with different atomic configurations. In contrast, in the direct method the force constants need to be recalculated every time when the configurations of interfacial regions are changed. 3) Using HOFCM, the system can be relaxed by minimizing the analytical expression of total energy, while system relaxation in DFT calculation requires a series of time-consuming self-consistent field calculations.

V.2.2 AGF approach for phonon transmission

A typical AGF simulation system for phonon transmission consists of three regions, one interfacial region and two semi-infinite reservoirs made up of bulk crystal 1 and 2. Phonon transmission across the interfacial region is calculated using the Green's function, which gives the response of the system under small perturbation. Under harmonic approximation, the Green's function $\mathbf{G}_{d,d}$ corresponding to the interfacial region can be calculated as [203]

$$\mathbf{G}_{d,d} = \left[\omega^2\mathbf{I} - \mathbf{H}_{d,d} - \mathbf{\Sigma}_1 - \mathbf{\Sigma}_2\right]^{-1}, \tag{V.7}$$

where ω is the phonon frequency; $\mathbf{H}_{d,d}$ represents the dynamical matrix of the whole interfacial region, $\mathbf{\Sigma}_1$ and $\mathbf{\Sigma}_2$ is the self-energy matrices of the left and right reservoirs, which are calculated from the dynamical matrices of reservoirs.[206] The elements in the dynamical matrices are written as

$$H_{ij} = \frac{1}{\sqrt{m_{\mathbf{R}} m_{\mathbf{R}'}}} K_{\mathbf{R}\mathbf{R}'}^{\alpha\beta}, \tag{V.8}$$

where *i* (*j*) stands for the *i*th (*j*th) degree of freedom in the system, or the α (β) direction of the atom at $\mathbf{R}$ ($\mathbf{R}'$); $m_{\mathbf{R}}$ is the mass of the atom at $\mathbf{R}$. With the Green's function, the total phonon transmission across the interfacial region is calculated as,

$$\Xi(\omega) = Tr[\mathbf{\Gamma}_1 \mathbf{G}_{d,d} \mathbf{\Gamma}_2 \mathbf{G}_{d,d}^{+}], \tag{V.9}$$

where $\mathbf{\Gamma}_1 = i(\mathbf{\Sigma}_1 - \mathbf{\Sigma}_1^{+})$, $\mathbf{\Gamma}_2 = i(\mathbf{\Sigma}_2 - \mathbf{\Sigma}_2^{+})$ and " + " denotes the conjugate transpose of the matrix. We use transmission per phonon $\xi(\omega)$ to present our results, which is related to the total phonon transmission through [223]

$$\Xi(\omega) = \xi(\omega) M(\omega), \tag{V.10}$$

where $M(\omega)$ is the total number of phonon modes at frequency ω from materials 1. More details can be found in Ref. [27, 204, 206].

The interfacial thermal conductance can then be calculated with the Landauer formalism using the total phonon transmission [224]:

$$G_0 = \frac{1}{2\pi A} \int_0^{\infty} \hbar\omega \frac{\partial f(\omega, T)}{\partial T} \Xi(\omega) d\omega, \tag{V.11}$$

where A is the cross-sectional area perpendicular to the heat flow direction, $f(\omega,T)$ is the phonon occupation number at the temperature T. It has been recognized that Eq. (10) gives a finite conductance for phonon transport across a non-existing interface within a bulk material, which is different from the conventional definition of interfacial conductance [225, 226]. To eliminate the finite conductance for a non-existing interface, we adopt the revised expression used by Tian *et al*. [28] to calculate the thermal conductance,

$$G = \frac{G_0}{1-\left(G_0/G_1 + G_0/G_2\right)/2}, \tag{V.12}$$

where G_1 and G_2 are the thermal conductance of pure material 1 and pure material 2 calculated from Eq. (V.4).

At low temperature, long-wavelength phonons dominate the interfacial thermal resistance across a sharp interface. The interfacial thermal conductance calculated from atomistic Green's function approach is found great agreement with the acoustic mismatch model and found great agreement [206].

It is noted that anharmonicity is not included in the present AGF approach, but it might affect both the phonon transmission and the interfacial thermal conductance at high temperature. Anharmonicity can enhance the interfacial thermal conductance since the inelastic scatterings could convert some phonon modes to the modes that are easily travel across the interface [24]. However, there is no simple approach at present to quantitatively estimate the effects of anharmonicity on phonon transport across specific interfaces, which might worth further investigation.

V.2.3 Implementation for $Mg_2Si/Mg_2Si_xSn_{1-x}$ interface

To illustrate the feasibility of our proposed first-principles-based AGF approach with HOFCM, we implemented the calculation for $Mg_2Si/Mg_2Si_xSn_{1-x}$ thermoelectric material system. Mg_2Si/Mg_2Sn-based materials have recently been studied intensively as promising middle temperature-range (400-800 K) thermoelectric materials [213, 214, 227] due to their reasonably high thermoelectric figure of merit, ZT ~1.1 at 700 K, as well as the abundance of the constituent elements and their nontoxicity. Recent work has suggested that the thermoelectric performance of Mg_2Si-based materials could be further enhanced through nanostructuring, where interface scattering can significantly reduce the phononic thermal conductivity [16]. The understanding of phonon transmission and interfacial thermal conductance across $Mg_2Si/Mg_2Si_xSn_{1-x}$ interface would thus greatly benefit the design of high efficiency Mg_2Si-based thermoelectric materials with low thermal conductivity.

Mg_2Si and Mg_2Sn have cubic anti-fluorite (Fm-3m) structures [195]: Si and Sn atoms sit in the FCC sites while Mg atoms occupy the tetrahedral holes. The similarities and differences between Mg_2Si and Mg_2Sn are attributed to the nature of Si and Sn elements that sit in the same column of the periodic table. To apply the HOFCM, the Si and Sn atoms are replaced by a virtual element, whose pseudopotential is generated by averaging the pseudopotentials of Si and Sn elements according to Eq. (V.2). The generation of the pseudopotential of the virtual element has been implemented in plane wave package QUANTUM ESPRESSO [97]. Using the same package, DFT-based first-principles calculations are performed to generate the displacement-type-force relations, which are used to extract the interatomic force constants. Local density approximation (LDA) of Perdew and Zunger [228] with a cutoff energy of 40 Ry is used for the plane-wave expansion. Considering that the decay of the third-order interatomic force constants (J, ψ, χ) is faster than that of the second-order ones (G, ϕ) as the displacement distance between atoms is

increased, we choose a smaller interaction cutoff for the calculation of the third-order interatomic force constants ($0.866a$) than that for the second-order ones ($1.5a$), where a is the lattice constant. The choice of the cutoff for the third-order force constants is validated by the recent thermal conductivity calculations on Mg_2Si and Mg_2Sn based on Peierls-Boltzmann transport equation (PBTE) theory with interatomic force constants from DFT as inputs, where the same cutoff was applied [16]. A supercell made up of $3\times3\times3$ conventional unit cells with a $4\times4\times4$ Monkhorst-Pack mesh is employed to generate the displacement-type-force data needed for second-order force constants, where one atom is displaced or changed, while a smaller $2\times2\times2$ supercell with a denser $6\times6\times6$ Monkhorst-Pack mesh is used for the third-order force constants. All the coefficients that are needed in the HOFCM are extracted through the DFT calculations using the procedures discussed in section II.A. All the simulations are conducted in the virtual crystal with lattice constant, $a_0=\left(a_0^{Mg_2Si}+a_0^{Mg_2Sn}\right)/2$, where $a_0^{Mg_2Si}$ and $a_0^{Mg_2Sn}$ are the lattice constants of Mg_2Si and Mg_2Sn, respectively.

After the interatomic force constants are determined, the atomic system for the AGF simulation system is constructed and then the position of each atom is optimized until the force on each atom becomes zero. The optimization is performed using the fast inertial relaxation engine (FIRE) algorithm [229], which is a molecular-dynamics-based method to find the minimum energy of an atomic system. The atomic positions are updated according to the forces that exerting on the atoms. The time steps and the atomic velocities are adjusted based on the forces and the velocities of the atoms so that the FIRE algorithm can efficiently relax the interfacial systems. The corresponding harmonic force constants K of a given system in equilibrium are then calculated using Eq. (V.6).

It is worthwhile to note that the harmonic force constants calculated are the zero-temperature values. When the temperature is higher than 0 K, the harmonic force constants could be slightly

changed due to thermal expansion, which could lead to some inaccuracy. According to the previous work reported by Li et al, [16] the difference between the calculated thermal conductivities and the measured ones at 300 K is only within 6%, where the thermal conductivities of Mg_2Si, Mg_2Sn and their alloy were calculated using the force constants at 0 K. The difference becomes larger to be about 20% for Mg_2Si at 600 K. However, considering the relatively scattered values of the measured thermal conductivity of Mg_2Si at high temperature, this difference might not be purely due to using the extracted force constants at 0K for high temperatures. We expect the force constants extracted from 0 K could provide a reasonable description of the lattice vibration properties of Mg_2Si, Mg_2Sn and their alloy from 0 K to 600 K. However, as mentioned earlier, quantitative estimate on the effect of anharmonicity on the phonon transmission has not been achieved and is worthwhile for further investigation.

In AGF simulations, when dealing with large system with thousands of atoms, large-size matrix operation is computationally costly. We employ a recursive AGF approach to efficiently calculate phonon transmission across the interfacial region, as done in our previous work [79, 204].

To test the accuracy of the harmonic force constants from the HOFCM, the phonon dispersions of a few typical Mg_2Si/Mg_2Sn structures are computed and compared with direct method in Sec. V.3. Phonon transmission across a sharp Mg_2Si/Mg_2Sn interface is presented in Sec. V.4, while the phonon transmission and scattering across $Mg_2Si/Mg_2Si_{1-x}Sn_x$ interface are studied in Sec. V.5.

V.3 Phonon dispersion of Mg_2Si, Mg_2Sn and their superlattice

Since the lattice in the interfacial region is distorted and the atoms near the interface interact with other species, an accurate force field that can not only correctly describe the interatomic

interaction within the unstrained bulk phases, but also the strained ones with specie mixing is essential. To evaluate the performance of the MA and the HOFCM on predicting the harmonic force constants in Mg_2Si/Mg_2Sn systems, we study the phonon dispersion of the unstrained and strained Mg_2Si and Mg_2Sn crystals, and the phonon density of states (DOS) of a short-period Mg_2Si/Mg_2Sn superlattice using the three first-principles-based methods to generate harmonic force constants: (a) the direct method with the actual pseudopentials of Si and Sn, (b) the MA with the pseudopotential generated according to Eq. (2) with $\{\sigma_{\mathbf{R}}\}=0$, and (c) the HOFCM, which improves the harmonic force constants from the MA with the higher-order terms, as detailed in Section II.(A).

Figure 2(a) shows the calculated phonon dispersion curves of Mg_2Si and Mg_2Sn in comparison with the neutron scattering experimental data [230, 231]. The overall agreement between the experimental data and the direct DFT calculations with Si/Sn pseudopotentials is excellent, except that a small difference (approximately 10% at Γ point) exhibits in the optical phonon modes. This small discrepancy is mainly due to the well-known red shift of the longitudinal optical (LO) phonon modes away from the transverse optical (TO) phonon modes (LO-TO splitting) in polar materials [232]. Since we do not consider the long-range interaction raised by the Born effective charge, the LO and TO modes intersect at the Γ point. While such a discrepancy in dispersion curves could be corrected by introducing a non-analytical term that is related to the Born effective charge into the dynamical matrix, taking all force constants in real space into account could be challenging. Since only a small portion of phonons is affected compared with the whole first Brillouin zone, we can expect that the LO-TO splitting has negligible effects on phonon transmission and the interfacial thermal conductance. To directly evaluate the influence of LO-TO on phonon transport, we also calculated phonon DOS with and without LO-TO splitting by

including the non-analytical term into the dynamical matrix. Figure V.2(b) shows that the DOS is almost unchanged by including LO-TO splitting.

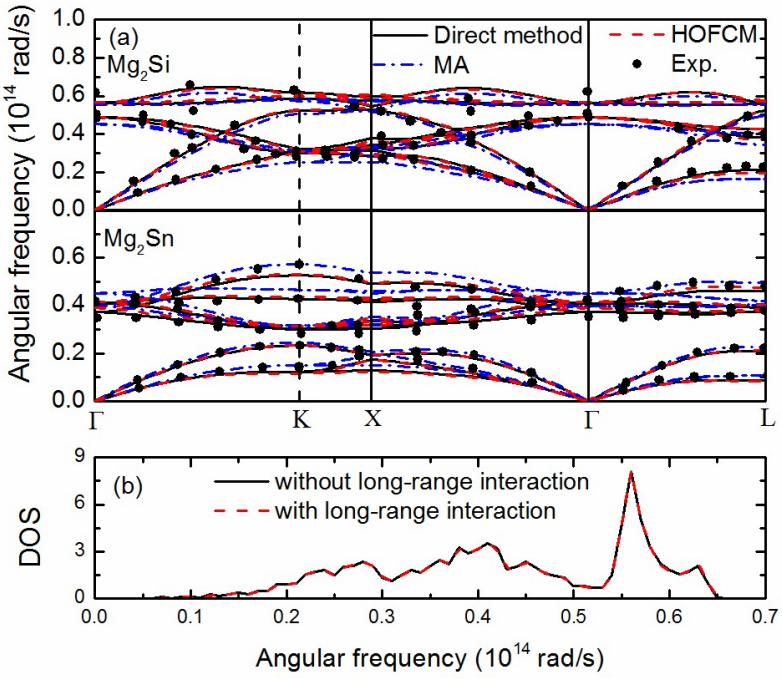

Figure V.2. (a) Calculated phonon dispersions of Mg_2Si and Mg_2Sn using the force constants from the first-principles calculations: the direct method, the MA, and the HOFCM, in comparison with the measured phonon dispersions from inelastic neutron scattering experiments [230, 231]. *(b) Calculated phonon DOS of Mg_2Si from the direct method with and without including the long-range interaction due to the Born effective charge.*

The phonon dispersion curves of both Mg_2Si and Mg_2Sn calculated using the HOFCM almost overlap with that from the direct method, indicating that the HOFCM has the similar accuracy as that of the DFT calculations using the species' own pseudopotentials. It is rather clear that the MA underestimates the frequencies of both acoustic and optical modes of Mg_2Si, but overestimates

those of Mg_2Sn. By examining the spring constants between Mg and its first-nearest neighbor Si (or Sn), defined as the trace of the harmonic force constants of Mg and Si(Sn) pairs, the bonding in Mg_2Si is found to be 16% stiffer than Mg_2Sn. The bonding in the virtual crystal lies in the middle of those of Mg_2Si and Mg_2Sn. Consequently, under the MA, the bonding stiffness in Mg_2Si is weakened which leads to the downshift of phonon dispersion, while the opposite trend occurs in Mg_2Sn.

Figure V.3 shows the phonon dispersion of the strained Mg_2Si and strained Mg_2Sn, which are stretched or compressed to the averaged lattice constant of them to mimic the deformed lattice near the interface. Similar to the unstrained cases, the phonon dispersions calculated using the HOFCM are in good agreement with the direct method, but the results from the MA deviate to some extent. It is noted that the third-order anharmonic force constants do not participate in the refining of the harmonic force constants in the HOFCM since the relative positions of atoms in the strained crystal are unchanged compared with the reference structure where the force constants are extracted. The differences of the harmonic interatomic force constants for the strained cases examined here from the MA and the HOFCM are thus purely originated from the third-order force constants involving the atom type $\{\sigma_{\mathbf{R}}\}$. This observation indicates the importance of taking the atom type into consideration when determining the accurate interatomic force constants, which is ignored in the conventional MA.

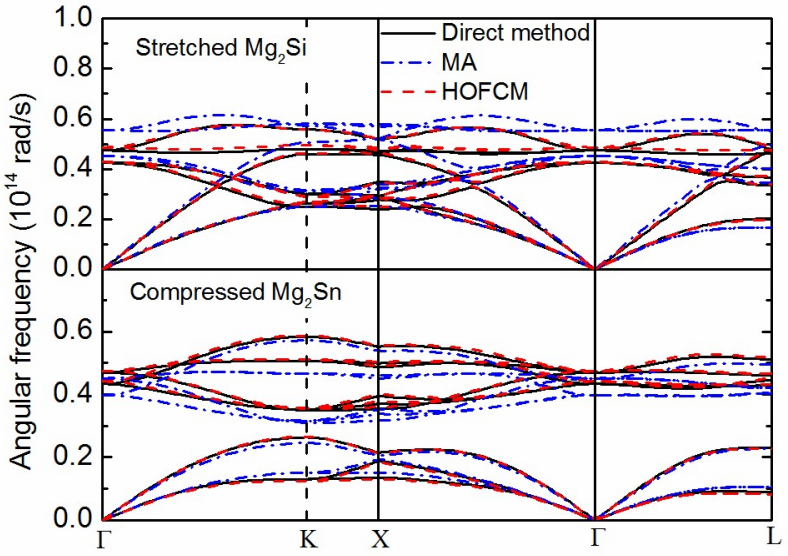

Figure V.3. Phonon dispersions of stretched Mg_2Si and compressed Mg_2Sn computed using the force constants from the direct method, the MA, the HOFCM. Mg_2Si and Mg_2Sn are strained to the same averaged lattice constant of them to mimic the deformed lattice near the interface.

To test whether the HOFCM can represent the interactions between different species, we study the phonon properties of a superlattice, whose crystal structure can be regarded as a conventional unit cell of Mg_2Si but with half of the Si atoms replaced by the Sn atoms (See. Fig. V.4(a)). In this crystal, the Si atoms interact with the Sn atoms in a fashion similar to the interfacial region. The phonon DOS of this superlattice is shown in Fig. V.4(b). While the curve of the phonon DOS from the HOFCM almost follows that from the direct method, there is considerable deviation for middle-to-high-frequency phonons in the MA from the direct method. The deviation could be related to the lattice deformation within the lattice. The phonons whose wavelengths are smaller than or comparable to the scale of lattice deformation are likely to be strongly affected [233]. Since the

MA does not consider the lattice deformation, the transmission of the short wavelength phonons, which are usually middle-to-high-frequency phonons, are not accurately calculated using the MA.

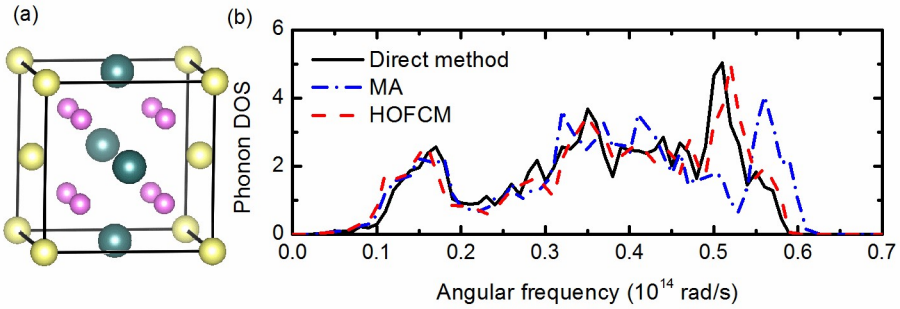

Figure V.4. (a) Lattice structure of Mg_2Si/Mg_2Sn superlattice. The small, medium and large atoms are Mg, Si and Sn, respectively. (b) Phonon DOS of Mg_2Si/Mg_2Sn superlattice calculated using the force constants from the direct method, the MA, the HOFCM.

V.4 Phonon transmission across a sharp Mg_2Si/Mg_2Sn interface

To show the importance of accurate force constants on phonon transmission calculation, we study the phonon transmission across a sharp Mg_2Si/Mg_2Sn interface. Two bulk Mg_2Si and Mg_2Sn crystals are connected with each other in a periodic box to form two interfaces, as shown in Fig. V.5(a). After performing the minimization of the total energy of the crystal, we take half of the system with one interface as the interfacial region to conduct the AGF calculation, as shown in Fig. V.5(b). The harmonic force constants of the interfacial region are generated according to atomic configuration after energy minimization. The atoms near the middle region of each phase are evenly distributed due to the reflection symmetry, and these regions are used to calculate the harmonic force constants of the two reservoirs. To ensure the distorted lattice near the interface,

which scatter the phonons, included in the interfacial region in our calculations, the total length of the simulation box is carefully tested. We calculate the phonon transmission using simulation boxes with total lengths of 36 times and 48 times of the average lattice constant a_0 of Mg_2Si and Mg_2Sn, which correspond to an 18 and a 24 unit-cell-long interfacial region, and found the phonon transmissions from the two calculations are identical. This indicates that an 18 unit-cell interfacial region is sufficiently long to include the distorted lattice and ensure that the calculated phonon transmission is converged if the size is further increased. For MA, we use Eq. (VI.2) to generate the pseudopotential with $\{\sigma_{\mathbf{R}}\}=0$ for Mg_2Si/Mg_2Sn interfaces.

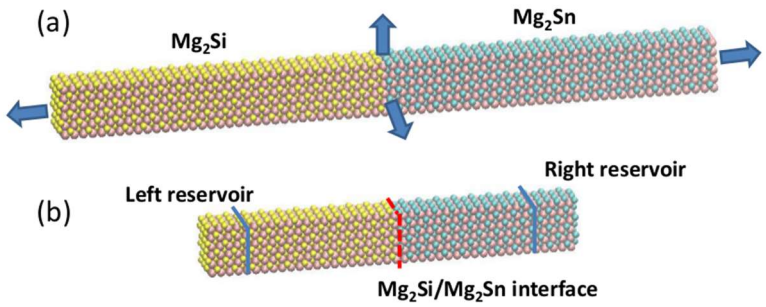

Figure V.5. (a) The atomic system used to perform energy minimization. The arrows indicate the periodic boundary condition. (b) The atomic system for the AGF calculation. The yellow, cyan and pink atoms are Si, Sn and Mg, respectively.

The phonon transmission curves from Mg_2Si to Mg_2Sn calculated from both the MA and the HOFCM are shown in Fig. V.6(a). The phonon DOS of the two reservoirs are also presented in Fig. V.6(b) and (c). Both phonon transmission curves show a similar trend. In the middle frequency region ($0.25-0.3\times10^{14}$ rad/s), there is a region with zero-transmission from both the HOFCM and the MA calculations. The zero phonon transmission is due to the frequency-gap

between the acoustic and optical branches of Mg_2Sn. Any phonons in Mg_2Si with frequency lying in the gap of Mg_2Sn phonon dispersion cannot transmit, since Mg_2Sn cannot support any phonon modes with such frequencies. At the low frequency region below the gap, the phonon transmission is relatively high, close to unity. This is because the phonon DOS in Mg_2Sn side is much larger than that in Mg_2Si and there can be multiple phonons in the Mg_2Sn side with similar low-frequency to match the incoming phonons from the Mg_2Si side [223]. At the high frequency region, the transmissions for both cases are much lower than unity, indicating that high-frequency phonons are more likely to be scattered at the Mg_2Si/Mg_2Sn interface since the phonon dispersions of Mg_2Si and Mg_2Sn become quite different.

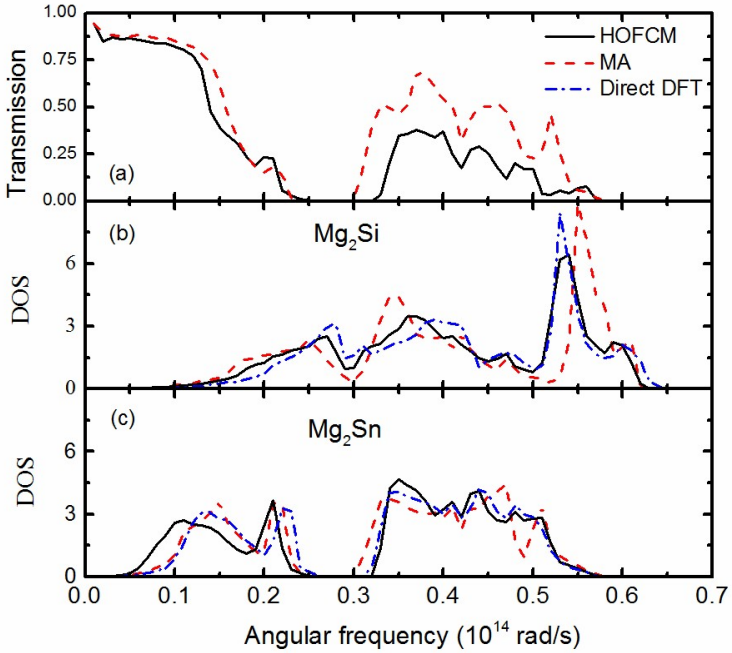

Figure V.6. (a) Frequency-dependent phonon transmission across a sharp Mg_2Si/Mg_2Sn interface. (b) Phonon DOS of Mg_2Si. (c) Phonon DOS of Mg_2Sn.

However, there are some quantitative differences. The MA predicts a smaller zero-transmission gap than HOFCM. The difference in the zero-transmission gap could be explained by the phonon DOS of the Mg_2Sn reservoir calculated from these two methods, as shown in Fig. V.6(c). By comparing phonon DOS calculated from the direct method, the MA and HOFCM of the DFT calculations, we found that the HOFCM gives almost identical phonon DOS results as the direct method and the MA renders a much smaller gap than the HOFCM and the direct method.

In addition to the different DOS results calculated from the MA and HOFCM which can easily explain the difference in zero phonon transmission gap, the over-prediction of the phonon transmission at high-frequency ($> 0.3\times10^{14}$ rad/s) by the MA, as shown in Fig. V.6(a), is likely due to the absence of the local force field scattering in the MA. This could be understood from the wave nature of phonons. Phonons are more likely to be scattered by the strain field whose characteristic size is comparable to the phonon wavelength λ. Since the strain field around the sharp interface spans a few unit cells, the phonons with small wavelength or large wavenumber ($k = 2\pi / \lambda$) are strongly affected. According to the phonon dispersion in Fig. V.3, low-frequency phonons are the modes in LA and TA branches with small wavenumber. On the other hand, phonons away from the Γ point are of middle and high frequency. Therefore, the transmission function of low-frequency phonons calculated from the MA and the HOFCM have a closer match, while the transmission of high-frequency phonons from the HOFCM is much smaller than that from the MA due to the strain field scattering.

Due to the over-predicted phonon transmission for the entire phonon spectra, the interfacial thermal conductance is overestimated by the MA, as shown in Fig. V.7. The discrepancy becomes more evident at high temperature. The interfacial thermal conductance from the MA at high temperature is almost twice as large as that from the HOFCM. At low temperature the thermal

conductance is mainly contributed by low-frequency phonons and both methods give similar phonon transmission for these low-frequency phonons. At high temperature, the high-frequency phonons, whose transmission is more significantly over-estimated under the MA, are excited and begin to participate in the energy transport.

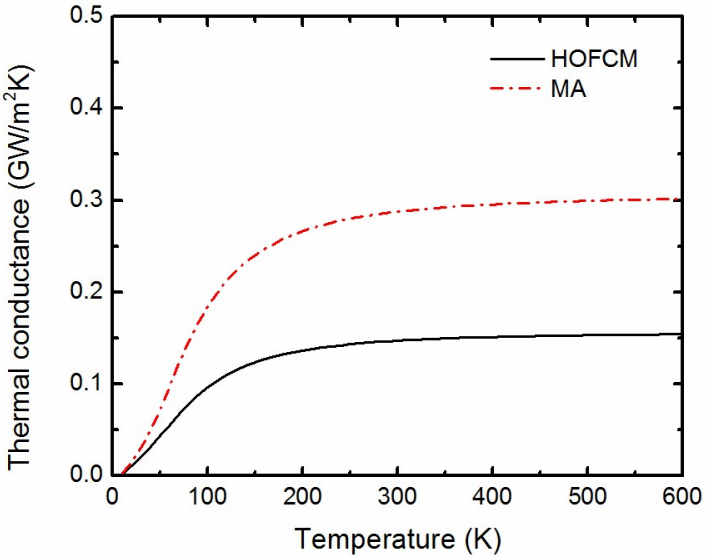

Figure V.7. Interfacial thermal conductance across Mg_2Si/Mg_2Sn interface at different temperature. The MA overpredicts the interfacial thermal conductance.

V.5 Phonon transmission across $Mg_2Si/Mg_2Si_{1-x}Sn_x/Mg_2Si$

In this section, we study the phonon transmission and scattering across $Mg_2Si/Mg_2Si_{1-x}Sn_x/Mg_2Si$ structures with the HOFCM to explore the phonon transport across interfaces made up of a crystal and its alloys. This kind of interfaces play an important role in increasing the figure of merit of the "nanoparticle in alloy" thermoelectric materials by reducing its thermal conductivity

below the alloy limit [185, 234]. In "nanoparticle in alloy" thermoelectric materials, the short-wavelength phonons are scattered by alloy scattering while the long-and-middle-wavelength phonons are scattered by the nanoparticles whose size can be tuned. Great progress has been made over the past decade on developing more efficient thermoelectric materials using such nanostructuring approach [51]. However, the detailed and systematic understanding on frequency-dependent phonon transmission across such kind of interfaces has not been developed.

Figure V.8(a) illustrates the atomic system used in the AGF simulations, where an $Mg_2Si_{1-x}Sn_x$ alloy layer with a thickness of L unit cells is sandwiched between two semi-infinite Mg_2Si crystals. The dimension of the cross-section is $2a_0 \times 2a_0$ and the periodic boundary condition is imposed when the simulation system is relaxed. Figure V.8(b) shows the phonon transmission across the alloy layer with different Sn compositions, x, when the length of the alloy layer L is fixed at 10 unit cells. When x is small, the phonon transmission always decreases with the increase of x for the entire phonon spectra due to the increasing scattering events in the alloy layers. The transmission curves exhibit a similar shape, where the peaks and valleys in the curves occur at the almost the same phonon frequency when the Sn concentration (x) is low. By examining the phonon transmission through alloy layers with other thickness, we even found that the phonon transmission across the alloy $Mg_2Si_{1-x}Sn_x$ with a thickness of $2L$, $T_{2L}^{x}(\omega)$, can be well approximated by that across the alloy $Mg_2Si_{1-2x}Sn_{2x}$ with a thickness of L but with $2x$ Sn concentration $T_{L}^{2x}(\omega)$, as shown in Fig. V.9(a) and (b). This indicates that the transmission is mainly determined by the total number of Sn atoms, which serves as alloy scattering centers, but is weakly dependent on the distribution of Sn atoms. Such a scaling relation indicates that the phonons are mainly scattered by the defects in the alloy layer and the scattering events due to the Sn defects can be regarded as independent events. However, when $x > 0.4$, such simple scaling relation does not work well.

$T_{2L}^{0.4}(\omega)$ exhibits very different features from $T_{L}^{0.8}(\omega)$, as shown in Fig. V.9(c). For example, there is a zero-transmission region for middle-frequency phonons, which is the signature of phonon DOS in Mg_2Sn. This is understandable because when x = 1.0, the interface becomes a sharp Mg_2Si/Mg_2Sn interface, but as x decreases, the Si atoms within the alloy layers act as defects leading to additional scattering.

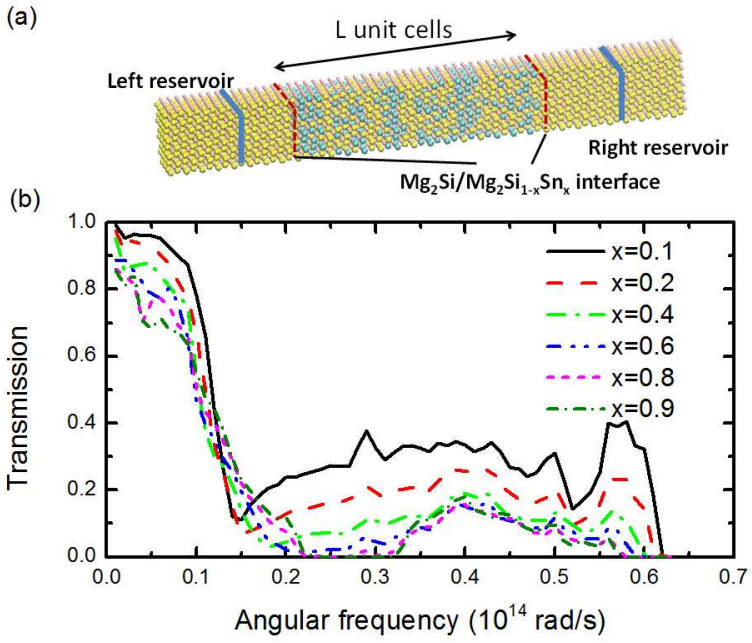

Figure V.8. (a) The schematic of the simulation system of $Mg_2Si/Mg_2Si_{1-x}Sn_x/Mg_2Si$ structure. (b) Phonon transmission across the $Mg_2Si/Mg_2Si_{1-x}Sn_x/Mg_2Si$ structure as a function of phonon frequency for different Sn compositions (x). The length of the alloy layers is fixed at 10 unit cells.

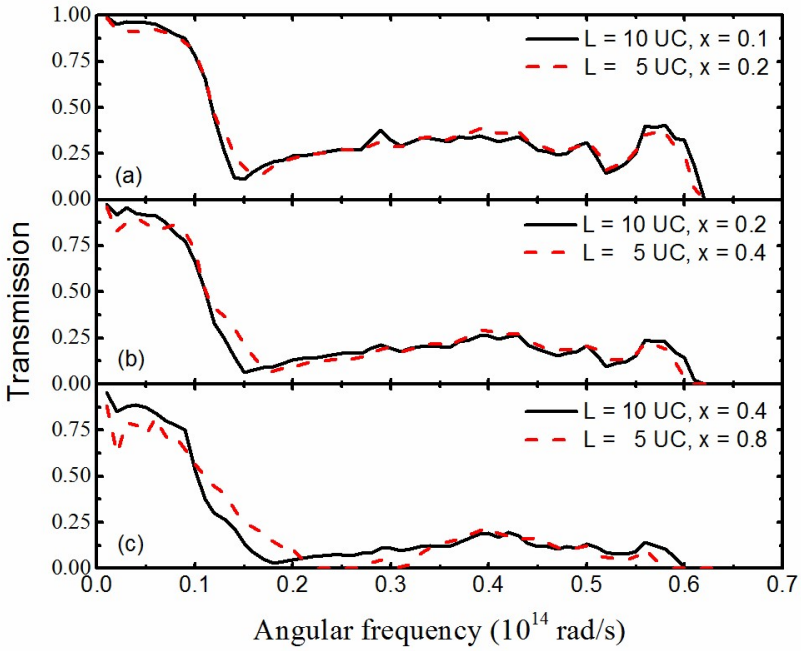

Figure V.9. Phonon transmission across the $Mg_2Si/Mg_2Si_{1-x}Sn_x/Mg_2Si$ structure as a function of phonon frequency for alloy layers with different Sn compositions and thickness.

To observe the collective behaviors of all phonons transmitting through the structure, the thermal resistance, or the inverse of the thermal conductance, across the structures with different L at 300 K, was calculated and shown in Fig. V.10. The total thermal resistance is found to be proportional to the length for each Sn concentration x , and their relation can be well fitted by

$$R_{\text{total}} = 2R_{\text{interface}} + \frac{L}{K_{\text{alloy}}}, \tag{V.12}$$

In this relation, R_{total} is the total thermal resistance, the coefficients $R_{\text{interface}}$ and K_{alloy} can be interpreted as the interfacial resistance of each $Mg_2Si/Mg_2Si_{1-x}Sn_x$ interface and the effective thermal conductivity of the alloy layer. By linear fitting of this relation, the interfacial resistance of $Mg_2Si/Mg_2Si_{1-x}Sn_x$ interfaces, as well as the thermal conductivity of $Mg_2Si_{1-x}Sn_x$ alloy, can be extracted. Strictly speaking, both the interfacial thermal conductance and thermal conductivity

could be size dependent especially if the simulated size is smaller than the mean free path of phonons. We estimate the average mean free path of phonons using the simple kinetic theory. Considering the thermal conductivity of $Mg_2Si_{1-x}Sn_x$ ~3 W/mK, the specific heat ~70 J/mol.K and the sound velocity ~ 5000 m/s, the average phonon mean free path is ~ 1 nm. The size of the alloy layers we simulated is usually larger than this value, which justifies the length-independent $R_{\text{interface}}$ and K_{alloy}.

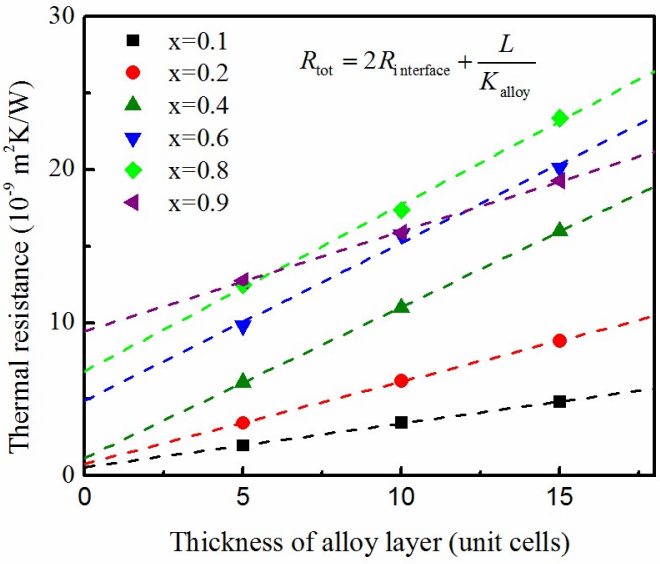

Figure V.10. The total thermal resistance of $Mg_2Si/Mg_2Si_{1-x}Sn_x/Mg_2Si$ structure as a function of the thickness of alloy layers.

The interfacial thermal resistance can be described as a piecewise linear function with x, as shown in Fig. V.11(a). The value of the interfacial resistance is small and weakly dependent on the composition when $x < 0.4$. This trend is consistent with the observation that the phonon transmission is dominated by the individual scattering events within the alloy layer when x is small. For $x > 0.4$, the slope of the interfacial resistance as a function of the Sn composition abruptly jumps to a larger value and the scattering at the interface dominates the transmission process. The

two regimes of interfacial thermal conductance can also be understood by looking at the transition of phonon DOS with the composition shown in Fig. V.12. While the DOS of the alloys retains the shape for high-frequency phonons as that of Mg_2Si at a small x, the peaks seem to disappear when x is larger than 0.4. Therefore, high-frequency phonons from the Mg_2Si phase are less likely to transmit across the $Mg_2Si/Mg_2Si_{1-x}Sn_x/Mg_2Si$ interface due to the relatively small number of phonons available to match these incoming phonons. As a result, the interfacial resistance is larger at a large x because of the important role of high-frequency phonons on thermal conductance according to the Landauer formulism, Eq. (11).

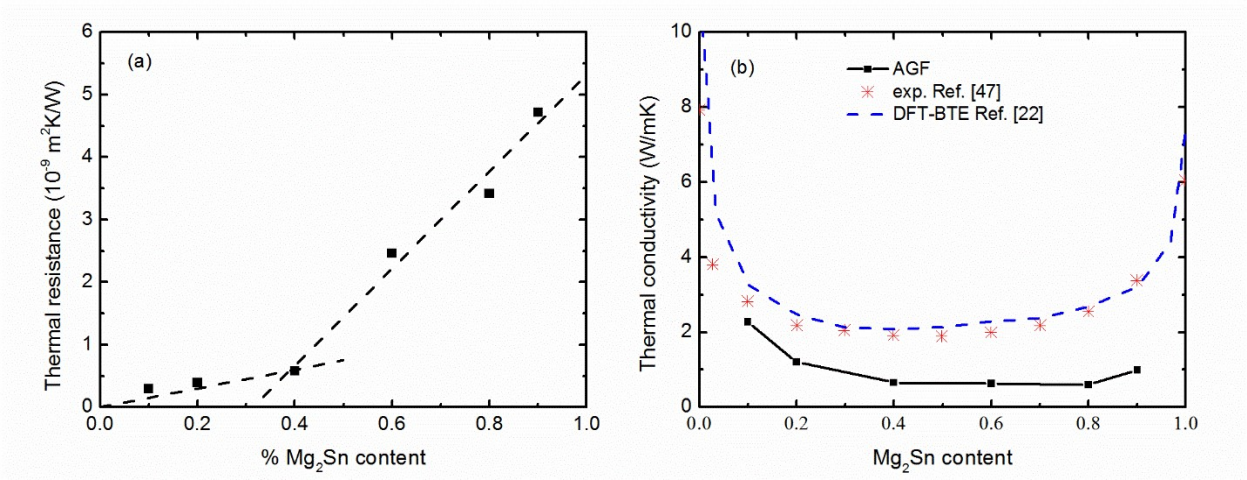

Figure V.11. (a) The extracted interfacial resistance of $Mg_2Si/Mg_2Si_{1-x}Sn_x$ interface as a function of x. (b) The extracted effective thermal conductivity of $Mg_2Si_{1-x}Sn_x$ alloy as a function of x, in comparison with the measured data from Ref. [195] and the PBTE calculation from Ref. [16].

Figure V.11(b) shows the effective lattice thermal conductivity of $Mg_2Si_{1-x}Sn_x$ as a function of the Sn composition, extracted from the AGF calculations, in comparison with the experimental data [195] as well as recent theoretical calculations based on the PBTE theory with interatomic force constants from DFT as inputs [16]. Overall the calculated values from the AGF resemble the

typical experimental trends of alloy thermal conductivity, where the thermal conductivity drops first, then becomes nearly independent of composition and increases again when *x* increases from 0.1 to 0.9. However, the calculated value of thermal conductivity is smaller than the measured data taken from thermoelectric handbook [195]. This observation is counter-intuitive. One would expect that anharmonicity happening in the experimental samples that are not implemented in AGF calculations would lead to a smaller thermal conductivity than the calculated values. However, Paython *et al* had found the similar results in their atomic simulations several decades ago [235]. They provided the qualitative explanation as follows. Under the harmonic approximation, the impurities destroy the translational symmetry so that some of the phonon modes cannot travel from one end to the other end and become localized modes, which do not contribute the heat flux. But with the help of anharmonic coupling, an energy exchange between the localized modes is induced, thus the heat flux is enhanced. As a result, the thermal conductivity of the disorder anharmonic crystal (experimental data) would be even larger than the disordered harmonic crystal (as calculated using the AGF model).

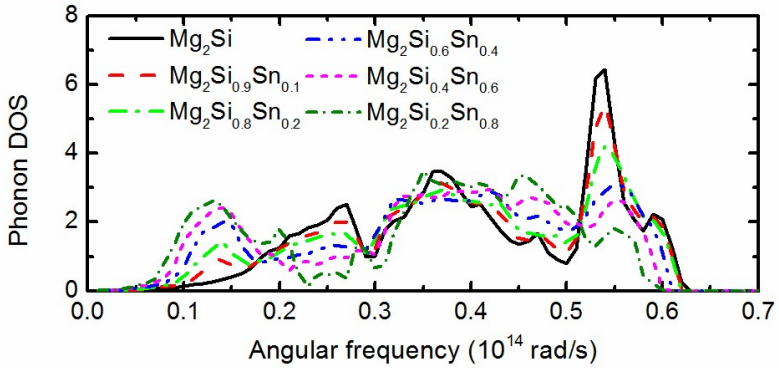

Figure V.12. The calculated phonon DOS of $Mg_2Si_{1-x}Sn_x$ alloys.

V.6 Summary of this chapter

In summary, we employ the HOFCM, which originates from the MA but considers the local force difference due to the different species (including both atom types and lattice constant difference), to efficiently calculate the harmonic force constants of the interfacial regions, and then integrate the obtained force constants from the first-principles calculations with the AGF approach to study phonon transmission across $Mg_2Si/Mg_2Si_{1-x}Sn_x$ interface. Starting from the harmonic interatomic force constants from the VCA, the HOFCM uses the higher-order terms which are related to the atomic displacement and atomic species to improve the accuracy of the harmonic force constants from the VCA. The HOFCM is found to be computationally affordable to extract the harmonic interatomic force constants from DFT calculations by taking the advantage of the VCA when comparing with the direct method, while yielding phonon dispersion closer to the direct DFT method in comparison with the MA. DFT-AGF approach was developed using the force constants calculated from both the MA and the HOFCM. It is found that the MA over-predicts the phonon transmission and interfacial thermal conductance across Mg_2Si/Mg_2Sn interface due to the absence of the internal strain field scattering for high frequency phonons in the MA. The frequency-dependent phonon transmission across an interface between a crystal and an alloy, which often appears in high efficiency "nanoparticle in alloy" thermoelectric materials was studied. The interfacial thermal resistance across $Mg_2Si/Mg_2Si_{1-x}Sn_x$ interface is found to be weakly dependent on the composition of Sn when the composition is less than 40%, but increases rapidly when it is larger than 40% due to the transition of the high-frequency phonon DOS in $Mg_2Si_{1-x}Sn_x$ alloys.

CHAPTER VI CONCLUSIONS AND FUTURE WORK

In this thesis, we have developed the first-principles-based simulation tools to predict the thermal conductivity of two-dimensional crystal materials and study the phonon transmission across interfaces between two dissimilar materials.

The effects of crystal structure, atomic mass, bonding stiffness, layer thickness and embedded nanodomains on thermal conductivity of silicene and TMDs are investigated. These findings could guide the synthesis of novel two-dimensional materials with desirable thermal properties or fabricate high-performance and reliable two-dimensional-material-based nanodevices. There are still a few issues needed to be addressed in the future.

The main inputs for thermal conductivity calculation are the interatomic force constants. In our current implementation, we extract these force constants under 0 K. However, it has been realized that using these force constants to calculate phonon dispersion and phonon scattering rates of the materials at high temperature condition could lead to deviation between the calculated results and the experimental data [236]. To solve this problem, *ab initio* molecular dynamics should be performed at the temperature that are of interest, and the interatomic force constants could be extracted by fitting the relation between atomic forces and displacements. Because of the thermal expansion effects, the lattice constants of the crystal cannot be determined through simple energy minimization as we do at 0 K condition. A series of *ab initio* molecular dynamics simulations have to be performed, which brings severe computational burden, in particular for crystals with less symmetry. It would be highly desirable if efficient methods can be proposed to accelerate the procedures to extract interatomic force constants at high temperature.

In our PBTE approach, we only considered the three-phonon, phonon-boundary, phonon-isotope, phonon-alloy and phonon-nanodomain scatterings. However, a few scattering

mechanisms are ignored, some of which might not be neglected in some situations. For example, at high temperature four-phonon scattering processes should be important. Although some literatures suggested that it could be neglected below 1000 K [121], the criteria should be material-dependent. In many device applications, two-dimensional materials are supported by the substrates. According to previous study on the supported graphene, the substrate could influence the thermal conductivity of two-dimensional materials in a complicated manner [237, 238]. The interaction between phonon and substrate should also be considered in the PBTE.

Our efforts on AGF approach enable us to study phonon transmission and interfacial thermal conductance with accurate force constants from first-principles simulations. With this powerful tool, we are able to study the roles of mass disorder and strain field disorder on the phonon transport across the interface. However, the AGF approach studied in this thesis is based on harmonic approximation, and inelastic effects are ignored. It is clearly seen from Figure V.11 that the harmonic approximation could lead to underestimation of interfacial thermal conductance and thermal conductivity. The future work will aim to include the phonon-phonon scattering effects in Green's function by solving the anharmonic self-energy term [239].

APPENDIX

A.1 The shape of silicene's ZA phonon dispersion

Instead of the definition of dynamical matrix from Eq. (II.3), the dynamical matrix can also be defined as [96]

$$C_{\tau\tau'}^{\alpha\beta}(\mathbf{q}) = \frac{1}{\sqrt{M_\tau M_{\tau'}}} \sum_{\mathbf{R}'} \phi_{\mathbf{0}\tau,\mathbf{R}'\tau'}^{\alpha\beta} e^{i\mathbf{q}\cdot\mathbf{X}_{\mathbf{R}'\tau'}}, \tag{A.1}$$

where $\mathbf{X}_{\mathbf{R}'\tau'}$ is the position of atom $\mathbf{R}'\tau'$. The two definitions of dynamical matrix give the identical phonon dispersion relation [96]. It is more convenient to derive the dispersion relation close to the Gamma point using Eq. (A.1) as the definition.

The dynamical matrix of a wavevector $\mathbf{q} = q\mathbf{u}$ ($\mathbf{u}$ is a unit vector in the *x*-*y* plane) can be calculated from the dynamical matrix of its neighbor wavevector $\mathbf{q}_0$ ($\mathbf{q} = \mathbf{q}_0 + \Delta\mathbf{q}$) as a perturbation

$$\begin{aligned} C_{\tau\tau'}^{\alpha\beta}(\mathbf{q}) &= \frac{1}{\sqrt{M_\tau M_{\tau'}}} \sum_{\mathbf{R}'} \phi_{\mathbf{0}\tau,\mathbf{R}'\tau'}^{\alpha\beta} e^{i\mathbf{q}\cdot\mathbf{X}_{\mathbf{R}'\tau'}} = \frac{1}{\sqrt{M_\tau M_{\tau'}}} \sum_{\mathbf{R}'} \phi_{\mathbf{0}\tau,\mathbf{R}'\tau'}^{\alpha\beta} e^{i(\mathbf{q}_0+\Delta\mathbf{q})\cdot\mathbf{X}_{\mathbf{R}'\tau'}} \\ &= \frac{1}{\sqrt{M_\tau M_{\tau'}}} \sum_{\mathbf{R}'} \left\{ \phi_{\mathbf{0}\tau,\mathbf{R}'\tau'}^{\alpha\beta} e^{i\mathbf{q}_0\cdot\mathbf{X}_{\mathbf{R}'\tau'}} + i\left(\Delta\mathbf{q}\cdot\mathbf{X}_{\mathbf{R}'\tau'}\right)\phi_{\mathbf{0}\tau,\mathbf{R}'\tau'}^{\alpha\beta} e^{i\mathbf{q}_0\cdot\mathbf{X}_{\mathbf{R}'\tau'}} \right. \\ &\quad \left. -\frac{1}{2}\left(\Delta\mathbf{q}\cdot\mathbf{X}_{\mathbf{R}'\tau'}\right)^2 \phi_{\mathbf{0}\tau,\mathbf{R}'\tau'}^{\alpha\beta} e^{i\mathbf{q}_0\cdot\mathbf{X}_{\mathbf{R}'\tau'}} + \ldots \right\} \end{aligned} \tag{A.2}$$

If $\mathbf{q}_0$ is chosen as the Gamma point, Eq. (A.2) can be simplified as

$$
\begin{aligned}
C_{\tau\tau'}^{\alpha\beta}(\mathbf{q}) &= \frac{1}{\sqrt{M_\tau M_{\tau'}}}\sum_{\mathbf{R}'}\left\{\phi_{\mathbf{0}\tau,\mathbf{R}'\tau'}^{\alpha\beta} + i\left(\mathbf{q}\cdot\mathbf{X}_{\mathbf{R}'\tau'}\right)\phi_{\mathbf{0}\tau,\mathbf{R}'\tau'}^{\alpha\beta} - \frac{1}{2}\left(\mathbf{q}\cdot\mathbf{X}_{\mathbf{R}'\tau'}\right)^2\phi_{\mathbf{0}\tau,\mathbf{R}'\tau'}^{\alpha\beta} + \ldots\right\} \\
&= C_{\tau\tau'}^{\alpha\beta}(\mathbf{0}) + iq\frac{1}{\sqrt{M_\tau M_{\tau'}}}\sum_{\mathbf{R}'}\left(\mathbf{u}\cdot\mathbf{X}_{\mathbf{R}'\tau'}\right)\phi_{\mathbf{0}\tau,\mathbf{R}'\tau'}^{\alpha\beta} \\
&\quad -q^2\frac{1}{\sqrt{M_\tau M_{\tau'}}}\sum_{\mathbf{R}'}\left\{\frac{1}{2}\left(\mathbf{u}\cdot\mathbf{X}_{\mathbf{R}'\tau'}\right)^2\phi_{\mathbf{0}\tau,\mathbf{R}'\tau'}^{\alpha\beta}\right\} + \ldots \\
&= C_{\tau\tau'}^{\alpha\beta}(\mathbf{0}) + iqC^{(1)\alpha\beta}_{\tau\tau'} - q^2C^{(2)\alpha\beta}_{\tau\tau'} + \ldots,
\end{aligned}
\tag{A.3}
$$

where $C^{(1)}$ and $C^{(2)}$ are real matrices. Then the eigenvalues are written as

$$
\omega_{\mathbf{q}s}^2 = \omega_{\mathbf{0}s}^2 + iq\left(\varepsilon_{\mathbf{0}s}^{\tau\alpha}\right)^* C^{(1)\alpha\beta}_{\tau\tau'}\varepsilon_{\mathbf{0}s}^{\tau'\beta} - q^2\left(\varepsilon_{\mathbf{0}s}^{\tau\alpha}\right)^* C^{(2)\alpha\beta}_{\tau\tau'}\varepsilon_{\mathbf{0}s}^{\tau'\beta} + \ldots \tag{A.4}
$$

where ε is eigenvector of the dynamical matrix C, and is real at $\mathbf{q}=0$. Since the eigenvalues of any dynamical matrix are always real, the second term in Eq. (A.4) naturally vanishes. Due to the crystal symmetry of silicene, it is easy to prove that $C^{(2)xz}_{\tau\tau'} = C^{(2)yz}_{\tau\tau'} = 0$. Therefore, there is an acoustic branch where the corresponding atomic movement at the Gamma point is pure out-of-plane motion (along z direction), or the ZA branch which is discussed in the main text. The components of its eigenvector are $\varepsilon_{\mathbf{0},\mathrm{ZA}}^{\tau z} = \sqrt{2}/2$, $\varepsilon_{\mathbf{0},\mathrm{ZA}}^{\tau x} = \varepsilon_{\mathbf{0},\mathrm{ZA}}^{\tau y} = 0$ at the Gamma point. The dispersion of this branch becomes quadratic only if the q^2 term in Eq. (A.4) is zero, or

$$
\sum_{\tau'} C^{(2)zz}_{\tau\tau'} = 0, \tag{A.5}
$$

which requires

$$
\left(\mathbf{u}\cdot\mathbf{X}_{\mathbf{R}'\tau'}\right)^2\phi_{\mathbf{0}\tau,\mathbf{R}'\tau'}^{zz} = 0. \tag{A.6}
$$

Physically, Eq. (A.6) indicates the energy of the 2-D crystal unchanged when every atom move a distance of $\theta\cdot\left(\mathbf{u}\cdot\mathbf{X}_{\mathbf{R}'\tau'}\right)$ along z direction, where θ can be regarded as a small angle that the

atomic plane rotates, as illustrated in Fig. A.1. The deformation due to the shear leads to a relative displacement among atoms. Since the original silicene structure is the structure with the minimum energy, the distorted lattice structure has to be of higher energy. Therefore, Eq. (A.6) does not hold for silicene, and there is always a linear component in the ZA dispersion. Such proof provided here can also be applied to other 2-D materials, such as transition metal dichalcogenides.

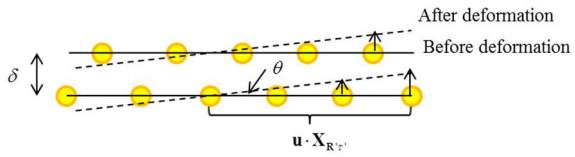

Fig. A.1. The schematic of the shear deformation of silicene.

A.2 The long-wavelength ZA phonon modes in graphene

Although the quadratic dispersion can be obtained from first-principles calculations and widely used for the flexural ZA phonons in graphene, some authors have recently pointed out that the quadratic shape of the ZA modes would lead to strong scatterings with long-wavelength LA and TA modes, making the phonon relaxation time of the LA and TA modes approach a constant for phonon near the zone center $q \to 0$ [66, 103]. Since the condition for the existence of phonons as elementary excitations is $\omega_{\mathbf{qs}}\tau_{\mathbf{qs}} > 1$ [118], the abnormal constant relaxation times of the LA and TA modes raise a concern on whether the phonon concept can even be applied to the long-wavelength acoustic vibrations in graphene. The problem becomes more severe when the sample

size is larger than 1 μm, since the condition $\omega_{\mathbf{q}s}\tau_{\mathbf{q}s}<1$ occurs in the region of the first Brillouin zone where $q<5\times10^{-5}(2\pi/a_0)$, i.e., where the wavelength λ > 1 μm [66, 103]. One possible way to avoid such a concern is to take into account the coupling of ZA and in-plane acoustic phonon modes, in which case the long-wavelength ZA dispersion has the form $\omega\propto q^{3/2}$ [110]. In this work, we slightly modify the ZA dispersion by multiplying the original dispersion relation by the factor $\left[1+(q_c/q)^2\right]^{1/4}$, where q_c is a cutoff wave vector, corresponding to the bending rigidity of $\kappa_0=1.68$ eV, similar to what Lindsay and Broido did in ref. [67]. The modified ZA branch is then plotted in Fig. 2(a). It is seen that such modification does not change the dispersion of middle- and short-wavelength phonons, but turns the quadratic dispersion to $\omega\propto q^{3/2}$ near the zone center, making $v\propto q^{1/2}$ and $n^0\propto q^{-3/2}$ for long wavelength ZA phonons. We have thus used the modified dispersion for flexural ZA modes in the calculation of thermal conductivity and phonon scattering rate of graphene in this work.

A.3 Analytical limit of the scattering rates of graphene's acoustic phonon modes

For a three-phonon process in a two-dimensional material, if the mode $\mathbf{q}s$ is fixed and the branch indices s' and s'' of the other two modes, $\mathbf{q}'s'$ and $\mathbf{q}''s''$ ($\mathbf{q}''=\mathbf{q}\pm\mathbf{q}'+\mathbf{G}$), are given, the wavevector $\mathbf{q}'$ has to be on a loop $t(\mathbf{q}')$ in the first Brillouin zone that is determined by the energy conservation condition $\omega_{\mathbf{q}s}\pm\omega_{\mathbf{q}'s'}=\omega_{(\mathbf{q}\pm\mathbf{q}'+\mathbf{G})s''}$. The two-dimensional integral, Eq. (II.14), can then be converted to a line integral, which is written as [66]

$$\Gamma_{\mathbf{q}s} \propto \int_{t(\mathbf{q}')} \frac{\left|V_3\right|^2 (1+n^0_{\mathbf{q}'s'}+n^0_{\mathbf{q}''s''})}{\left|\partial\left(\omega_{\mathbf{q}s}-\omega_{\mathbf{q}'s'}-\omega_{\mathbf{q}''s''}\right)/\partial\mathbf{q}'\right|}dt \quad \text{(for decay processes),} \tag{A.7}$$

$$\Gamma_{\mathbf{q}s} \propto \int_{t(\mathbf{q}')} \frac{\left|V_3\right|^2 (n^0_{\mathbf{q}''s''}-n^0_{\mathbf{q}'s'})}{\left|\partial\left(\omega_{\mathbf{q}s}+\omega_{\mathbf{q}'s'}-\omega_{\mathbf{q}''s''}\right)/\partial\mathbf{q}'\right|}dt \quad \text{(for annihilation processes).} \tag{A.8}$$

To scatter a long-wavelengh phonon mode $\mathbf{q}s$ on a linear dispersion with two other phonon modes $\mathbf{q}'s'$ and $\mathbf{q}''s''$ which are on a dispersion with $\omega \propto q^{3/2}$, it is easy to show that $q' \propto q^{2/3}$ and $q'' \propto q^{2/3}$ to satisfy the energy conservation condition. As a result, the perimeter of the loop $t(\mathbf{q}')$ is on the of order $q^{2/3}$, $(1+n^0_{\mathbf{q}'s'}+n^0_{\mathbf{q}''s''})$ is on the of order q^{-1} and the gradient is on the of order $q^{1/3}$. Now, the only unknown quantity is the three-phonon scattering matrix element $\left|V_3\right|^2$. Take the LA phonon in graphene as an example, Eq. (II.6) can be written as

$$V_3 \propto \frac{\sum_{\tau}\sum_{\mathbf{R}'\tau'}\sum_{\mathbf{R}''\tau''}\Psi^{xzz}_{0\tau,\mathbf{R}'\tau',\mathbf{R}''\tau''}e^{i\mathbf{q}\cdot(\mathbf{r}_\tau-\mathbf{R}''-\mathbf{r}_{\tau''})}e^{i\mathbf{q}'\cdot(\mathbf{R}'+\mathbf{r}_{\tau'}-\mathbf{R}_{\mathbf{R}''}-\mathbf{r}_{\tau''})}}{\left(\omega_{\mathbf{q}s}\omega_{\mathbf{q}'s'}\omega_{\mathbf{q}''s''}\right)^{1/2}}. \tag{A.9}$$

By expanding the exponential in powers of q, we can get the terms of $1, q^{2/3}, q, q^{4/3}, q^{5/3}, q^2, q^{7/3}, \ldots$ In Ref. [66], the authors proved that the coefficients of the first six terms would be zero due to the acoustic summation rule and mirror symmetry of the graphene sheet. Since the first nonzero term is $q^{7/3}$, the scattering matrix element $\left|V_3\right|^2$ scales with $q^{5/3}$, and finally the scattering rate due to the LA->ZA+ZA process should follow the relation as $\Gamma_{\mathbf{q}s} \propto q$ as $q \to 0$.

A.4 Analytical limit of the scattering rates of silicene's acoustic phonon modes

In Sec. III(D), we discussed three possible scattering mechanisms for a long-wavelength acoustic phonon mode $\mathbf{q}s$ that satisfies the same linear phonon dispersion. One is the decay process that scatters into two long-wavelength acoustic modes $\mathbf{q}'s'$ and $\mathbf{q}''s''$. The other two are the annihilation scattering with a high-frequency mode $\mathbf{q}'s'$ and generate another high-frequency mode $\mathbf{q}''s''$ that could be on the same branch as $\mathbf{q}'s'$ or on a different branch.

In the first case, all of the three long-wavelength modes are on the linear dispersion curves, and the scattering matrix can be derived from a continuum model, which gives $|V_3|^2 \propto qq'q''$ [99]. Since both q' and q'' are in the order of q(otherwise energy conservation condition cannot be satisfied), we can get these scaling relations: $|V_3|^2 \propto q^3$, $\left(1+n^0_{\mathbf{q}'s'}+n^0_{\mathbf{q}''s''}\right) \propto q^{-1}$ and $\left|\nabla_{\mathbf{q}'}\left(\omega_{\mathbf{q}s}-\omega_{\mathbf{q}'s'}-\omega_{\mathbf{q}''s''}\right)\right| \propto 1$ through some algebra. In addition, the perimeter of the loop $t(\mathbf{q}')$ is in the same order of q'. Therefore, the scattering rate $\Gamma_{\mathbf{q}s}$ due to the decay processes into two long-wavelength modes is in the order of q^3 according to Eq. (A.7).

In the other two cases, $\mathbf{q}'s'$ and $\mathbf{q}''s''$ are not long-wavelength modes. The scattering matrix element $|V_3|^2$ becomes proportional to q and $\left(n^0_{\mathbf{q}''s''}-n^0_{\mathbf{q}'s'}\right)$ can be estimated by $n^0\left(\omega_{\mathbf{q}''s''}\right)-n^0\left(\omega_{\mathbf{q}'s'}\right)=\left[\partial n^0\left(\omega_{\mathbf{q}'s'}\right)/\partial\omega_{\mathbf{q}'s'}\right]vq \propto q$, which $v_{\mathbf{q}s}q$ is the energy of $\mathbf{q}s$. If modes $\mathbf{q}'s'$ and $\mathbf{q}''s''$ are on the same branch, the gradient $\left|\nabla_{\mathbf{q}'}\left(\omega_{\mathbf{q}s}-\omega_{\mathbf{q}'s'}+\omega_{\mathbf{q}''s''}\right)\right|$ can be estimated by $\left|\left(\partial\omega_{\mathbf{q}'s'}/\partial\mathbf{q}'\right)\cdot\mathbf{q}\right| \propto q$ and the perimeter of the loop $t(\mathbf{q}')$ is a finite value. Then according to Eq.

(A.8) we can obtain $\Gamma_{\mathbf{q}s} \propto q$ for the second case. If $\mathbf{q}'s'$ and $\mathbf{q}''s''$ are not on the same branch, $\left|\nabla_{\mathbf{q}'}\left(\omega_{\mathbf{q}s}-\omega_{\mathbf{q}'s'}+\omega_{\mathbf{q}''s''}\right)\right|=\left|\mathbf{v}_{\mathbf{q}'s'}-\mathbf{v}_{\mathbf{q}''s''}\right|$ is a finite number. Now, $\Gamma_{\mathbf{q}s} \propto q^2$ for the third case.

A.5: Imposing translational and rotational invariance to the fitting for interatomic force constants

First-principles calculations are performed to obtain the displacement-type-force relation, Eq. (VI.5), which are linear equations with respect to the interatomic force constants ϕ, ψ, χ J and G. To obtain physically correct interatomic force constants, the translational and rotational invariances have to be considered when solving Eq. (VI.5) with linear fitting. The translational invariance relations, which indicate that the energy of a system is a constant value when all atoms are displaced the same amount distance along a given direction, are expressed as [216, 219]

$$\begin{gathered}\sum_{\mathbf{R}'}\phi_{\mathbf{RR}'}^{\alpha\beta}=0,\ \ \forall\left(\mathbf{R},\alpha\beta\right)\\ \sum_{\mathbf{R}''}\psi_{\mathbf{RR}'\mathbf{R}''}^{\alpha\beta\gamma}=0,\ \forall\left(\mathbf{RR}',\alpha\beta\gamma\right)\\ \sum_{\mathbf{R}'}\chi_{\mathbf{RR}'\mathbf{R}''}^{\alpha\beta}=0,\ \forall\left(\mathbf{RR}',\alpha\beta\right)\end{gathered}\tag{A.9}$$

The rotational invariances, which ensure the constant system energy when all atoms are rotated a small angle along any axis, are written as [216, 219]

$$\begin{gathered}\sum_{\mathbf{R}'}\phi_{\mathbf{RR}'}^{\alpha\beta}\left(\mathbf{R}'\right)^{\gamma}\varepsilon^{\beta\gamma\nu}=0,\ \ \forall\left(\mathbf{R},\alpha\beta\right)\\ \sum_{\mathbf{R}''}\psi_{\mathbf{RR}'\mathbf{R}''}^{\alpha\beta\gamma}\left(\mathbf{R}''\right)^{\delta}\varepsilon^{\gamma\delta\nu}+\phi_{\mathbf{RR}'}^{\gamma\beta}\varepsilon^{\gamma\alpha\nu}+\phi_{\mathbf{RR}'}^{\alpha\gamma}\varepsilon^{\gamma\beta\nu}=0,\ \forall\left(\mathbf{RR}',\alpha\beta\gamma\right)\\ \sum_{\mathbf{R}'}\chi_{\mathbf{RR}'\mathbf{R}''}^{\alpha\beta}\left(\mathbf{R}'\right)^{\gamma}\varepsilon^{\beta\gamma\nu}+G_{\mathbf{RR}''}^{\beta}\varepsilon^{\beta\alpha\nu}=0,\ \forall\left(\mathbf{RR}'',\alpha\beta\right)\end{gathered}\tag{A.10}$$

where $\varepsilon^{\alpha\beta\gamma}$ is the Levi-Civita symbol.

These constraints can be observed by the weighted least squares or Lagrange multiplier approach [240] in the linear fitting process. However, the weighted least squares method involves the choice of weighting factor, which is rather arbitrary, and the Lagrange multiplier approach is more complicate to implement. Here, we propose a simple embedded method, converting the constrained problem to the unconstrained one based on singular value decomposition (SVD).

For convenience, we convert both the displacement-type-force relation, Eq. (VI.5), to matrix form $\mathbf{Ax}=\mathbf{b}$ and the translational and rotational invariance constraints, Eq. (A9-A10), to $\mathbf{Cx}=0$, where $\mathbf{x}$ is a vector whose elements are the interatomic force constants ϕ, ψ, χ J and G that need to be determined, $\mathbf{A}$ and $\mathbf{C}$ are simply the coefficient matrix of the linear equation sets of the displacement-type-force relation and the constraints, and $\mathbf{b}$ is a column vector. The constrained linear fitting problem is to minimize $\left|\mathbf{Ax}-\mathbf{b}\right|^2$ under the constraints $\mathbf{Cx}=\mathbf{0}$.

Suppose $\mathbf{C}$ is an $m\times n$ matrix where m is the number of constraints and n is the number of independent interatomic force constants, the rank of $\mathbf{C}$, r, must be smaller than n. Otherwise, the vector $\mathbf{x}$ that satisfy $\mathbf{Cx}=\mathbf{0}$ has to be $\mathbf{0}$. Through SVD, we have $\mathbf{C}=\mathbf{U}\Sigma\mathbf{V}^T$, where $\mathbf{U}$ and $\mathbf{V}$ are $m\times m$ and $n\times n$ unitary matrices, $\Sigma=diag(\sigma_1,\sigma_2,\cdots,\sigma_r,0,\cdots 0)$ is an $m\times n$ rectangular diagonal matrix with r positive numbers, σ_i , on the diagonal. It can be shown that the last $n-r$ column vectors of $\mathbf{V}$ span the null space of $\mathbf{C}$. In other words, any $\mathbf{x}$ satisfying $\mathbf{Cx}=0$ must be the linear combination of $\{\mathbf{V}_{r+1},\mathbf{V}_{r+2},...,\mathbf{V}_n\}$,

$$\mathbf{x}=y_1\mathbf{V}_{r+1}+y_2\mathbf{V}_{r+2}+...+y_{n-r}\mathbf{V}_n, \tag{A.11}$$

where $\mathbf{V}_i$ is the ith column of $\mathbf{V}$ and y_i is a scalar. In matrix form, Eq. (A.11) is expressed as $\mathbf{x}=\bar{\mathbf{V}}\mathbf{y}$, where $\bar{\mathbf{V}}$ is the submatrix made up of the last $n-r$ column vectors of $\mathbf{V}$ and $\mathbf{y}$ is a

$(n-r)\times 1$ vector with y_i as its elements. Only if we can find the $\mathbf{y}^*$ which make $|\mathbf{Ax}-\mathbf{b}|^2$ minimized, $\mathbf{x}^*=\bar{\mathbf{V}}\mathbf{y}^*$ strictly satisfying all constraints and is the solution of the original constrained least-squares problem, To find the y^*, we plug in $\mathbf{x}=\bar{\mathbf{V}}\mathbf{y}$ to $\mathbf{Ax}=\mathbf{b}$ and obtain $\left(\mathbf{A}\bar{\mathbf{V}}\right)\mathbf{y}=\mathbf{b}$. The least-squares solution of $\left(\mathbf{A}\bar{\mathbf{V}}\right)\mathbf{y}=\mathbf{b}$ is $y^*=\left[\left(\mathbf{A}\bar{\mathbf{V}}\right)^T\left(\mathbf{A}\bar{\mathbf{V}}\right)\right]^{-1}\left(\mathbf{A}\bar{\mathbf{V}}\right)'\mathbf{b}$. Therefore, the extracted interatomic force constant vector is expressed as

$$\mathbf{x}^*=\bar{\mathbf{V}}\mathbf{y}^*=\bar{\mathbf{V}}\left[\left(\mathbf{A}\bar{\mathbf{V}}\right)^T\left(\mathbf{A}\bar{\mathbf{V}}\right)\right]^{-1}\left(\mathbf{A}\bar{\mathbf{V}}\right)'\mathbf{b}. \tag{A.12}$$

BIBLIOGRAPHY

[1] Goodson, K. E., and Ju, Y. S., 1999, "Heat conduction in novel electronic films," Annual Review of Materials Science, 29(1), pp. 261-293.

[2] Krishnan, S., Garimella, S. V., Chrysler, G., and Mahajan, R., 2007, "Towards a Thermal Moore's Law," IEEE Transactions on Advanced Packaging, 30(3), pp. 462-474.

[3] DiMatteo, R. S., Greiff, P., Finberg, S. L., Young-Waithe, K. A., Choy, H. K. H., Masaki, M. M., and Fonstad, C. G., 2001, "Enhanced photogeneration of carriers in a semiconductor via coupling across a nonisothermal nanoscale vacuum gap," Applied Physics Letters, 79(12), pp. 1894-1896.

[4] Tritt, T. M., 2001, Recent trends in thermoelectric materials research, Academic Press, San Diego.

[5] Chen, G., and Shakouri, A., 2002, "Heat Transfer in Nanostructures for Solid-State Energy Conversion," Journal of Heat Transfer, 124(2), pp. 242-252.

[6] Dresselhaus, M. S., Chen, G., Tang, M. Y., Yang, R. G., Lee, H., Wang, D. Z., Ren, Z. F., Fleurial, J. P., and Gogna, P., 2007, "New Directions for Low-Dimensional Thermoelectric Materials," Advanced Materials, 19(8), pp. 1043-1053.

[7] Chen, G., 2005, Nanoscale energy transport and conversion: a parallel treatment of electrons, molecules, phonons, and photons, Oxford University Press, USA.

[8] Esfarjani, K., Chen, G., and Stokes, H. T., 2011, "Heat transport in silicon from first-principles calculations," Physical Review B, 84(8), p. 085204.

[9] Minnich, A. J., Johnson, J., Schmidt, A., Esfarjani, K., Dresselhaus, M., Nelson, K. A., and Chen, G., 2011, "Thermal conductivity spectroscopy technique to measure phonon mean free paths," Physical review letters, 107(9), p. 095901.

[10] Peierls, R., 1929, "Zur kinetischen theorie der wärmeleitung in kristallen," Annalen der Physik, 395(8), pp. 1055-1101.

[11] Broido, D., Ward, A., and Mingo, N., 2005, "Lattice thermal conductivity of silicon from empirical interatomic potentials," Physical Review B, 72(1), p. 014308.

[12] Mingo, N., and Broido, D., 2005, "Length dependence of carbon nanotube thermal conductivity and the “problem of long waves”," Nano letters, 5(7), pp. 1221-1225.

[13] Nika, D., Pokatilov, E., Askerov, A., and Balandin, A., 2009, "Phonon thermal conduction in graphene: Role of Umklapp and edge roughness scattering," Physical Review B, 79(15), p. 155413.

[14] Cao, J., Yan, X., Xiao, Y., and Ding, J., 2004, "Thermal conductivity of zigzag single-walled carbon nanotubes: Role of the umklapp process," Physical Review B, 69(7), p. 073407.

[15] Ward, A., Broido, D., Stewart, D. A., and Deinzer, G., 2009, "Ab initio theory of the lattice thermal conductivity in diamond," Physical Review B, 80(12), p. 125203.

[16] Li, W., Lindsay, L., Broido, D., Stewart, D. A., and Mingo, N., 2012, "Thermal conductivity of bulk and nanowire Mg 2 Si x Sn 1− x alloys from first principles," Physical Review B, 86(17), p. 174307.

[17] Lindsay, L., Broido, D., and Reinecke, T., 2013, "Ab initio thermal transport in compound semiconductors," Physical Review B, 87(16), p. 165201.

[18] Tian, Z., Garg, J., Esfarjani, K., Shiga, T., Shiomi, J., and Chen, G., 2012, "Phonon conduction in PbSe, PbTe, and PbTe 1− x Se x from first-principles calculations," Physical Review B, 85(18), p. 184303.

[19] Garg, J., Bonini, N., Kozinsky, B., and Marzari, N., 2011, "Role of disorder and anharmonicity in the thermal conductivity of silicon-germanium alloys: A first-principles study," Physical Review Letters, 106(4), p. 045901.

[20] Fugallo, G., Lazzeri, M., Paulatto, L., and Mauri, F., 2013, "Ab initio variational approach for evaluating lattice thermal conductivity," Physical Review B, 88(4), p. 045430.

[21] Yang, R., and Chen, G., 2004, "Thermal conductivity modeling of periodic two-dimensional nanocomposites," Physical Review B, 69(19), p. 195316.

[22] Yang, R., Chen, G., and Dresselhaus, M. S., 2005, "Thermal conductivity of simple and tubular nanowire composites in the longitudinal direction," Physical Review B, 72(12), p. 125418.

[23] Jeng, M.-S., Yang, R., Song, D., and Chen, G., 2008, "Modeling the thermal conductivity and phonon transport in nanoparticle composites using Monte Carlo simulation," Journal of Heat Transfer, 130(4), p. 042410.

[24] Swartz, E. T., and Pohl, R. O., 1989, "Thermal boundary resistance," Reviews of Modern Physics, 61(3), p. 605.

[25] Schelling, P., Phillpot, S., and Keblinski, P., 2002, "Phonon wave-packet dynamics at semiconductor interfaces by molecular-dynamics simulation," Applied Physics Letters, 80(14), pp. 2484-2486.

[26] Zhao, H., and Freund, J., 2005, "Lattice-dynamical calculation of phonon scattering at ideal Si–Ge interfaces," Journal of Applied Physics, 97(2), p. 024903.

[27] Mingo, N., and Yang, L., 2003, "Phonon transport in nanowires coated with an amorphous material: An atomistic Green's function approach," Physical Review B, 68(24), p. 245406.

[28] Tian, Z., Esfarjani, K., and Chen, G., 2012, "Enhancing phonon transmission across a Si/Ge interface by atomic roughness: First-principles study with the Green's function method," Physical Review B, 86(23), p. 235304.

[29] Volz, S. G., and Chen, G., 1999, "Molecular dynamics simulation of thermal conductivity of silicon nanowires," Applied Physics Letters, 75(14), pp. 2056-2058.

[30] Berber, S., Kwon, Y.-K., and Tomanek, D., 2000, "Unusually high thermal conductivity of carbon nanotubes," Physical review letters, 84(20), p. 4613.

[31] Lukes, J. R., Li, D., Liang, X.-G., and Tien, C.-L., 2000, "Molecular dynamics study of solid thin-film thermal conductivity," Journal of heat transfer, 122(3), pp. 536-543.

[32] Porter, L. J., Justo, J. F., and Yip, S., 1997, "The importance of Grüneisen parameters in developing interatomic potentials," Journal of Applied Physics, 82(11), pp. 5378-5381.

[33] Stackhouse, S., Stixrude, L., and Karki, B. B., 2010, "Thermal conductivity of periclase (MgO) from first principles," Physical review letters, 104(20), p. 208501.

[34] Sellan, D., Landry, E., Turney, J., McGaughey, A., and Amon, C., 2010, "Size effects in molecular dynamics thermal conductivity predictions," Physical Review B, 81(21), p. 214305.

[35] Novoselov, K. S., Geim, A. K., Morozov, S., Jiang, D., Zhang, Y., Dubonos, S., Grigorieva, I., and Firsov, A., 2004, "Electric field effect in atomically thin carbon films," Science, 306(5696), pp. 666-669.

[36] Novoselov, K. S., Geim, A. K., Morozov, S. V., Jiang, D., Katsnelson, M. I., Grigorieva, I. V., Dubonos, S. V., and Firsov, A. A., 2005, "Two-dimensional gas of massless Dirac fermions in graphene," Nature, 438(7065), pp. 197-200.

[37] Geim, A. K., and Novoselov, K. S., 2007, "The rise of graphene," Nature materials, 6(3), pp. 183-191.

[38] Neto, A. H. C., Guinea, F., Peres, N. M. R., Novoselov, K. S., and Geim, A. K., 2009, "The electronic properties of graphene," Rev. Mod. Phys., 81(1), p. 109.

[39] Xu, M., Liang, T., Shi, M., and Chen, H., 2013, "Graphene-like two-dimensional materials," Chemical reviews, 113(5), pp. 3766-3798.

[40] Butler, S. Z., Hollen, S. M., Cao, L., Cui, Y., Gupta, J. A., Gutierrez, H. R., Heinz, T. F., Hong, S. S., Huang, J., and Ismach, A. F., 2013, "Progress, challenges, and opportunities in two-dimensional materials beyond graphene," ACS nano, 7(4), pp. 2898-2926.

[41] Wang, Q. H., Kalantar-Zadeh, K., Kis, A., Coleman, J. N., and Strano, M. S., 2012, "Electronics and optoelectronics of two-dimensional transition metal dichalcogenides," Nature nanotechnology, 7(11), pp. 699-712.

[42] Chhowalla, M., Shin, H. S., Eda, G., Li, L.-J., Loh, K. P., and Zhang, H., 2013, "The chemistry of two-dimensional layered transition metal dichalcogenide nanosheets," Nature chemistry, 5(4), pp. 263-275.

[43] Ju, Y., and Goodson, K., 1999, "Phonon scattering in silicon films with thickness of order 100 nm," Applied Physics Letters, 74(20), pp. 3005-3007.

[44] Li, D., Wu, Y., Kim, P., Shi, L., Yang, P., and Majumdar, A., 2003, "Thermal conductivity of individual silicon nanowires," Applied Physics Letters, 83(14), pp. 2934-2936.

[45] Hochbaum, A. I., Chen, R., Delgado, R. D., Liang, W., Garnett, E. C., Najarian, M., Majumdar, A., and Yang, P., 2008, "Enhanced thermoelectric performance of rough silicon nanowires," Nature, 451(7175), pp. 163-167.

[46] Lee, S., Cahill, D. G., and Venkatasubramanian, R., 1997, "Thermal conductivity of Si {endash} Ge superlattices," Applied physics letters, 70(22).

[47] Yang, B., and Chen, G., 2003, "Partially coherent phonon heat conduction in superlattices," Physical Review B, 67(19), p. 195311.

[48] Poudel, B., Hao, Q., Ma, Y., Lan, Y., Minnich, A., Yu, B., Yan, X., Wang, D., Muto, A., and Vashaee, D., 2008, "High-thermoelectric performance of nanostructured bismuth antimony telluride bulk alloys," Science, 320(5876), pp. 634-638.

[49] Kim, W., Zide, J., Gossard, A., Klenov, D., Stemmer, S., Shakouri, A., and Majumdar, A., 2006, "Thermal conductivity reduction and thermoelectric figure of merit increase by embedding nanoparticles in crystalline semiconductors," Phys. Rev. Lett., 96(4), p. 045901.

[50] Luckyanova, M. N., Garg, J., Esfarjani, K., Jandl, A., Bulsara, M. T., Schmidt, A. J., Minnich, A. J., Chen, S., Dresselhaus, M. S., and Ren, Z., 2012, "Coherent phonon heat conduction in superlattices," Science, 338(6109), pp. 936-939.

[51] Dresselhaus, M. S., Chen, G., Tang, M. Y., Yang, R., Lee, H., Wang, D., Ren, Z., Fleurial, J. P., and Gogna, P., 2007, "New Directions for Low ‐ Dimensional Thermoelectric Materials," Advanced Materials, 19(8), pp. 1043-1053.

[52] Kim, W., Wang, R., and Majumdar, A., 2007, "Nanostructuring expands thermal limits," Nano Today, 2(1), pp. 40-47.

[53] Clarke, D. R., Oechsner, M., and Padture, N. P., 2012, "Thermal-barrier coatings for more efficient gas-turbine engines," MRS Bull., 37(10), pp. 891-898.

[54] Balandin, A. A., 2011, "Thermal properties of graphene and nanostructured carbon materials," Nature materials, 10(8), pp. 569-581.

[55] Sadeghi, M. M., Pettes, M. T., and Shi, L., 2012, "Thermal transport in graphene," Solid State Commun., 152(15), pp. 1321-1330.

[56] Pop, E., Varshney, V., and Roy, A. K., 2012, "Thermal properties of graphene: Fundamentals and applications," MRS bulletin, 37(12), pp. 1273-1281.

[57] Nika, D. L., and Balandin, A. A., 2012, "Two-dimensional phonon transport in graphene," Journal of Physics: Condensed Matter, 24(23), p. 233203.

[58] Goldsmid, H., and Douglas, R., 1954, "The use of semiconductors in thermoelectric refrigeration," British Journal of Applied Physics, 5(11), p. 386.

[59] Ioffe, A. F., 1957, Semiconductor thermoelements, and Thermoelectric cooling, Infosearch, ltd.

[60] Zhao, L.-D., Lo, S.-H., Zhang, Y., Sun, H., Tan, G., Uher, C., Wolverton, C., Dravid, V. P., and Kanatzidis, M. G., 2014, "Ultralow thermal conductivity and high thermoelectric figure of merit in SnSe crystals," Nature, 508(7496), pp. 373-377.

[61] Venkatasubramanian, R., Siivola, E., Colpitts, T., and O'quinn, B., 2001, "Thin-film thermoelectric devices with high room-temperature figures of merit," Nature, 413(6856), pp. 597-602.

[62] Neto, A. C., Guinea, F., Peres, N., Novoselov, K. S., and Geim, A. K., 2009, "The electronic properties of graphene," Reviews of modern physics, 81(1), p. 109.

[63] Geim, A. K., 2009, "Graphene: status and prospects," science, 324(5934), pp. 1530-1534.

[64] Singh, D., Murthy, J. Y., and Fisher, T. S., 2011, "Mechanism of thermal conductivity reduction in few-layer graphene," Journal of Applied Physics, 110(4), pp. 044317-044317-044318.

[65] Pereira, L. F. C., and Donadio, D., 2013, "Divergence of the thermal conductivity in uniaxially strained graphene," Physical Review B, 87(12), p. 125424.

[66] Bonini, N., Garg, J., and Marzari, N., 2012, "Acoustic phonon lifetimes and thermal transport in free-standing and strained graphene," Nano letters, 12(6), pp. 2673-2678.

[67] Lindsay, L., Broido, D., and Mingo, N., 2010, "Flexural phonons and thermal transport in graphene," Physical Review B, 82(11), p. 115427.

[68] Li, X., Maute, K., Dunn, M. L., and Yang, R., 2010, "Strain effects on the thermal conductivity of nanostructures," Physical Review B, 81(24), p. 245318.

[69] Shahil, K. M., and Balandin, A. A., 2012, "Graphene–multilayer graphene nanocomposites as highly efficient thermal interface materials," Nano letters, 12(2), pp. 861-867.

[70] Goyal, V., and Balandin, A. A., 2012, "Thermal properties of the hybrid graphene-metal nano-micro-composites: applications in thermal interface materials," Applied Physics Letters, 100(7), p. 073113.

[71] Goli, P., Legedza, S., Dhar, A., Salgado, R., Renteria, J., and Balandin, A. A., 2014, "Graphene-enhanced hybrid phase change materials for thermal management of Li-ion batteries," Journal of Power Sources, 248, pp. 37-43.

[72] Yan, Z., Liu, G., Khan, J. M., and Balandin, A. A., 2012, "Graphene quilts for thermal management of high-power GaN transistors," Nature communications, 3, p. 827.

[73] Malekpour, H., Chang, K.-H., Chen, J.-C., Lu, C.-Y., Nika, D., Novoselov, K. S., and Balandin, A. A., 2014, "Thermal Conductivity of Graphene Laminate," Nano letters, 14(9), pp. 5155-5161.

[74] Butler, S. Z., Hollen, S. M., Cao, L., Cui, Y., Gupta, J. A., Gutiérrez, H. R., Heinz, T. F., Hong, S. S., Huang, J., and Ismach, A. F., 2013, "Progress, Challenges, and Opportunities in Two-Dimensional Materials Beyond Graphene," ACS nano, 7(4), pp. 2898-2926.

[75] Cahangirov, S., Topsakal, M., Aktürk, E., Şahin, H., and Ciraci, S., 2009, "Two-and one-dimensional honeycomb structures of silicon and germanium," Physical Review Letters, 102(23), p. 236804.

[76] Fleurence, A., Friedlein, R., Ozaki, T., Kawai, H., Wang, Y., and Yamada-Takamura, Y., 2012, "Experimental evidence for epitaxial silicene on diboride thin films," Physical Review Letters, 108(24), p. 245501.

[77] Vogt, P., De Padova, P., Quaresima, C., Avila, J., Frantzeskakis, E., Asensio, M. C., Resta, A., Ealet, B., and Le Lay, G., 2012, "Silicene: Compelling experimental evidence for graphenelike two-dimensional silicon," Physical Review Letters, 108(15), p. 155501.

[78] Wang, B., Wu, J., Gu, X., Yin, H., Wei, Y., Yang, R., and Dresselhaus, M., 2014, "Stable planar single-layer hexagonal silicene under tensile strain and its anomalous Poisson's ratio," Applied Physics Letters, 104(8), p. 081902.

[79] Chen, L., Liu, C.-C., Feng, B., He, X., Cheng, P., Ding, Z., Meng, S., Yao, Y., and Wu, K., 2012, "Evidence for Dirac Fermions in a honeycomb lattice based on silicon," Physical Review Letters, 109(5), p. 056804.

[80] Drummond, N., Zolyomi, V., and Fal'Ko, V., 2012, "Electrically tunable band gap in silicene," Physical Review B, 85(7), p. 075423.

[81] Ni, Z., Liu, Q., Tang, K., Zheng, J., Zhou, J., Qin, R., Gao, Z., Yu, D., and Lu, J., 2011, "Tunable bandgap in silicene and germanene," Nano letters, 12(1), pp. 113-118.

[82] Zhang, X., Xie, H., Hu, M., Bao, H., Yue, S., Qin, G., and Su, G., 2014, "Thermal conductivity of silicene calculated using an optimized Stillinger-Weber potential," Physical Review B, 89(5), p. 054310.

[83] Hu, M., Zhang, X., and Poulikakos, D., 2013, "Anomalous thermal response of silicene to uniaxial stretching," Physical Review B, 87(19), p. 195417.

[84] Xu, X., Pereira, L. F. C., Wang, Y., Wu, J., Zhang, K., Zhao, X., Bae, S., Bui, C. T., Xie, R., Thong, J. T. L., Hong, B. H., Loh, K. P., Donadio, D., Li, B., and Özyilmaz, B., 2014, "Length-dependent thermal conductivity in suspended single layer graphene," Nature Communications, 5, p. 3689.

[85] Pei, Q.-X., Zhang, Y.-W., Sha, Z.-D., and Shenoy, V. B., 2013, "Tuning the thermal conductivity of silicene with tensile strain and isotopic doping: A molecular dynamics study," Journal of Applied Physics, 114(3), p. 033526.

[86] Ng, T. Y., Yeo, J., and Liu, Z., 2013, "Molecular dynamics simulation of the thermal conductivity of shorts strips of graphene and silicene: a comparative study," International Journal of Mechanics and Materials in Design, 9(2), pp. 105-114.

[87] Luo, T., Garg, J., Shiomi, J., Esfarjani, K., and Chen, G., 2013, "Gallium arsenide thermal conductivity and optical phonon relaxation times from first-principles calculations," EPL (Europhysics Letters), 101(1), p. 16001.

[88] Tian, Z., Garg, J., Esfarjani, K., Shiga, T., Shiomi, J., and Chen, G., 2012, "Phonon conduction in PbSe, PbTe, and PbTe_ {1− x} Se_ {x} from first-principles calculations," Physical Review B, 85(18), p. 184303.

[89] Shiomi, J., Esfarjani, K., and Chen, G., 2011, "Thermal conductivity of half-Heusler compounds from first-principles calculations," Physical Review B, 84(10), p. 104302.

[90] Li, W., Lindsay, L., Broido, D., Stewart, D. A., and Mingo, N., 2012, "Thermal conductivity of bulk and nanowire Mg_ {2} Si_ {x} Sn_ {1− x} alloys from first principles," Physical Review B, 86(17), p. 174307.

[91] Garg, J., Bonini, N., and Marzari, N., 2011, "High Thermal Conductivity in Short-Period Superlattices," Nano letters, 11(12), pp. 5135-5141.

[92] Garg, J., and Chen, G., 2013, "Minimum thermal conductivity in superlattices: A first-principles formalism," Physical Review B, 87(14), p. 140302.

[93] Li, W., Mingo, N., Lindsay, L., Broido, D., Stewart, D., and Katcho, N., 2012, "Thermal conductivity of diamond nanowires from first principles," Physical Review B, 85(19), p. 195436.

[94] Paulatto, L., Mauri, F., and Lazzeri, M., 2013, "Anharmonic properties from a generalized third-order ab initio approach: Theory and applications to graphite and graphene," Physical Review B, 87(21), p. 214303.

[95] Tang, X., and Fultz, B., 2011, "First-principles study of phonon linewidths in noble metals," Physical Review B, 84(5), p. 054303.

[96] Srivastava, G. P., 1990, The physics of phonons, CRC Press.

[97] Giannozzi, P., Baroni, S., Bonini, N., Calandra, M., Car, R., Cavazzoni, C., Ceresoli, D., Chiarotti, G. L., Cococcioni, M., and Dabo, I., 2009, "QUANTUM ESPRESSO: a modular and open-source software project for quantum simulations of materials," Journal of Physics: Condensed Matter, 21(39), p. 395502.

[98] McGaughey, A. J., and Jain, A., 2012, "Nanostructure thermal conductivity prediction by Monte Carlo sampling of phonon free paths," Applied Physics Letters, 100(6), p. 061911.

[99] Ziman, J. M., 2001, Electrons and phonons: the theory of transport phenomena in solids, Oxford University Press.

[100] Yates, J. R., Wang, X., Vanderbilt, D., and Souza, I., 2007, "Spectral and Fermi surface properties from Wannier interpolation," Physical Review B, 75(19), p. 195121.

[101] Van der Vorst, H. A., 1992, "Bi-CGSTAB: A fast and smoothly converging variant of Bi-CG for the solution of nonsymmetric linear systems," SIAM J. Sci. Comput., 13(2), pp. 631-644.

[102] Omini, M., and Sparavigna, A., 1996, "Beyond the isotropic-model approximation in the theory of thermal conductivity," Physical Review B, 53(14), p. 9064.

[103] Chernatynskiy, A., and Phillpot, S. R., 2010, "Evaluation of computational techniques for solving the Boltzmann transport equation for lattice thermal conductivity calculations," Physical Review B, 82(13), p. 134301.

[104] Scalise, E., Houssa, M., Pourtois, G., van den Broek, B., Afanas'ev, V., and Stesmans, A., 2013, "Vibrational properties of silicene and germanene," Nano Research, 6(1), pp. 19-28.

[105] Ferrari, A., Meyer, J., Scardaci, V., Casiraghi, C., Lazzeri, M., Mauri, F., Piscanec, S., Jiang, D., Novoselov, K., and Roth, S., 2006, "Raman spectrum of graphene and graphene layers," Physical Review Letters, 97(18), p. 187401.

[106] Şahin, H., Cahangirov, S., Topsakal, M., Bekaroglu, E., Akturk, E., Senger, R. T., and Ciraci, S., 2009, "Monolayer honeycomb structures of group-IV elements and III-V binary compounds: First-principles calculations," Physical Review B, 80(15), p. 155453.

[107] Li, X., Mullen, J. T., Jin, Z., Borysenko, K. M., Nardelli, M. B., and Kim, K. W., 2013, "Intrinsic electrical transport properties of monolayer silicene and MoS 2 from first principles," Physical Review B, 87(11), p. 115418.

[108] Zabel, H., 2001, "Phonons in layered compounds," Journal of Physics: Condensed Matter, 13(34), p. 7679.

[109] Li, X., Mullen, J. T., Jin, Z., Borysenko, K. M., Nardelli, M. B., and Kim, K. W., 2013, "Intrinsic electrical transport properties of monolayer silicene and MoS_ {2} from first principles," Physical Review B, 87(11), p. 115418.

[110] Mariani, E., and von Oppen, F., 2008, "Flexural phonons in free-standing graphene," Physical Review Letters, 100(7), p. 076801.

[111] Lindsay, L., and Broido, D., 2010, "Optimized Tersoff and Brenner empirical potential parameters for lattice dynamics and phonon thermal transport in carbon nanotubes and graphene," Physical Review B, 81(20), p. 205441.

[112] Chen, S., Wu, Q., Mishra, C., Kang, J., Zhang, H., Cho, K., Cai, W., Balandin, A. A., and Ruoff, R. S., 2012, "Thermal conductivity of isotopically modified graphene," Nature materials, 11(3), pp. 203-207.

[113] Chen, S., Moore, A. L., Cai, W., Suk, J. W., An, J., Mishra, C., Amos, C., Magnuson, C. W., Kang, J., and Shi, L., 2010, "Raman measurements of thermal transport in suspended monolayer graphene of variable sizes in vacuum and gaseous environments," ACS nano, 5(1), pp. 321-328.

[114] Lee, J.-U., Yoon, D., Kim, H., Lee, S. W., and Cheong, H., 2011, "Thermal conductivity of suspended pristine graphene measured by Raman spectroscopy," Physical Review B, 83(8), p. 081419.

[115] Faugeras, C., Faugeras, B., Orlita, M., Potemski, M., Nair, R. R., and Geim, A., 2010, "Thermal conductivity of graphene in corbino membrane geometry," ACS nano, 4(4), pp. 1889-1892.

[116] Liu, W., and Asheghi, M., 2006, "Thermal conductivity measurements of ultra-thin single crystal silicon layers," Journal of heat transfer, 128(1), pp. 75-83.

[117] Stillinger, F. H., and Weber, T. A., 1985, "Computer simulation of local order in condensed phases of silicon," Physical Review B, 31(8), p. 5262.

[118] Cahill, D. G., Braun, P. V., Chen, G., Clarke, D. R., Fan, S., Goodson, K. E., Keblinski, P., King, W. P., Mahan, G. D., and Majumdar, A., 2014, "Nanoscale thermal transport. II. 2003–2012," Applied Physics Reviews, 1(1), p. 011305.

[119] Xie, H., Hu, M., and Bao, H., 2014, "Thermal conductivity of silicene from first-principles," Applied Physics Letters, 104(13), p. 131906.

[120] Balkanski, M., Wallis, R., and Haro, E., 1983, "Anharmonic effects in light scattering due to optical phonons in silicon," Physical Review B, 28(4), p. 1928.

[121] Ecsedy, D., and Klemens, P., 1977, "Thermal resistivity of die ectric crystals due to four-phonon processes and optical modes," Physical Review B, 15(12), p. 5957.

[122] Mak, K. F., Lee, C., Hone, J., Shan, J., and Heinz, T. F., 2010, "Atomically thin MoS 2: a new direct-gap semiconductor," Physical review letters, 105(13), p. 136805.

[123] Splendiani, A., Sun, L., Zhang, Y., Li, T., Kim, J., Chim, C.-Y., Galli, G., and Wang, F., 2010, "Emerging photoluminescence in monolayer MoS2," Nano letters, 10(4), pp. 1271-1275.

[124] Ding, Y., Wang, Y., Ni, J., Shi, L., Shi, S., and Tang, W., 2011, "First principles study of structural, vibrational and electronic properties of graphene-like MX< sub> 2</sub>(M= Mo, Nb, W, Ta; X= S, Se, Te) monolayers," Physica B: Condensed Matter, 406(11), pp. 2254-2260.

[125] Yun, W. S., Han, S., Hong, S. C., Kim, I. G., and Lee, J., 2012, "Thickness and strain effects on electronic structures of transition metal dichalcogenides: 2H-M X 2 semiconductors (M= Mo, W; X= S, Se, Te)," Physical Review B, 85(3), p. 033305.

[126] Gutiérrez, H. R., Perea-López, N., Elías, A. L., Berkdemir, A., Wang, B., Lv, R., López-Urías, F., Crespi, V. H., Terrones, H., and Terrones, M., 2012, "Extraordinary room-temperature photoluminescence in triangular WS2 monolayers," Nano letters, 13(8), pp. 3447-3454.

[127] Lebègue, S., Björkman, T., Klintenberg, M., Nieminen, R., and Eriksson, O., 2013, "Two-dimensional materials from data filtering and ab initio calculations," Physical Review X, 3(3), p. 031002.

[128] Jiang, H., 2011, "Structural and electronic properties of ZrX2 and HfX2 (X= S and Se) from first principles calculations," Journal of chemical physics, 134(20), p. 204705.

[129] Li, Y., Kang, J., and Li, J., 2014, "Indirect-to-direct band gap transition of the ZrS 2 monolayer by strain: first-principles calculations," RSC Advances, 4(15), pp. 7396-7401.

[130] Muratore, C., Varshney, V., Gengler, J., Hu, J., Bultman, J., Smith, T., Shamberger, P., Qiu, B., Ruan, X., and Roy, A., 2013, "Cross-plane thermal properties of transition metal dichalcogenides," Applied Physics Letters, 102(8), p. 081604.

[131] Huang, W., Da, H., and Liang, G., 2013, "Thermoelectric performance of MX2 (M= Mo, W; X= S, Se) monolayers," Journal of Applied Physics, 113(10), p. 104304.

[132] Lee, C., Hong, J., Whangbo, M.-H., and Shim, J. H., 2013, "Enhancing the thermoelectric properties of layered transition-metal dichalcogenides 2H-MQ2 (M= Mo, W; Q= S, Se, Te) by layer mixing: Density functional investigation," Chemistry of Materials, 25(18), pp. 3745-3752.

[133] Huang, W., Luo, X., Gan, C. K., Quek, S. Y., and Liang, G., 2014, "Theoretical study of thermoelectric properties of few-layer MoS 2 and WSe 2," Physical Chemistry Chemical Physics, 16(22), pp. 10866-10874.

[134] Sahoo, S., Gaur, A. P., Ahmadi, M., Guinel, M. J.-F., and Katiyar, R. S., 2013, "Temperature-Dependent Raman Studies and Thermal Conductivity of Few-Layer MoS2," Journal of Physical Chemistry C, 117(17), pp. 9042-9047.

[135] Yan, R., Simpson, J. R., Bertolazzi, S., Brivio, J., Watson, M., Wu, X., Kis, A., Luo, T., Hight Walker, A. R., and Xing, H. G., 2014, "Thermal conductivity of monolayer molybdenum disulfide obtained from temperature-dependent Raman spectroscopy," ACS nano, 8(1), pp. 986-993.

[136] Jo, I., Pettes, M. T., Ou, E., Wu, W., and Shi, L., 2014, "Basal-plane thermal conductivity of few-layer molybdenum disulfide," Applied Physics Letters, 104(20), p. 201902.

[137] Cai, Y., Lan, J., Zhang, G., and Zhang, Y.-W., 2014, "Lattice vibrational modes and phonon thermal conductivity of monolayer MoS 2," Physical Review B, 89(3), p. 035438.

[138] Li, W., Carrete, J., and Mingo, N., 2013, "Thermal conductivity and phonon linewidths of monolayer MoS2 from first principles," Appl. Phys. Lett., 103(25), p. 253103.

[139] Liu, X., Zhang, G., Pei, Q.-X., and Zhang, Y.-W., 2013, "Phonon thermal conductivity of monolayer MoS2 sheet and nanoribbons," Applied Physics Letters, 103(13), p. 133113.

[140] Jiang, J.-W., Park, H. S., and Rabczuk, T., 2013, "Molecular dynamics simulations of single-layer molybdenum disulphide (MoS2): Stillinger-Weber parametrization, mechanical properties, and thermal conductivity," Journal of Applied Physics, 114(6), p. 064307.

[141] Jiang, J.-W., Zhuang, X., and Rabczuk, T., 2013, "Orientation Dependent Thermal Conductance in Single-Layer MoS2," Scientific reports, 3.

[142] Muratore, C., Varshney, V., Gengler, J. J., Hu, J., Bultman, J. E., Roy, A. K., Farmer, B. L., and Voevodin, A. A., 2014, "Thermal anisotropy in nano-crystalline MoS 2 thin films," Physical Chemistry Chemical Physics, 16(3), pp. 1008-1014.

[143] Gu, X., and Yang, R., 2015, "Phonon transport and thermal conductivity in two-dimensional materials," arXiv preprint arXiv:1509.07762.

[144] Ghosh, S., Bao, W., Nika, D. L., Subrina, S., Pokatilov, E. P., Lau, C. N., and Balandin, A. A., 2010, "Dimensional crossover of thermal transport in few-layer graphene," Nature materials, 9(7), pp. 555-558.

[145] Lindsay, L., Broido, D., and Mingo, N., 2011, "Flexural phonons and thermal transport in multilayer graphene and graphite," Physical Review B, 83(23), p. 235428.

[146] Wei, Z., Ni, Z., Bi, K., Chen, M., and Chen, Y., 2011, "In-plane lattice thermal conductivities of multilayer graphene films," Carbon, 49(8), pp. 2653-2658.

[147] Pettes, M. T., Maassen, J., Jo, I., Lundstrom, M. S., and Shi, L., 2013, "Effects of surface band bending and scattering on thermoelectric transport in suspended bismuth telluride nanoplates," Nano letters, 13(11), pp. 5316-5322.

[148] Qiu, B., and Ruan, X., 2010, "Thermal conductivity prediction and analysis of few-quintuple Bi2Te3 thin films: A molecular dynamics study," Applied Physics Letters, 97(18), p. 183107.

[149] Yan, Z., Jiang, C., Pope, T., Tsang, C., Stickney, J., Goli, P., Renteria, J., Salguero, T., and Balandin, A., 2013, "Phonon and thermal properties of exfoliated TaSe2 thin films," Journal of Applied Physics, 114(20), p. 204301.

[150] Zhang, X., Sun, D., Li, Y., Lee, G. H., Cui, X., Chenet, D., You, Y., Heinz, T., and Hone, J., 2015, "Measurement of lateral and interfacial thermal conductivity of single-and bi-layer MoS2 and MoSe2 using refined optothermal Raman technique," ACS Applied Materials & Interfaces.

[151] Sahoo, S., Gaur, A. P., Ahmadi, M., Guinel, M. J.-F., and Katiyar, R. S., 2013, "Temperature-dependent Raman studies and thermal conductivity of few-layer MoS2," The Journal of Physical Chemistry C, 117(17), pp. 9042-9047.

[152] Liu, J., Choi, G.-M., and Cahill, D. G., 2014, "Measurement of the anisotropic thermal conductivity of molybdenum disulfide by the time-resolved magneto-optic Kerr effect," Journal of Applied Physics, 116(23), p. 233107.

[153] Ding, Z., Jiang, J.-W., Pei, Q.-X., and Zhang, Y.-W., 2015, "In-plane and cross-plane thermal conductivities of molybdenum disulfide," Nanotechnology, 26(6), p. 065703.

[154] Broido, D., Malorny, M., Birner, G., Mingo, N., and Stewart, D., 2007, "Intrinsic lattice thermal conductivity of semiconductors from first principles," Applied Physics Letters, 91(23), p. 231922.

[155] Gu, X., and Yang, R., 2015, "First-principles prediction of phononic thermal conductivity of silicene: A comparison with graphene," Journal of Applied Physics, 117(2), p. 025102.

[156] Gu, X., and Yang, R., 2014, "Phonon transport in single-layer transition metal dichalcogenides: A first-principles study," Appl. Phys. Lett., 105(13), p. 131903.

[157] Wakabayashi, N., Smith, H., and Nicklow, R., 1975, "Lattice dynamics of hexagonal Mo S 2 studied by neutron scattering," Physical Review B, 12(2), p. 659.

[158] Lee, S., Esfarjani, K., Mendoza, J., Dresselhaus, M. S., and Chen, G., 2014, "Lattice thermal conductivity of Bi, Sb, and Bi-Sb alloy from first principles," Physical Review B, 89(8), p. 085206.

[159] Barron, T. H. K., and Klein, M. L., 1974, Dynamical Properties of Solids, G. K. Horton, and A. A. Maradudin, eds., North-Holland, Amsterdam, p. 391.

[160] Gordon, R., Yang, D., Crozier, E., Jiang, D., and Frindt, R., 2002, "Structures of exfoliated single layers of WS 2, MoS 2, and MoSe 2 in aqueous suspension," Physical Review B, 65(12), p. 125407.

[161] Böker, T., Severin, R., Müller, A., Janowitz, C., Manzke, R., Voß, D., Krüger, P., Mazur, A., and Pollmann, J., 2001, "Band structure of MoS 2, MoSe 2, and α-MoTe 2: Angle-resolved photoelectron spectroscopy and ab initio calculations," Physical Review B, 64(23), p. 235305.

[162] Schutte, W., De Boer, J., and Jellinek, F., 1987, "Crystal structures of tungsten disulfide and diselenide," Journal of Solid State Chemistry, 70(2), pp. 207-209.

[163] Greenaway, D. L., and Nitsche, R., 1965, "Preparation and optical properties of group IV–VI< sub> 2</sub> chalcogenides having the CdI< sub> 2</sub> structure," Journal of Physics and Chemistry of Solids, 26(9), pp. 1445-1458.

[164] Lee, S., Esfarjani, K., Luo, T., Zhou, J., Tian, Z., and Chen, G., 2014, "Resonant bonding leads to low lattice thermal conductivity," Nature communications, 5.

[165] Lindsay, L., Broido, D., and Reinecke, T., 2013, "First-principles determination of ultrahigh thermal conductivity of boron arsenide: a competitor for diamond?," Physical Review Letters, 111(2), p. 025901.

[166] Wilson, R., and Cahill, D. G., 2014, "Anisotropic failure of Fourier theory in time-domain thermoreflectance experiments," Nature communications, 5.

[167] Yan, J.-A., Ruan, W., and Chou, M., 2008, "Phonon dispersions and vibrational properties of monolayer, bilayer, and trilayer graphene: Density-functional perturbation theory," Physical review B, 77(12), p. 125401.

[168] Christensen, M., Abrahamsen, A. B., Christensen, N. B., Juranyi, F., Andersen, N. H., Lefmann, K., Andreasson, J., Bahl, C. R., and Iversen, B. B., 2008, "Avoided crossing of rattler modes in thermoelectric materials," Nature materials, 7(10), pp. 811-815.

[169] Dong, J., Sankey, O. F., and Myles, C. W., 2001, "Theoretical study of the lattice thermal conductivity in Ge framework semiconductors," Physical review letters, 86(11), p. 2361.

[170] Wang, H., Yuan, H., Hong, S. S., Li, Y., and Cui, Y., 2015, "Physical and chemical tuning of two-dimensional transition metal dichalcogenides," Chem. Soc. Rev., 44(9), pp. 2664-2680.

[171] Radisavljevic, B., Radenovic, A., Brivio, J., Giacometti, V., and Kis, A., 2011, "Single-layer MoS2 transistors," Nat. Nanotechnol., 6(3), pp. 147-150.

[172] Kong, D., Wang, H., Cha, J. J., Pasta, M., Koski, K. J., Yao, J., and Cui, Y., 2013, "Synthesis of MoS2 and MoSe2 films with vertically aligned layers," Nano Lett., 13(3), pp. 1341-1347.

[173] Wan, C., Gu, X., Dang, F., Itoh, T., Wang, Y., Sasaki, H., Kondo, M., Koga, K., Yabuki, K., and Snyder, G. J., 2015, "Flexible n-type thermoelectric materials by organic intercalation of layered transition metal dichalcogenide TiS2," Nat. Mater., 14(6), pp. 622-627.

[174] Dresselhaus, M. S., 2013, Intercalation in layered materials, Springer.

[175] Gong, Y., Lin, J., Wang, X., Shi, G., Lei, S., Lin, Z., Zou, X., Ye, G., Vajtai, R., and Yakobson, B. I., 2014, "Vertical and in-plane heterostructures from WS2/MoS2 monolayers," Nat. Mater., 13, p. 1135.

[176] Huang, C., Wu, S., Sanchez, A. M., Peters, J. J., Beanland, R., Ross, J. S., Rivera, P., Yao, W., Cobden, D. H., and Xu, X., 2014, "Lateral heterojunctions within monolayer MoSe2–WSe2 semiconductors," Nat. Mater., 13(12), pp. 1096-1101.

[177] Li, M.-Y., Shi, Y., Cheng, C.-C., Lu, L.-S., Lin, Y.-C., Tang, H.-L., Tsai, M.-L., Chu, C.-W., Wei, K.-H., and He, J.-H., 2015, "Epitaxial growth of a monolayer WSe2-MoS2 lateral pn junction with an atomically sharp interface," Science, 349(6247), pp. 524-528.

[178] Chen, Y., Xi, J., Dumcenco, D. O., Liu, Z., Suenaga, K., Wang, D., Shuai, Z., Huang, Y.-S., and Xie, L., 2013, "Tunable band gap photoluminescence from atomically thin transition-metal dichalcogenide alloys," ACS Nano, 7(5), pp. 4610-4616.

[179] Mann, J., Ma, Q., Odenthal, P. M., Isarraraz, M., Le, D., Preciado, E., Barroso, D., Yamaguchi, K., von Son Palacio, G., and Nguyen, A., 2014, "2‐Dimensional Transition Metal

Dichalcogenides with Tunable Direct Band Gaps: MoS2 (1 − x) Se2x Monolayers," Adv. Mater., 26(9), pp. 1399-1404.

[180] Gu, X., Li, B., and Yang, R., 2016, "Layer thickness-dependent phonon properties and thermal conductivity of MoS2," J. Appl. Phys., 119(8), p. 085106.

[181] Zhang, X., Sun, D., Li, Y., Lee, G.-H., Cui, X., Chenet, D., You, Y., Heinz, T. F., and Hone, J. C., 2015, "Measurement of Lateral and Interfacial Thermal Conductivity of Single-and Bilayer MoS2 and MoSe2 Using Refined Optothermal Raman Technique," ACS Appl. Mater. Interfaces, 7(46), pp. 25923-25929.

[182] Padture, N. P., Gell, M., and Jordan, E. H., 2002, "Thermal barrier coatings for gas-turbine engine applications," Science, 296(5566), pp. 280-284.

[183] Kayyalha, M., Shi, L., and Chen, Y. P., 2015, "Gate-Tunable and Thickness-dependent Electronic and Thermoelectric Transport in few-layer MoS2," arXiv preprint arXiv:1505.05891.

[184] Hippalgaonkar, K., Wang, Y., Ye, Y., Zhu, H., Wang, Y., Moore, J., and Zhang, X., 2015, "Record High Thermoelectric Powerfactor in Single and Few-Layer MoS $ _2$," arXiv preprint arXiv:1505.06779.

[185] Mingo, N., Hauser, D., Kobayashi, N., Plissonnier, M., and Shakouri, A., 2009, "“Nanoparticle-in-Alloy” approach to efficient thermoelectrics: silicides in SiGe," Nano letters, 9(2), pp. 711-715.

[186] Economou, E. N., 1984, Green's functions in quantum physics, Springer.

[187] Mingo, N., Esfarjani, K., Broido, D., and Stewart, D., 2010, "Cluster scattering effects on phonon conduction in graphene," Phys. Rev. B, 81(4), p. 045408.

[188] Zhu, J., Chen, J. Y., Park, H., Gu, X., Zhang, H., Karthikeyan, S., Wendel, N., Campbell, S. A., Dawber, M., Du, X., Li, M., Wang, J.-P., Yang, R., and Wang, X., 2016, "Revealing the Origins of 3D Anisotropic Thermal Conductivities of Black Phosphorus," Adv. Electron. Mater., 2(5), p. 201600040.

[189] Abeles, B., 1963, "Lattice thermal conductivity of disordered semiconductor alloys at high temperatures," Phys. Rev., 131(5), p. 1906.

[190] Klemens, P., 1955, "The scattering of low-frequency lattice waves by static imperfections," Proceedings of the Physical Society. Section A, 68(12), p. 1113.

[191] Gu, X., Li, X., and Yang, R., 2015, "Phonon transmission across Mg 2 Si/Mg 2 Si 1− x Sn x interfaces: A first-principles-based atomistic Green's function study," Phys. Rev. B, 91(20), p. 205313.

[192] Kundu, A., Mingo, N., Broido, D., and Stewart, D., 2011, "Role of light and heavy embedded nanoparticles on the thermal conductivity of SiGe alloys," Phys. Rev. B, 84(12), p. 125426.

[193] Katcho, N., Carrete, J., Li, W., and Mingo, N., 2014, "Effect of nitrogen and vacancy defects on the thermal conductivity of diamond: An ab initio Green's function approach," Phys. Rev. B, 90(9), p. 094117.

[194] Lambin, P., and Vigneron, J., 1984, "Computation of crystal Green's functions in the complex-energy plane with the use of the analytical tetrahedron method," Phys. Rev. B, 29(6), p. 3430.

[195] Rowe, D. M., 2005, Thermoelectrics handbook: macro to nano, CRC press.

[196] Majumdar, A., 1993, "Microscale heat conduction in dielectric thin films," J. Heat Transfer, 115(1), pp. 7-16.

[197] Walton, D., and Lee, E., 1967, "Scattering of phonons by a square-well potential and the effect of colloids on the thermal conductivity. II. Theoretical," Phys. Rev., 157(3), p. 724.

[198] Kim, W., and Majumdar, A., 2006, "Phonon scattering cross section of polydispersed spherical nanoparticles," J. Appl. Phys., 99(8), p. 084306.

[199] Cahill, D. G., Ford, W. K., Goodson, K. E., Mahan, G. D., Majumdar, A., Maris, H. J., Merlin, R., and Phillpot, S. R., 2003, "Nanoscale thermal transport," Journal of Applied Physics, 93(2), pp. 793-818.

[200] Evans, A. G., Mumm, D., Hutchinson, J., Meier, G., and Pettit, F., 2001, "Mechanisms controlling the durability of thermal barrier coatings," Progress in materials science, 46(5), pp. 505-553.

[201] Yang, R., Chen, G., and Dresselhaus, M. S., 2005, "Thermal conductivity modeling of core-shell and tubular nanowires," Nano letters, 5(6), pp. 1111-1115.

[202] Yang, R., Chen, G., Laroche, M., and Taur, Y., 2005, "Simulation of nanoscale multidimensional transient heat conduction problems using ballistic-diffusive equations and phonon Boltzmann equation," Journal of heat transfer, 127(3), pp. 298-306.

[203] Wang, J.-S., Wang, J., and Lü, J., 2008, "Quantum thermal transport in nanostructures," European Physical Journal B, 62(4), pp. 381-404.

[204] Li, X., and Yang, R., 2012, "Effect of lattice mismatch on phonon transmission and interface thermal conductance across dissimilar material interfaces," Physical Review B, 86(5), p. 054305.

[205] Zhao, H., and Freund, J. B., 2009, "Phonon scattering at a rough interface between two fcc lattices," Journal of Applied Physics, 105(1), p. 013515.

[206] Zhang, W., Fisher, T., and Mingo, N., 2007, "Simulation of Interfacial Phonon Transport in Si–Ge Heterostructures Using an Atomistic Green's Function Method," Journal of heat transfer, 129(4), pp. 483-491.

[207] Yamamoto, T., and Watanabe, K., 2006, "Nonequilibrium Green's function approach to phonon transport in defective carbon nanotubes," Physical review letters, 96(25), p. 255503.

[208] Chen, L., Huang, Z., and Kumar, S., 2013, "Phonon transmission and thermal conductance across graphene/Cu interface," Applied Physics Letters, 103(12), p. 123110.

[209] Huang, Z., Fisher, T., and Murthy, J., 2011, "An atomistic study of thermal conductance across a metal-graphene nanoribbon interface," Journal of Applied Physics, 109(7), p. 074305.

[210] Murakami, T., Shiga, T., Hori, T., Esfarjani, K., and Shiomi, J., 2013, "Importance of local force fields on lattice thermal conductivity reduction in PbTe1− xSex alloys," Europhysics Letters, 102(4), p. 46002.

[211] Larkin, J. M., and McGaughey, A. J., 2013, "Predicting alloy vibrational mode properties using lattice dynamics calculations, molecular dynamics simulations, and the virtual crystal approximation," Journal of Applied Physics, 114(2), p. 023507.

[212] Zhou, J., Li, X., Chen, G., and Yang, R., 2010, "Semiclassical model for thermoelectric transport in nanocomposites," Physical Review B, 82(11), p. 115308.

[213] Zaitsev, V., Fedorov, M., Gurieva, E., Eremin, I., Konstantinov, P., Samunin, A. Y., and Vedernikov, M., 2006, "Highly effective Mg 2 Si 1− x Sn x thermoelectrics," Physical Review B, 74(4), p. 045207.

[214] Zhang, Q., He, J., Zhu, T., Zhang, S., Zhao, X., and Tritt, T., 2008, "High figures of merit and natural nanostructures in Mg2Si0. 4Sn0. 6 based thermoelectric materials," Applied Physics Letters, 93(10), p. 102109.

[215] Dubay, O., and Kresse, G., 2003, "Accurate density functional calculations for the phonon dispersion relations of graphite layer and carbon nanotubes," Physical Review B, 67(3), p. 035401.

[216] Esfarjani, K., and Stokes, H. T., 2008, "Method to extract anharmonic force constants from first principles calculations," Physical Review B, 77(14), p. 144112.

[217] Baroni, S., de Gironcoli, S., Dal Corso, A., and Giannozzi, P., 2001, "Phonons and related crystal properties from density-functional perturbation theory," Reviews of Modern Physics, 73(2), p. 515.

[218] De Gironcoli, S., Giannozzi, P., and Baroni, S., 1991, "Structure and thermodynamics of Si x Ge 1-x alloys from ab initio Monte Carlo simulations," Physical review letters, 66(16), p. 2116.

[219] de Gironcoli, S., 1992, "Phonons in Si-Ge systems: An ab initio interatomic-force-constant approach," Physical Review B, 46(4), p. 2412.

[220] De Gironcoli, S., Molinari, E., Schorer, R., and Abstreiter, G., 1993, "Interface mode in Si/Ge superlattices: Theory and experiments," Physical Review B, 48(12), p. 8959.

[221] de Gironcoli, S., and Baroni, S., 1992, "Effects of disorder on the vibrational properties of SiGe alloys: failure of mean-field approximations," Physical review letters, 69(13), p. 1959.

[222] S. Baroni et al., http://www.quantum-espresso.org.

[223] Li, X., and Yang, R., 2012, "Size-dependent phonon transmission across dissimilar material interfaces," Journal of Physics: Condensed Matter, 24(15), p. 155302.

[224] Rego, L. G., and Kirczenow, G., 1998, "Quantized thermal conductance of dielectric quantum wires," Physical review letters, 81(1), p. 232.

[225] Pettersson, S., and Mahan, G., 1990, "Theory of the thermal boundary resistance between dissimilar lattices," Physical Review B, 42(12), p. 7386.

[226] Chen, G., 2003, "Diffusion–transmission interface condition for electron and phonon transport," Applied Physics Letters, 82(6), pp. 991-993.

[227] Tani, J.-i., and Kido, H., 2005, "Thermoelectric properties of Bi-doped Mg< sub> 2</sub> Si semiconductors," Physica B: Condensed Matter, 364(1), pp. 218-224.

[228] Perdew, J. P., and Zunger, A., 1981, "Self-interaction correction to density-functional approximations for many-electron systems," Physical Review B, 23(10), p. 5048.

[229] Bitzek, E., Koskinen, P., Gähler, F., Moseler, M., and Gumbsch, P., 2006, "Structural relaxation made simple," Physical review letters, 97(17), p. 170201.

[230] Hutchings, M., Farley, T. W. D., Hackett, M., Hayes, W., Hull, S., and Steigenberger, U., 1988, "Neutron scattering investigation of lattice dynamics and thermally induced disorder in the antifluorite Mg< sub> 2</sub> Si," Solid State Ionics, 28, pp. 1208-1212.

[231] Kearney, R., Worlton, T., and Schmunk, R., 1970, "Lattice dynamics of magnesium stannide at room temperature," Journal of Physics and Chemistry of Solids, 31(5), pp. 1085-1097.

[232] Tani, J.-i., and Kido, H., 2008, "Lattice dynamics of Mg< sub> 2</sub> Si and Mg< sub> 2</sub> Ge compounds from first-principles calculations," Computational Materials Science, 42(3), pp. 531-536.

[233] Meng, Q., Wu, L., and Zhu, Y., 2013, "Phonon scattering of interfacial strain field between dissimilar lattices," Physical Review B, 87(6), p. 064102.

[234] Wang, S., and Mingo, N., 2009, "Improved thermoelectric properties of Mg 2 Si x Ge y Sn 1-xy nanoparticle-in-alloy materials," Applied Physics Letters, 94(20), pp. 203109-203109-203103.

[235] Payton III, D. N., Rich, M., and Visscher, W. M., 1967, "Lattice thermal conductivity in disordered harmonic and anharmonic crystal models," Physical Review, 160(3), p. 706.

[236] Hellman, O., and Broido, D. A., 2014, "Phonon thermal transport in Bi 2 Te 3 from first principles," Physical Review B, 90(13), p. 134309.

[237] Seol, J. H., Jo, I., Moore, A. L., Lindsay, L., Aitken, Z. H., Pettes, M. T., Li, X., Yao, Z., Huang, R., and Broido, D., 2010, "Two-dimensional phonon transport in supported graphene," Science, 328(5975), pp. 213-216.

[238] Ong, Z.-Y., and Pop, E., 2011, "Effect of substrate modes on thermal transport in supported graphene," Physical Review B, 84(7), p. 075471.

[239] Mingo, N., 2006, "Anharmonic phonon flow through molecular-sized junctions," Physical Review B, 74(12), p. 125402.

[240] Mingo, N., Stewart, D. A., Broido, D. A., and Srivastava, D., 2008, "Phonon transmission through defects in carbon nanotubes from first principles," Phys. Rev. B, 77(3), p. 033418.